Johann Patrick Taufenegger, B.Sc.

Master Thesis 2017 supervised by
Univ. –Prof. Dipl. –Ing. Dr. mont. Gerhard Thonhauser
Dipl.-Ing. Miodrag Ivanovic

Redesigning a Drilling Test Facility for a Drill String Prototype

dpe DEPARTMENT PETROLEUM ENGINEERING

MONTAN UNIVERSITÄT

Affidavit

I declare in lieu of oath that I wrote this thesis and performed the associated research myself using only literature cited in this volume.

Eidesstattliche Erklärung

Ich erkläre an Eides statt, dass ich diese Arbeit selbständig verfasst, andere als die angegebenen Quellen und Hilfsmittel nicht benutzt und mich auch sonst keiner unerlaubten Hilfsmittel bedient habe.

_____

Name, 18 September 2017

Abstract

This thesis discusses the reconstruction of a drilling test stand, formerly used for dual-body bits, by extending its testing capabilities onto specific testing conditions, designed to test the performance of a drill string prototype. Both testing platforms are merged into one drilling facility, offering the possibility to conduct the former and new testing functions with the least possible facility adjustments.

Its design is presented in form of a system architecture covering its modular components and functions in a well arranged manner. The main modular extensions consists of test well, a customized well head and drill site surface equipment. By conducting a brief geomechanical study based on seismic data of the Trofaiach basin, the far field stresses acting upon a borehole with 300 m depth are investigated.

Within the cased hole, a 9 5/8 in casing is immersed in completion fluid, capable of receiving injected liquid and gaseous influxes. The well is provided with a completion fluid circulation heating system, to accelerate the curing process of the test cement within the 9 5/8 in casing, which is drilled.

The completed facility extension allows overbalanced drilling with well control interventions and managed pressure drilling, while tracking the dynamic drilling performance of the prototype under these conditions. The subsurface as well as surface components are designed within the practical disciplinary design methods in drilling and mechanical engineering. The tri-axial Van Mises failure criterion is utilized during the design, heating as well as the test phases, to monitor the casing stresses, in order to guarantee its integrity.

A register of the acquisition costs of the entire facility as well as the costs of the demonstrated test runs are included. Furthermore, steps are introduced to upgrade the designed facility to conduct sensory tests for high pressure, high temperature wells.

Zusammenfassung

Diese Abschlussarbeit beinhaltet die Rekonstruktion einer ehemaligen Bohrversuchsanlage mit erweiterten Testfähigkeiten, welche für einen Bohrstrang Prototypen zugeschnitten sind, um ihre Funktion unter bestimmten Bedingungen auszuwerten. Beide Prüfstände wurden zu einer Anlage vereint und bieten die Möglichkeit die ehemaligen sowie die erweiterten Testfunktionen mit minimaler Einstellungsänderung der Versuchsanlage durchzuführen.

Ihre Konstruktion wird in Form einer Systemarchitektur vorgestellt, welche den modularen Aufbau der Funktionen und Komponenten übersichtlich darstellt. Mittels einer kurzen geomechanischen Studie, basierend auf seismischen Daten des Trofaiacher Beckens, wurden die Spannungsfelder und somit die Spannungen im Bohrloch mit 300 m Tiefe ermittelt.

Das verrohrte Bohrloch birgt eine 9 5/8 in Verrohrung, welche in einem Ergänzungsfluid gelagert ist, mit der Fähigkeit flüssige und gasförmige Zuströme durch Injektion zu simulieren. Das Bohrloch ist versehen mit einem Heizsystem, dass die 9 5/8 in Verrohrung mit Dampf beheizt um den Aushärtungsprozess des darin liegenden Testzements zu beschleunigen, auf welches die Bohrtests ausgeübt werden.

Die Anlage ist fähig unter statischem und dynamischem Druckeinschluss eine Testbohrung abzuteufen, worauf die dynamischen Belastungen am Bohrstrang gemessen werden. Die ober- sowie untertage verbauten Anlagenelemente wurden nach Dimensionierungsmethoden des allgemeinen Maschinenbaus sowie die der Tiefbohrtechnik durchgeführt. Die Spannungszustände der Verrohrungen wurden während dem Einbau, Heizen und Tests mittels der triaxialen Gestaltänderungshypothese von Van Mises überwacht, um die Integrität zu gewährleisten.

Eine Kostenauflistung der Gesamtanlage sowie der angeführten Testdurchläufe wurden inkludiert, sowie die Abänderungsaspekte für die Anlage, um Sensoren auf hohen Drücken und Temperaturen zu testen.

Acknowledgements

First, I would like to profoundly thank my advisor at TDE Group, Dipl.-Ing. Miodrag Ivanovic, for giving me the chance to write this thesis on this innovative topic as well as granting me the freedom of incorporating my ideas into this work. I thank him for guiding me through the process of this thesis and for sharing his experience.

Furthermore, I would like to thank Univ. -Prof. Dipl. -Ing. Dr. mont. Gerhard Thonhauser, for being my advisor at the University of Leoben and providing me with invaluable insight to complete this thesis. I extend my thanks to the colleagues at the Chair of Drilling and Completion Engineering, particularly Dipl.-Ing. Christoph Thonhofer for administrative support.

I would also like to thank Dipl.-Ing. Medardus Ramsauer at TDE Equipment and Manufacturing, for sharing his ideas and practical experience to improve the outcome of my work. I express my gratitude to my student colleagues, with whom I shared an academic career of solidarity trough out moments of joy and hardship.

Most of all, I deeply thank my family, especially my parents for supporting me in my ambitions to this point in life.

Contents

Chapter 1 Introduction

"Practice makes perfect. After a long time of practicing, our work will become natural, skilful, swift, and steady"

Bruce Lee

Athletes from all disciplines live up to similar creeds, while preparing for the event, where their performance is tested. Preparations become even more diverse, when equipment is involved, as these have to fulfil certain requirements to form a successful synergy with its wielder.

This becomes even more evident, when only its integrity decides over victory or defeat, such as in formula one racing, where one can clearly observe, that over the years, countless tests on vehicle prototype components have led to the performance summit of today. This fact can be directly projected as an analogy to the drilling industry, where companies have developed sophisticated down hole tools, in order to establish a conduit between surface and hydrocarbon deposits under tough circumstances.

One such innovation resides within the company TDE Equipment and Manufacturing, situated in Edling, Austria. This drill string prototype is based on a unique technology platform and possesses revolutionary capabilities. This thesis comprises the design of a testing facility, which takes the drill string prototype into a real feedback environment, in order to screen its shortcomings and subsequently unlock its potentials.

The testing facility is designed on the basis of a former drilling test stand and requires a vertical well with 300 m depth, accompanied by a tri-axial well design, located on the company's vicinity. In order to design the well, a geomechanical study was conducted, based on former borehole and seismic data originating from the basin of Trofaiach.

The key components and modifications as well as installation considerations in order to realize the unique features of the facility are described with a modular system architecture. Furthermore, drilling test programmes with overbalanced as well as managed pressure drilling on various cement compositions are presented. The final chapter illustrates the overall cost estimates for the facility as well as the costs per test run.

1.1 Prologue

The drilling test stand was formerly property of the University of Leoben. The research conducted on this test stand, primarily concerned various types and set ups of dual-body bits as shown in figure 1, consisting of a coring bit (rim) and a centre bit (plug). The latter can be retrieved or adjusted via wire line, both bodies intended to be deployed as one unit.

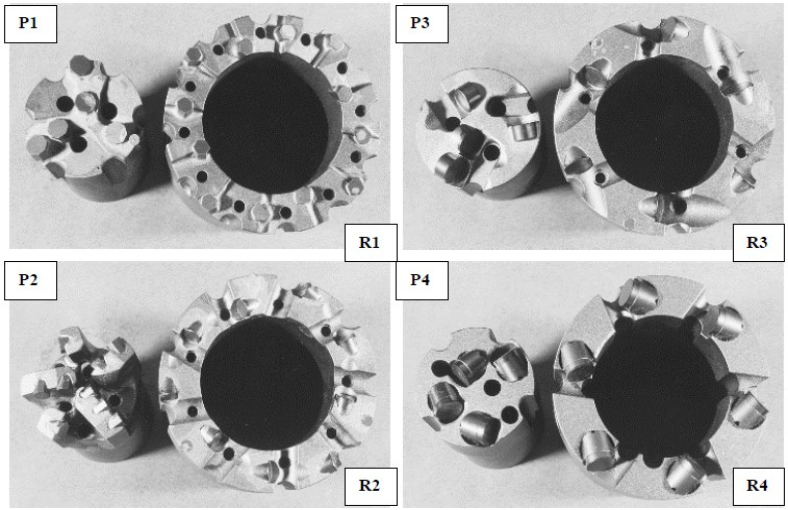

Figure 1: Dual body-bits in various Polycrystalline Diamond Compact (PDC) cutter arrangements, researched at the University of Leoben ([2] p. 7).

This configuration allows dynamic adjustments in order to increase Rate of Penetration (ROP), as well as changing from coring to drilling and vice versa. A. Bencic [1] published his work with this test stand, examining the cutting performance of dual-body bits, tested on several sedimentary rocks. This is done by adjusting the vertical offset of the tool phase, while drilling. J. de Sousa [2] conducted research leaned more towards the fluid dynamic behavior, regarding the dual-body bit in terms of hole cleaning and bit balling under similar circumstances. Both studies embody the intent to make the technology more competitive besides conventional drilling and ultimately more cost effective at flat oil prices.

1.1.1 Former Design Layout

The test stand set up, is featured in figure 2 [1]. The pressure vessel is located in the mast and can be divided, as well as hydraulically lifted at the lower most flange. There, a chamber can be equipped with a fore fitted sedimentary rock cylinder. After closure, the pressure vessel can manage pressurizations of up to 400 bar, in order to simulate down hole pressure conditions. Weight on Bit (WOB) is established by the main cylinder and torque with a top drive, which transmits 7100 Nm and Revolutions per Minute (RPMs) up to 910. Flow rates of the triplex mud pump were recorded up to 300 l/min.

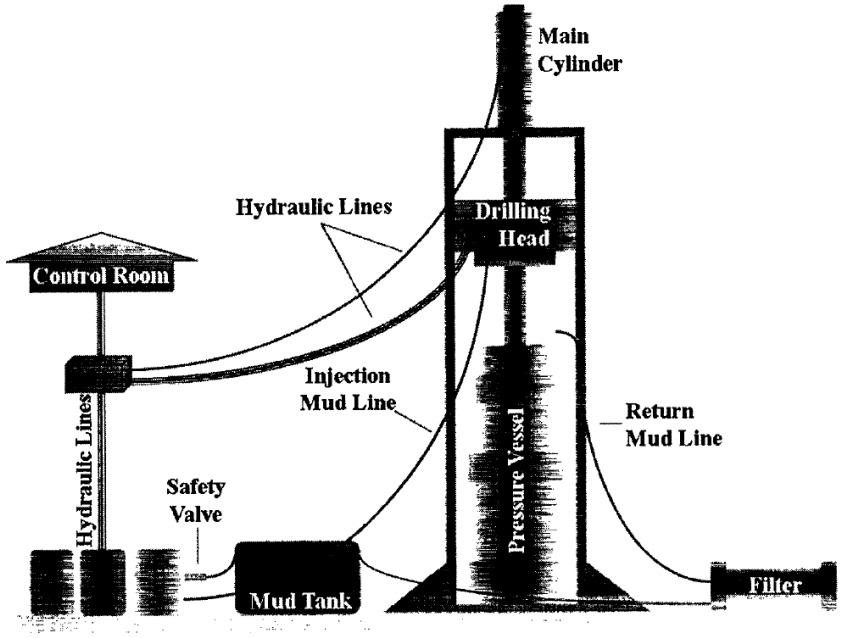

Figure 2: The controls are managed manually from a centre panel.

The drilling test stand had been decommissioned due to utility expenses and is now in possession of the company TDE Equipment and Manufacturing, which continues research on this technology.

1.2 Objective

The intended testing capability extensions and modifications for the new drilling facility are primarily geared towards the drill string prototype and are listed as following:

1. Testing and recording of the prototype's dynamic behavior, while drilling variable cement compositions, mimicking various sedimentary rock strengths.
2. Initiate liquid and/or gas influxes during tripping, to test the response of various sensors for kick detection and well control measures.
3. Testing and recording of the prototypes behavior while drilling at underbalanced conditions.
4. Functions of the former drilling test stand should be retained and integrated into the new system.

Figure 3: Former drilling test stand as installed at the University of Leoben.

Chapter 2 Redesigning a Drilling Test Facility for a Drill String Prototype

Realizing the requirements regarding the extended testing capabilities, forced a new design or at least an alteration of the old design to a certain degree. During the redesign phase, additional components are inevitable and presented as a modular system architecture, as shown in figure 4, to ensure a good overview.

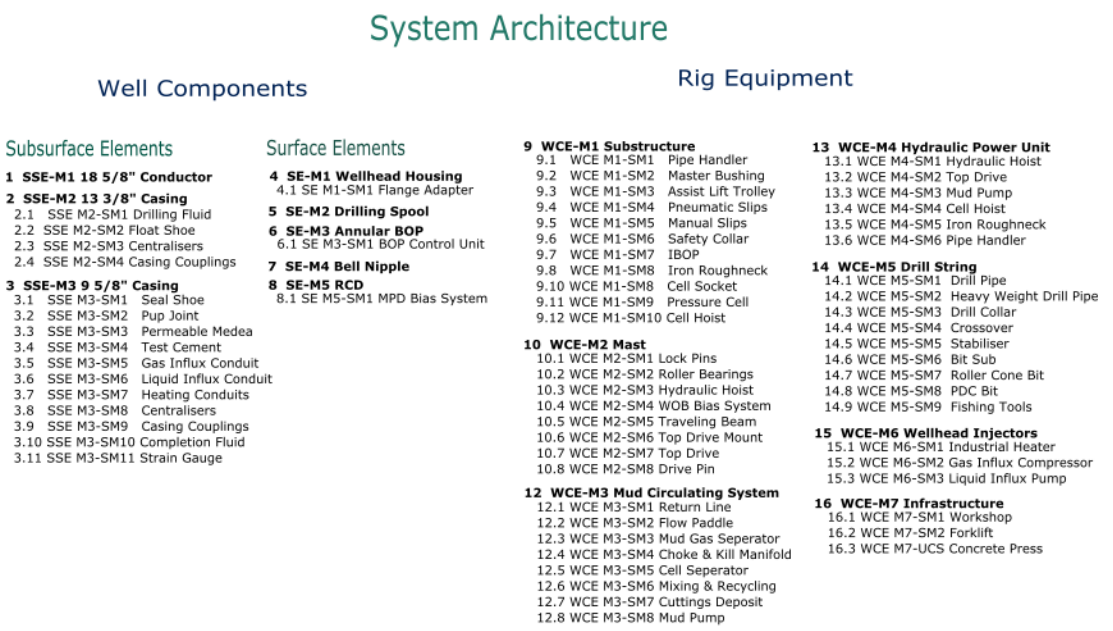

Figure 4: The facility is divided into two main compartments, being the well construction equipment and the well components, which is further differentiated between subsurface and surface elements.

The modular set up results from an assembly drawing with Computer Aided Design (CAD), shown in the Appendix A, where all components can visually be allocated. The essential modules and associating sub modules that make up the unique capabilities of the facility in order to create the decisive test environment are described in more detail.

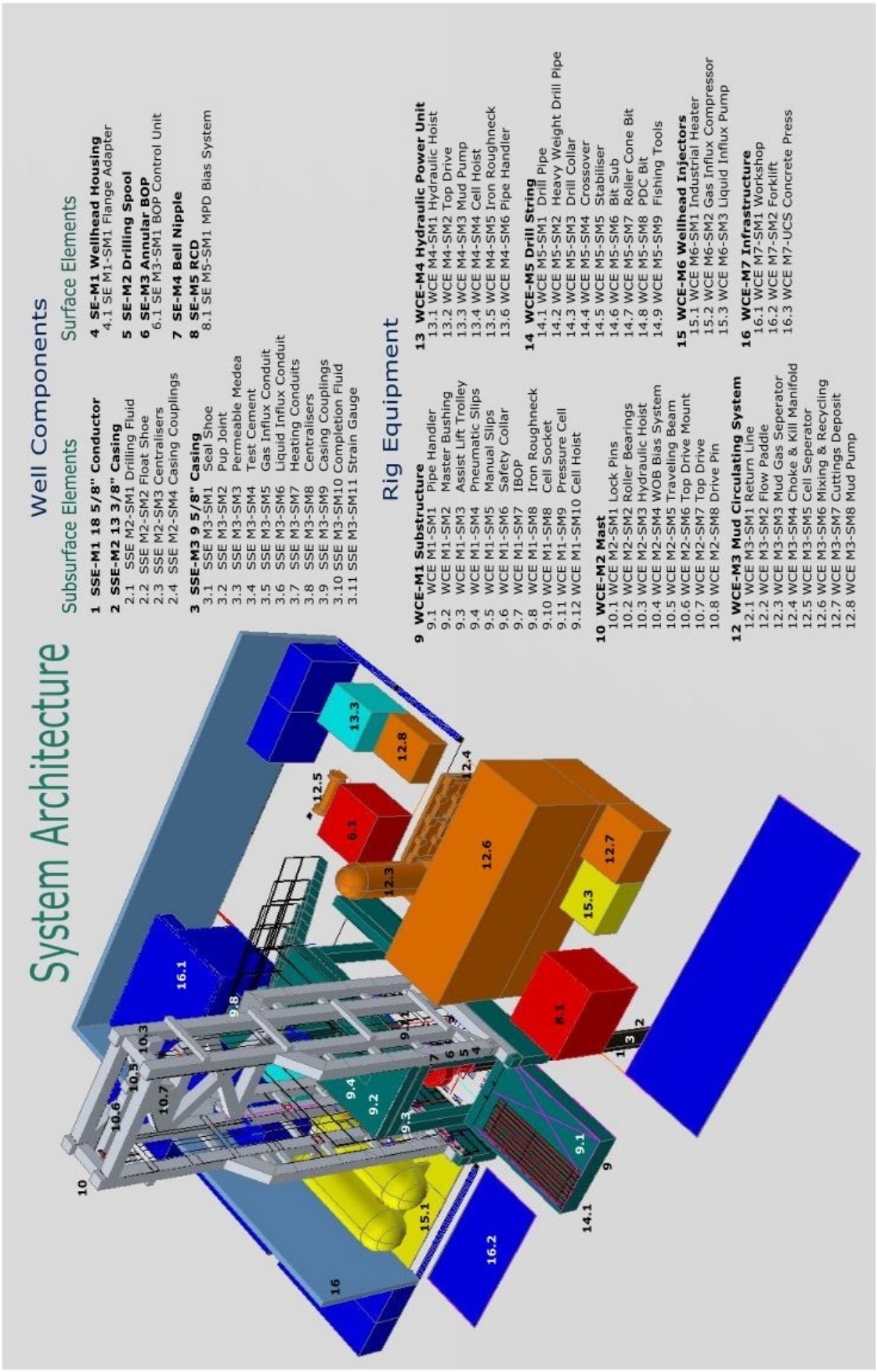

Figure 5: The 3D layout of the drilling test facility measures 22m in length and 21m in width. For visual reasons, the roof which shelters most of the equipment is left out.

2.1 Well Components

The proposed Basis of Design (BOD) of the vertical well according to water law is shown in figure 5 and consists of three casing strings, exploiting the depth limit of 300 m for the lower most casing string. A more detailed view of the well and its interior can be seen in Appendix A.1.

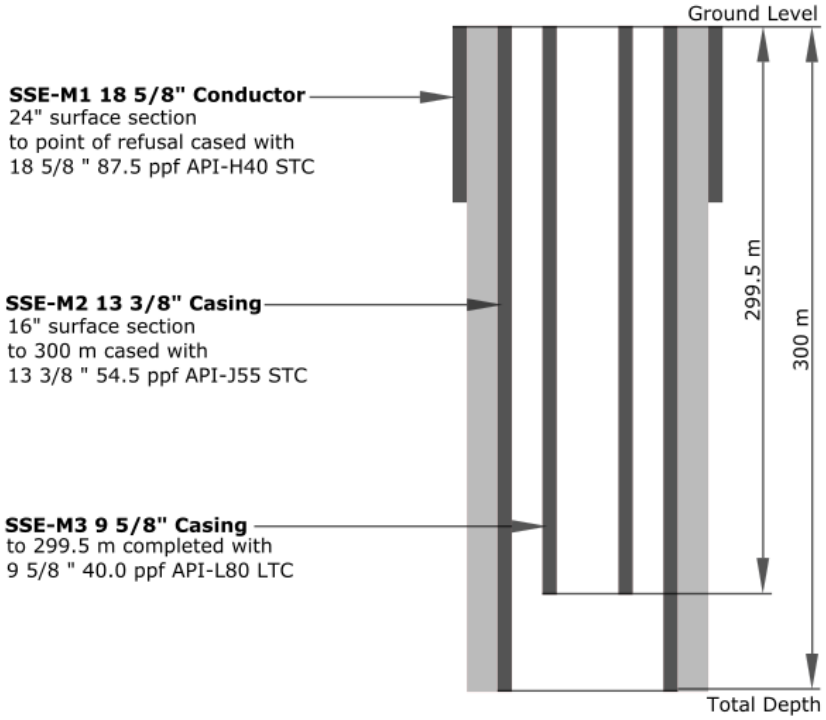

Figure 6: Well schematic of the proposed BOD as a frontier approach. The casing strings are not according to scale.

For drilling operations on land, conductor casings are often driven into the ground with a diesel pile-driving hammer, in other cases, drilling a hole and cementing the conductor into place. According to T. Byrom [3], the setting depths of conductors can be very simple or rather complicated. However for many shallow wells, most conductors are set at depths of 15 to 33 m, depending on how hard or soft the surface soil is. For this application, the recommendation according to S. Devereux [4] is proposed, by driving the conductor to the deepest possible point.

2.1.1 Mechanical Earth Model

Reservoir geomechanics on the behalf of drilling, requires knowledge on the in situ stress state, mechanical rock properties, mechanical behavior as a function of pore pressure and failure criteria when planning a wells trajectory for the desired location. The intended well placement is within the companies vicinity located in Edling related

to the basin of Trofaiach. Gruber et al published a geophysical study on this basin, on which this particular evaluation of geomechanics builds on [5].

2.1.1.1 The Trofaiach Basin

The basin of Trofaiach is classified as a pull-apart basin, from which the far field stresses are derived from, caused by. a major strike-slip fault as the main faulting mechanism, shown in figure 7 as "Trofaiach Fault".

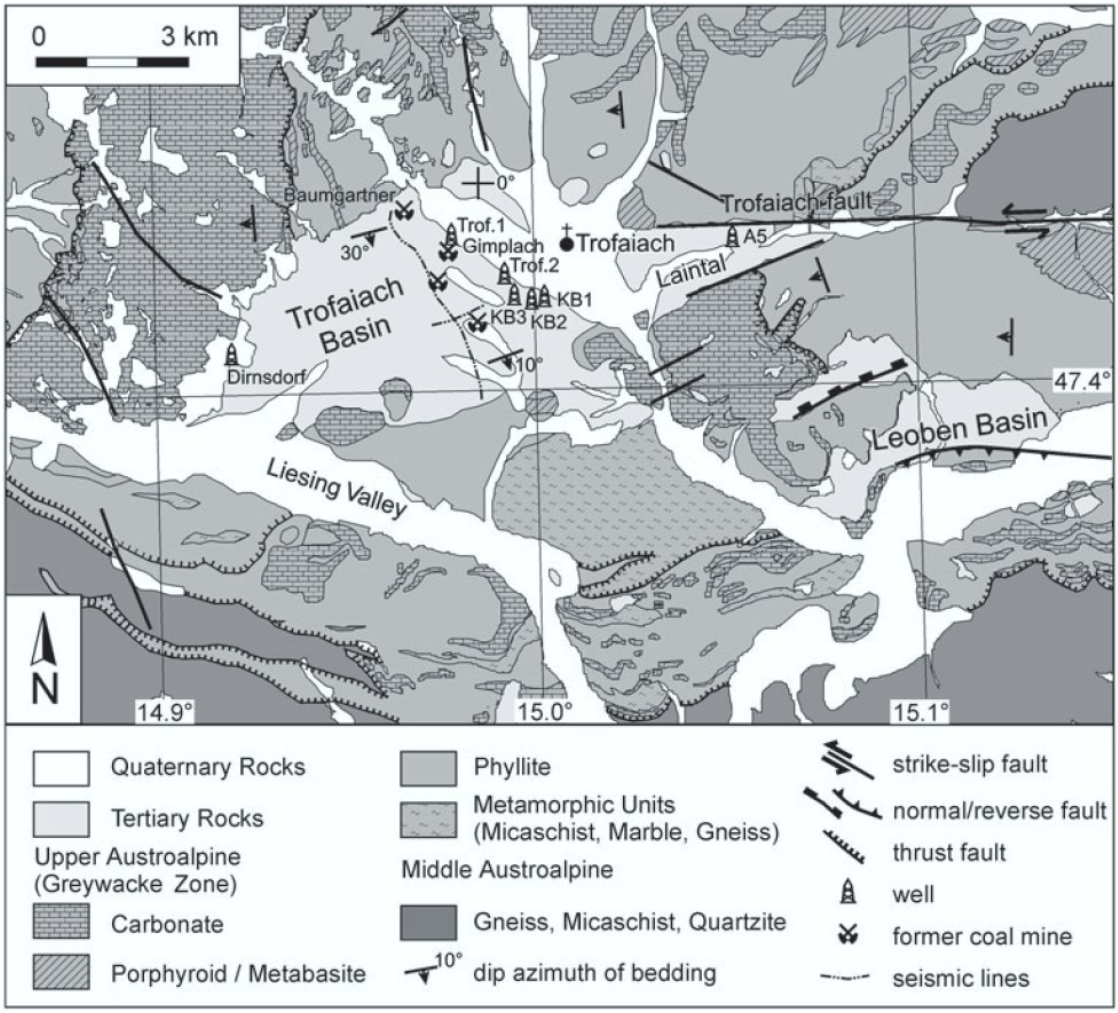

Figure 7: The basin of Trofaiach is subjected to a strike-slip fault located on its north west. Reference wells, subordinate faulting mechanisms as well as rock classifications are shown ([5], p. 283).

By means of a stress map according to Bada et al [6], the far field stress orientation for the Trofaiach basin can be derived as shown in figure 8. The Mur - Mürz - Zilina fault zone reveals an azimuth of 40° for the orientation of maximum horizontal stress S_{Hmax} and perpendicular to it the orientation of minimum horizontal stress S_{hmin}.

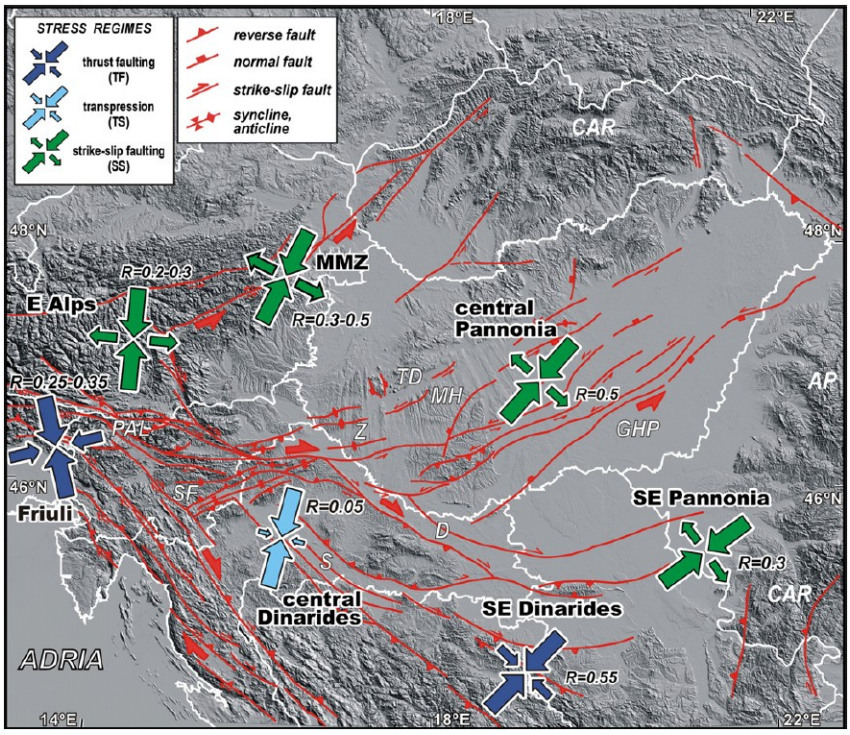

Figure 8: Stress orientations of the Pannonian basin. "MMZ" refers to the Mur-Mürz-Zilina fault zone. The prominent arrows show the direction of maximum horizontal stress.([6], p.173).

With reference wells and the main faulting mechanism of this particular basin, as well as the stress orientations of S_{Hmax} and S_{hmin}, the evaluation according to frictional faulting theory can be applied for the planned well. The chosen well of reference is named "Trofaiach 2" in Kehrwald near "Trofaiach 1" in Gimplach, as it is nearer to the vicinity of TDE Equipment and Manufacturing shown in figure 9.

Figure 9: Satellite image air distance of a reference well bore is 3.17 km. The upper left shows the adopted far field stress vectors with respect to the TDE compound marked with a red square (Google 2017).

2.1.1.2 Geophysical Data

The seismic data used are pseudo density logs and the associated interval transit times to derive further parameters as shown in table 1. The basin depth was reported to be 800 to 900m and was scaled into 3 sections, meaning that pseudo densities and corresponding interval transit times were averaged for each section. The depth for the test well with 300m reaches the second section of the lithology which ends at the approximate depth of 450m. The formations drilled were mainly calcareous shale, coaly shale and minor layers of thin sandstone as shown in figure 10 for "Trofaiach 1" and "Trofaiach 2".

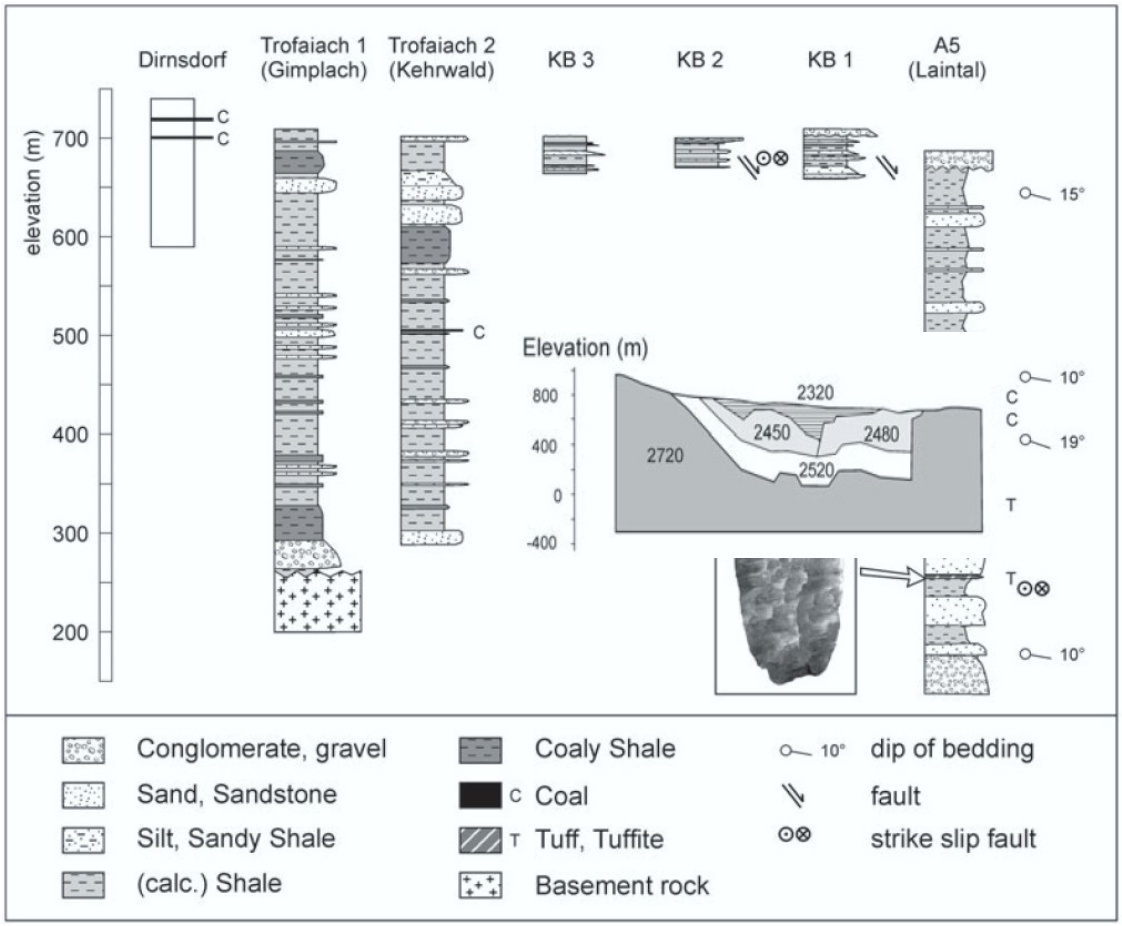

Figure 10: Lithology of reference wells consist mainly of calcerous shale. The average pseudo densities at the depth of interest of 300 m were logged with 2320 kg/m³ and 2450 kg/m³ ([5], p. 284).

The compression waves from seismic readings are stacked velocities, ranging from 2100 to 2500 m/s for the upper interval (section 1) and 2700 to 3200 m/s for the lower interval (section 2). An average value for both ranges were applied to construct the pressure profiles.

Table 1: Parameters derived from pseudo density and compression waves.

Parameter	Unit	Relationship	Section 1	Section 2
P wave	[m/s]	$\frac{V_p}{V_s} = \sqrt{3}$	2,300.0	2,950.0
Shear wave	[m/s]	$\frac{V_p}{V_s} = \sqrt{3}$	1,329.4	1,445.1
Poisson's Ratio	[-]	$\nu = \frac{(V_p^2 - 2V_s^2)}{2(V_p^2 - V_s^2)}$	0.249	0.249
Shear modulus	[Pa]	$G = \rho V_s^2$	3,084,393.1	3,540,462.4
Poisson solid	[Pa]	$\lambda = G$	3,084,393.1	3,540,462.4
Young's Modulus	[Pa]	$E = \frac{(3\lambda + 2G)}{(\lambda + G)}$	7,710 982,1	8,851 156,10
Biot coefficient	[-]	permanent trend	0.6	0.6

A commonly used equation for predicting the pore pressure gradient P_p by means of interval transit times is Eaton's method shown in equation 1 valid for shale formations.

$$P_p = S_v - (S_v - P_{hyd})\left(\frac{\Delta t_n}{\Delta t}\right)^3 \quad (1)$$

Whereas,

S_v …Overburden stress (psi)

P_{hyd} …Hydrostatic pressure (psi)

Δt_n …Normal transit time for shale (µs/ft)

Δt … Transit time obtained by logging (µs/ft)

The normal transit time for shale is valued at 114.5 µs/ft as an average value according to Carmichael [7].

The Biot coefficient describes the poroelasticity of rocks, defined as the ability of pore pressure to counteract external stress and ranges from 0 for pore free rocks and 1 for maximum pore pressure influence. For shale, it is difficult to predict this, as absolute values can only be generated with comparing hydrated and dry bulk samples, dependant on its texture and composition within an uni-axial unloading cell. In publications, Biot values even stray for the same well log depending on which method is used for correlation [8]. According to X. Luo, absolute values are secondary compared to its depth trend, the continuity is of priority. Based on laboratory test values of O. Vincke [9], an average value of 0.6 was assumed as a continuous trend for

this relatively shallow well. Referring to the stress classification system of E.M. Anderson on frictional faulting theory, the stress magnitudes can be assessed according to figure 11.

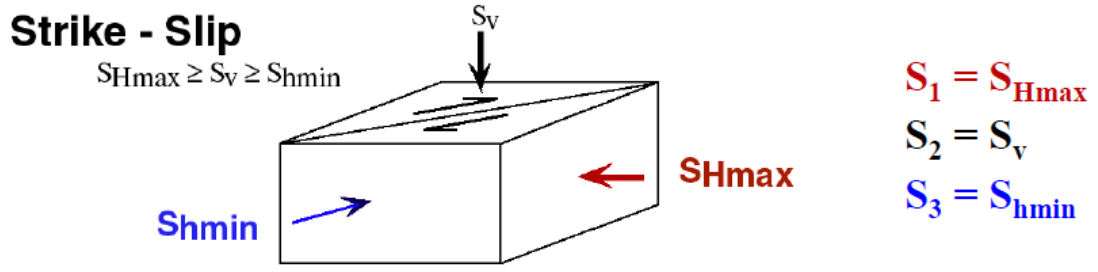

Figure 11: Governing stress magnitudes of a strike-slip environment ([10] s4, p. 25).

The corresponding equation for this fault mode is given in equation 2.

$$\frac{S_{Hmax} - P_p}{S_{hmin} - P_p} = \sqrt{\mu^2 + 1} + \mu^2 \tag{2}$$

Whereas,

S_{Hmax} …Maximum horizontal stress (psi)

S_{hmin}…Minimum horizontal stress (psi)

P_p…Pore pressure (psi)

μ… Internal friction coefficient

The internal friction coefficient resides between 0.6 and 1 according to Bayerlee's law. In general the ratio between S_{Hmax} to S_{hmin} is from 3 to 5 for the earths crust world wide. According to M. D. Zoback [11], internal friction coefficients were determined from locations as Fenton Hill in the UK, Silijan in Sweden and Dixie Valley Nevada in the US to be at 0,6 and seems to be a common occurrence, therefore used for these calculations. The effect of poroelasticity is incorporated for the stress calculations as shown in equation 3.

$$\Delta S_H = \alpha \frac{1 - 2\nu}{1 - \nu} \Delta P_p \tag{3}$$

Whereas

$\Delta S_{H...}$ Change in horizontal stresses (psi)

ΔP_p… Change in pore pressure (psi)

ν… Poisson's ratio (-)

α… Biot's coefficient (-)

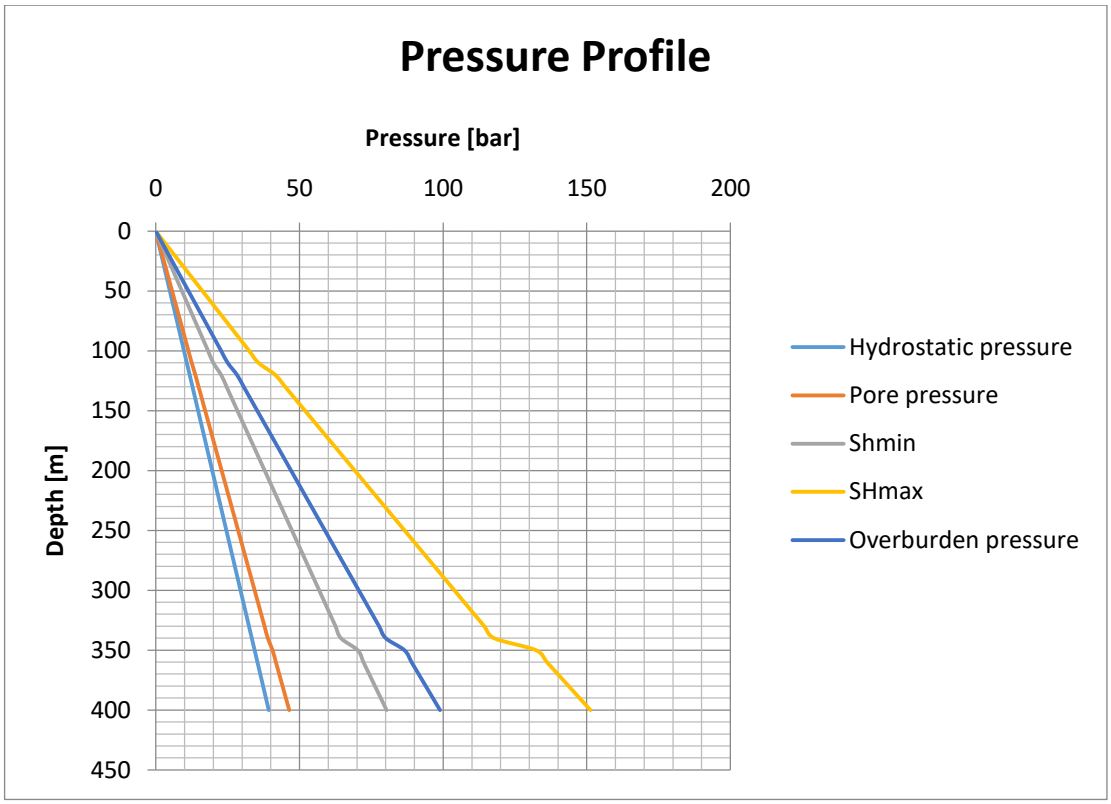

Figure 12: The above shows the pressure profile based on geophysical and geomechanical data.

By observing figure 12, one can clearly see the predicted pore pressure gradient picks up rather quick with depth, compared to the pore pressure gradient for normal pressured zones of 0.11 bar/m (0.465 psi/ft) as often stated in numerous sources This fact is open for debate as averaged value assumptions were made based on the measured source data regarding pseudo density and seismic velocities. Nevertheless, the basin of Trofaiach is also known as a wrench basin. These basin types are characteristic having narrow widths and extreme fast subsidence, meaning that at some point in time, the basin was subjected to a higher sedimentation rate than the pore fluids could equilibrate, causing slight overpressure. Furthermore, the majority of involved formations are calcareous shale, which supports this explanation. To calibrate the predicted fracture pressure P_{ff}, normally encountered in Leak Off Tests (LOTs) as S_{hmin} for certain values, a more practical approach with the equation of Hubbert and Willis was conducted, which neglects poroelastic effects, shown in equation 4.

$$P_{ff} = \frac{б_{ob} + 2P_f}{3} \tag{4}$$

Whereas,

$б_{ob}$ …Overburden pressure (psi)

P_f … Pore pressure

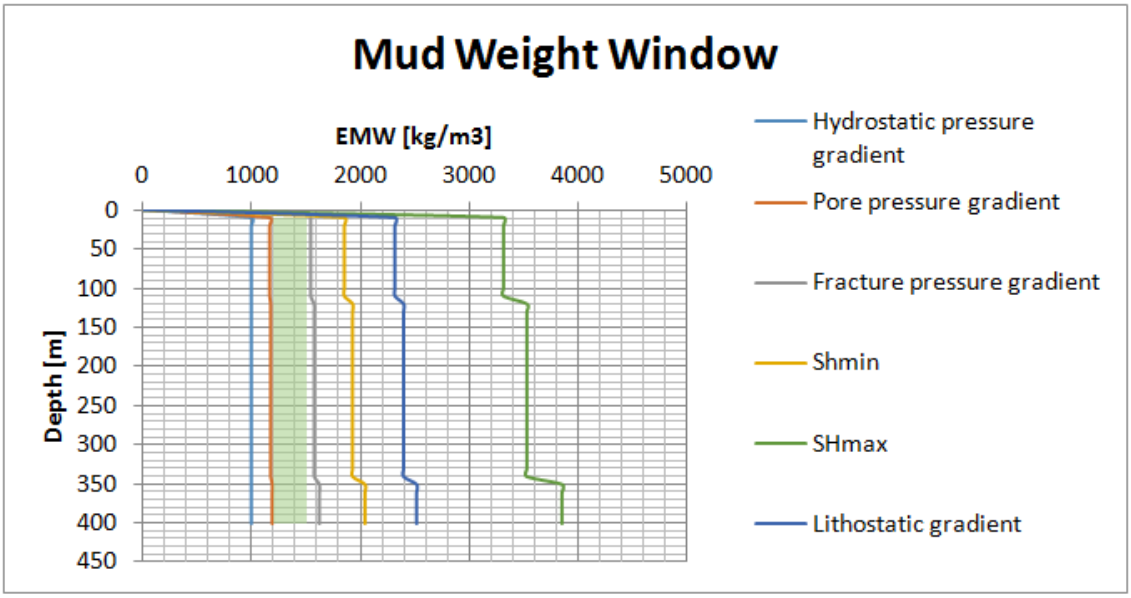

Figure 13: Pressure gradients displayed in equivalent mud weight. The window of interest considered drillable is marked in the grey area.

The pore pressure prediction coincides with the evaluated S_{hmax}, however for assurance an separate fracture gradient not tied into the evaluation of frictional faulting theory has been evaluated, which does not overlap with S_{hmax}. This might be due to the shallow depth as poroelastic effects become more dominant with greater depth, as the trend indicates. T. Engelder claims, that at shallower regions, S_{hmin} is more dominated by friction [12]. Nevertheless, the equation of Hubbert and Willis can be used as a fast approximation if limited data at hand for the fracture gradient.

2.1.1.3 Wellbore Stress Concentrations

The main failure mechanisms for a vertical wellbore, are either tensile in nature, with fracture propagation in the direction of S_{Hmax} or compressive failure, with breakouts advancing in the direction of S_{hmin}. In order to adjust an accurate mud weight, the stress concentrations for a borehole with 16" in diameter, needs to be evaluated with respect to the far field stresses. This is done in equations 5 to 7, with hoop stress $б_{\theta\theta}$ acting tangentially along the borehole wall, the radial stress $б_{rr}$ acting perpendicular to the hole's surface and the effective stress $б_{zz}$ acting parallel to the borehole axis. No thermal effects are considered here.

$$б_{\theta\theta} = S_{hmin} + S_{Hmax} - 2(S_{Hmax} - S_{hmin})cos2\theta - P_p - P_{mud} \quad (5)$$

$$б_{zz} = S_v - 2\nu(S_{Hmax} - S_{hmin})cos2\theta - P_p \quad (6)$$

$$б_{rr} = P_{mud} - P_p \quad (7)$$

Whereas,

S_{Hmax} …Maximum horizontal stress (psi)

S_{hmin}…Minimum horizontal stress (psi)

P_f … Pore pressure (psi)

ν… Poisson's ratio

Θ…Azimuth angle measured from S_{Hmax} (rad)

In order to define the upper bound of the stress amplitude profile, the uni-axial compressive strength C_0 for shale formations are predicted with equation 8, which was developed by Coates and Denoo derived from linear failure envelopes on dynamic measurements [13].

$$C_0 = 9.015E^{0.901} \tag{8}$$

Whereas,

E…Young's modulus (Pa).

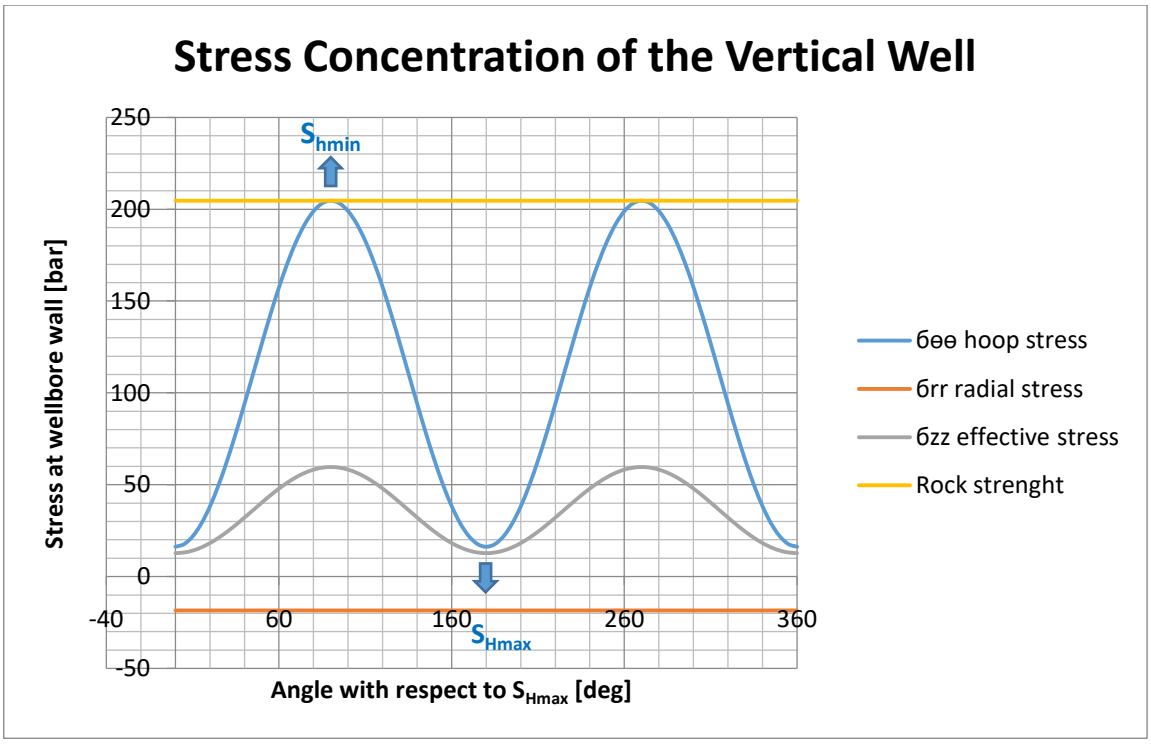

Figure 14: Stress concentrations of the 16 in OH.

The presented principal stress amplitudes at True Vertical Depth (TVD) of 300 m in figure 14 are calibrated to 540 kg/m³ (4.5 Pounds Per Gallon) (ppg)), meaning the mud pressure is far below the pore pressure. The loss of further hydrostatic at this point would theoretically trigger breakouts, as the hoop stress dissects the rock strength. For this reason, the wellbore collapse pressure is set to this value. Heavier mud will shift the hoop stress amplitude downward, with 1557 kg/m³ (13 ppg), it would dissect the

radial stress, which means tensile stresses around the wellbore are at work. If the radial stress line is overlaps the hoop stress amplitude (orange line), then the equivalent mud weight has reached S_{hmin}, the fracture pressure. Setting the mud density at 1258 kg/m^3 (10.5 ppg) including a 5 % safety margin as static mud weight is reasonable, as Equivalent Circulating Density (ECD) and cuttings will raise it.

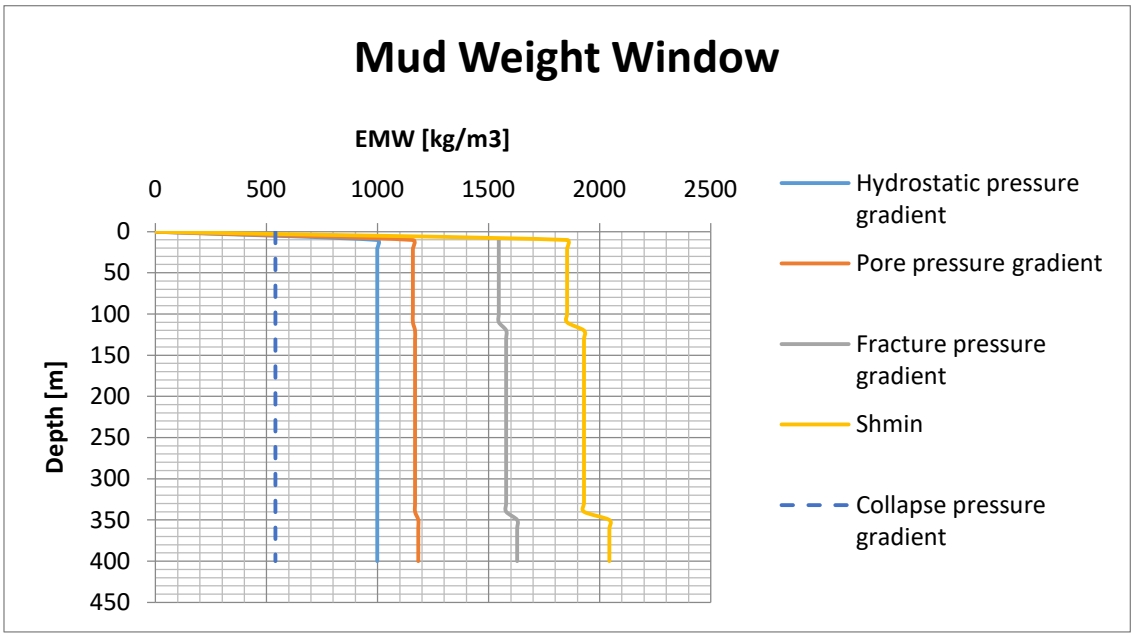

Figure 15: The dashed line indicates the collapse pressure gradient.

2.2 Casing Design

The outer 13 3/8" casing was designed using a geothermal well design methodology and a more precise approach by applying the tri-axial combined loads by Van Mises for insurance. This was conducted as it is intended to circulate brine as a completion fluid in the annular space between the 13 3/8" casing and the 9 5/8" casing and heated up to temperatures of 100°C. The heating system has the purpose to accelerate the hardening time of the drillable testing cement contained within the 9 5/8" casing.

2.2.1 Bi-axial Geothermal Well Design

Elements for the design were obtained from the report by A. Moumin, undergoing the steps by designing the casing according to the proposed minimum acceptable design factors [14]:

- Internal yield (burst) design factor 1.5 -1.8;
- Collapse design factors 1.2;
- Tensile design factors 1.5 -1.8
- and Compressive factor 1.2

Thermal aspects in terms of environment in which the casing resides are not an issue by itself. It is the differential temperature load cycles between ambient temperature down hole and the temperature of externally induced fluids, for instance cold water injection or steam injection that might harm the casing's integrity according to T. Byrom [15]. For this particular case, the circulating completion fluid exerts the differential temperature. The prevailing geothermal gradient in the basin of Trofaiach according to W. Gruber is shown in figure 16 [5].

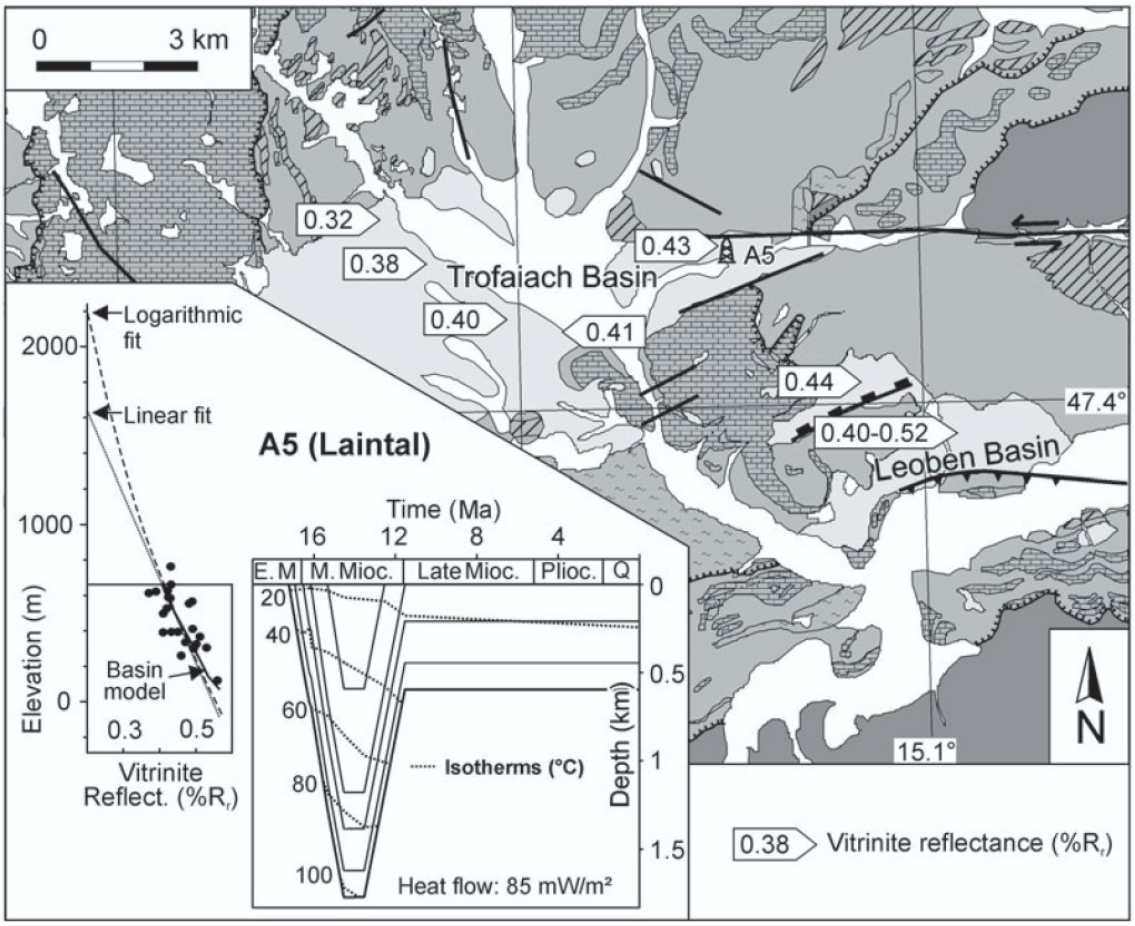

Figure 16: Temperature isotherms indicate 40°C for the approximate depth range of 200 to 400m is expected for casing setting([5] p.285).

These down hole temperature conditions stay constant whole year round until to a depth of 20m. From here seasonal temperature changes up to the surface influence the temperature gradient as shown in figure 17, [16], [17]. These temperatures serve as a basis to create differential temperatures with respect to the heating increments from 50 to 100°C on which the brine fluid and subsequently the casings are subjected to.

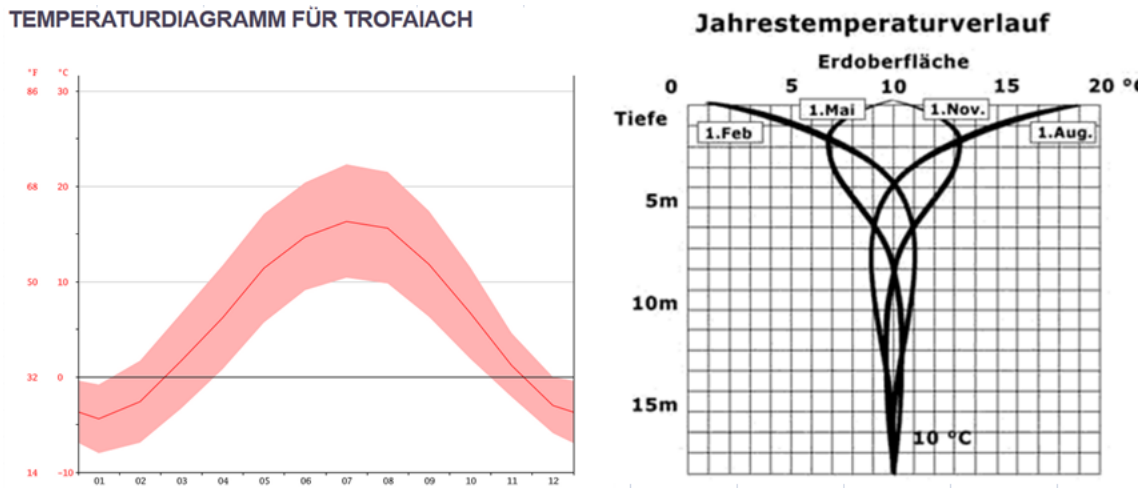

Figure 17: Seasonal surface temperature of Trofaiach on the left and the fluctuations of seasonal temperature of the subsurface showing constant temperatures at 20m depth.

For burst, collapse and tension, the yield strength according to the American Petroleum Institute (API), is degraded to the assumed maximum temperature in which the casing is exposed to and is only valid for casing setting and running. No temperature incremental increase was assigned to these particular design calculations. This value has been set to the 100°C for internal completion fluid heating, according to table 2, degrading the yield strength by a factor of 0.95 for uncemented casing, even though while setting it into ambient temperature environment of 40°C.

Table 2: Yield strength degradation due temperature, which is valid for J55 due similar metallurgical casing composition of K55 according to temperature effects (NZS) on casing properties ([14], p. 12).

Parameter	Temperature (°C)			
	20	100	200	300
API yield strength [-]	1	0.95	0.95	0.95
Tensile strength [-]	1	0.97	1.02	1.07

According to the compressive factor, it contains the requisite of compressive loads F_t due to thermal expansion during heating up of the well, when the casing is constrained, both longitudinal and lateral by cement, in which the proposed differential temperatures can be applied as shown in equation 9. However it does not directly give the indication on how it may affect collapse, while constrained, the only possible direction of expansion is inward.

$$F_t = C_t(T_2 - T_1)A_p \tag{9}$$

Whereas,

C_t… Thermal stress constant for casing steel (psi/°F)

T_2…Maximum expected temperature (°F)

T_1… Temperature at time where cement is set (°F)

A_p… Cross section area of pipe (in^2)

The calculations resulted in a 13 3/8“ 61 lb/ft J55 surface casing

2.2.1.1 Design on Tension Compression

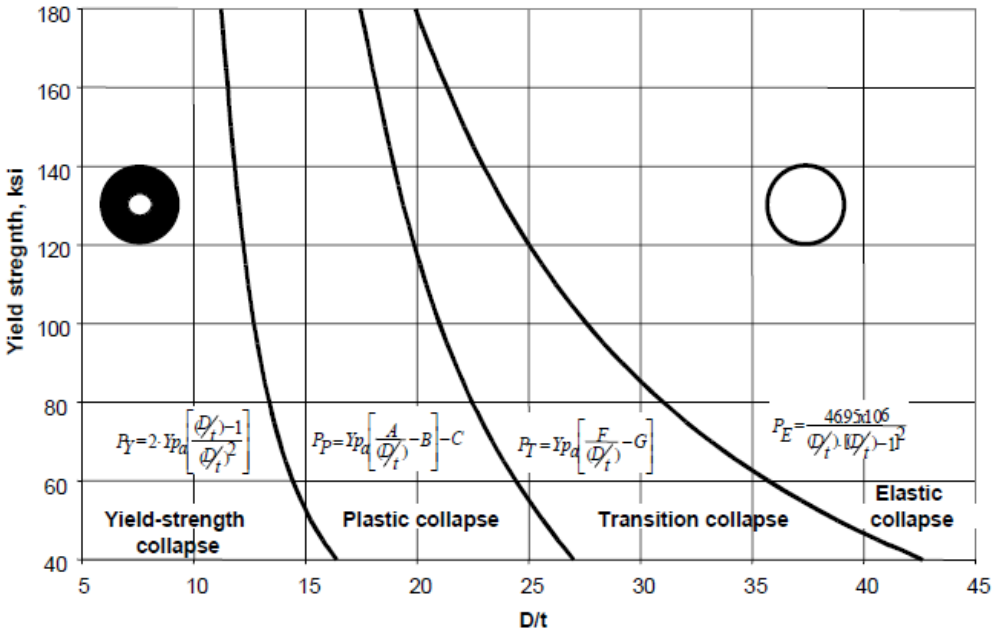

Figure 18: Four regions of collapse mode according to D/t ratio ([18] p. 1)

The calculated transition collapse pressure (collapse resistance) containing the effective degraded yield strength by biaxial means, divided by the calculated collapse design pressure (cement slurry- ,fresh water- and pump pressure) yields the design factor and should be greater than the minimum design factor by comparison.

2.2.1.2 Design on Tension Burst or Compression Collapse

The calculated burst resistance P according to Barlow shown in equation 10 containing the effective degraded yield strength by biaxial means, divided by the calculated burst design pressure (mud hydrostatic) yields the design factor and should be greater the minimum design factor by comparison.

$$P = 0.875\frac{2Y_p t}{OD} \tag{10}$$

Whereas,

Y_{pa}…Minimum yield strength of thermal degraded pipe (psi)

t…Pipe thickness (in)

OD…Outer pipe diameter (in)

2.2.1.3 Design on Tension

For this design, the string weight, shock load and the loads for pressure testing were included according to A. Moumin [14].

2.2.1.4 Design on Compression

According to equation 11, the calculated thermal compression forces were conducted for all 4 seasons regarding thermal effects from 50 to 100°C in 10°C heating steps and in 5 m increments to TVD.

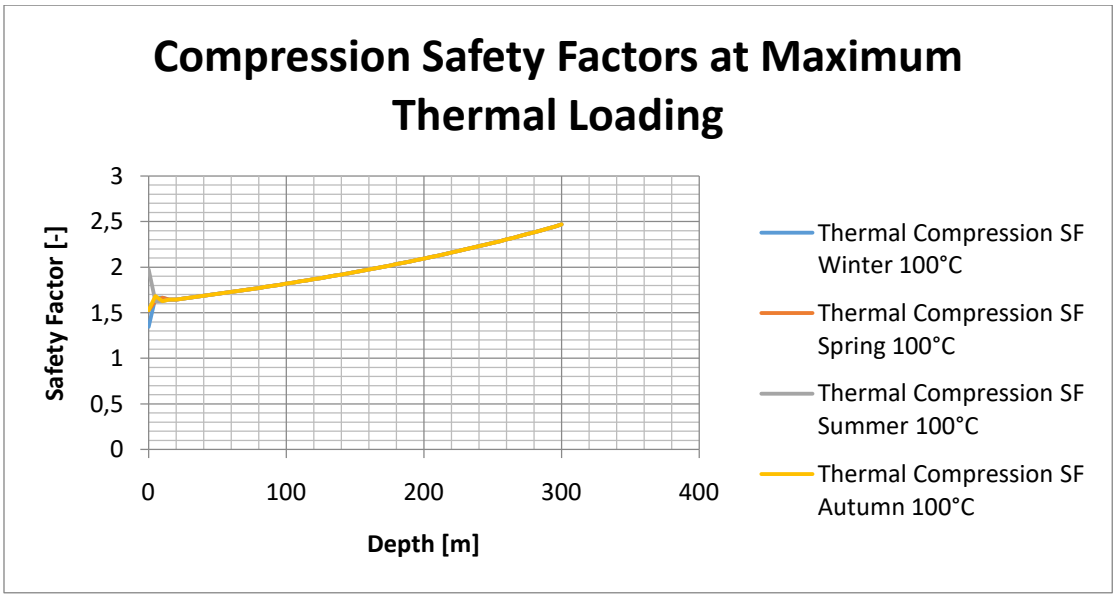

Figure 19: Thermal compressive Safety Factors vs. Depth.

Figure 19 shows that for the highest heating temperature of 100°C, the 13 3/8 in casing yields the lowest safety factor of 1.34 during winter periods higher than the design factor of 1.2. The trend shows that the surface part of the casing is the most thermally stressed segment of the well, due to the highest differential temperature. Assuming an average surface temperature of 0°C and maximum heating temperature of 100°C the 300 m long casing would hot-yield in differential length ΔL of 1.44 ft according to equation 11 at the surface if it would be constrained.

$$\Delta L = -\alpha \Delta T L \tag{11}$$

Whereas,

α…Casing thermal expansion coefficient ($°F^{-1}$)

ΔT…Temperature change (°F)

L…Casing length (ft)

The safety factors are evaluated between the thermal compression loads and the pipe body yield strength, as it is lower than the joint strength. The reversed alternative would have yielded better results and actually would have been seemingly the right way to evaluate the compression subject, assuming that the threads on the casing couplings can withstand equal loads on compression as in tension, depending on the compression efficiency of the couplings. Not only is this approach wrong for low compression efficiencies regarding casing couplings, it does not show the collapse tendency and stress state of the constrained pipe body when subjected to thermal loading. Therefore the theorem of Van Mises regarding tri-axial combined loads including thermal effects is required.

2.2.2 Tri-axial Geothermal Casing Design

Conducting the biaxial geothermal casing design as a precursor in the previous segment, revealed the highest thermal compression stresses on the casing near surface level. There exist numerous conducted researches on the topic of thermal stress relationships between casing and cement interfaces via laboratory tests and Finite Element (FE) analysis for geothermal wells. The essential design loads for general casing design are tensile loading and fluid pressure, but according to S. Kaldal [19], in geothermal wells, high temperature loadings are the most severe. Based on FE analysis, S. Kaldal examined the stress relationships of cement and casing, with expanding trapped water between the casing cement interface while producing hot fluids These fluid pockets expand on the casing locally, posing a threat to its integrity. Figure 20 shows the casing failure at the collapse limit point until post collapse with and without cement support.

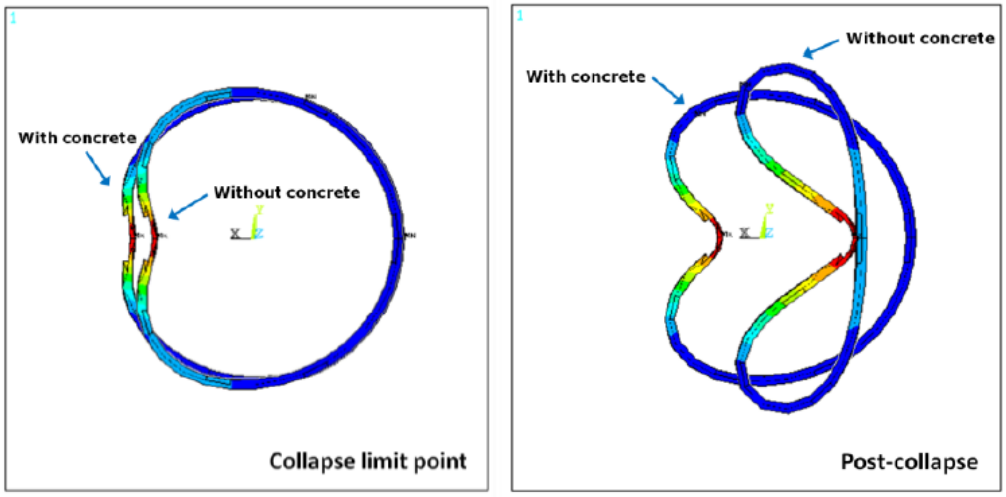

Figure 20: G. Kaldal's findings on collapse failure mode of K55 13 3/8 production casing ([19], p. 11).

One can clearly observe, that the magnitude of deformation is greater without cement support, due to the missing cement steel bonding mechanisms while setting casing. Another FE study conducted by Z. Shen [20] on casing collapse in High Pressure High Temperature (HPHT) wells gave deep insight on how the formulas affect the radial stress $б_{rr}$, the tangential stress $б_{\theta\theta}$ and the axial stress $б_{zz}$ in equations 12, 13 and 14.

$$б_{rr} = \frac{2(p_o r_o^2 - p_i r_o^2)(1-\nu) + \alpha E \Delta T (r_o^2 - r_i^2)}{2(r_o^2 - r_i^2)(1-\nu)(1-2\nu)} - \frac{2(p_o^2 - p_i^2)(1-\nu) r_o^2 r_i^2 + \alpha E \Delta T r_i^2 (r_o^2 - r_i^2)}{2(1-\nu)(r_o^2 - r_i^2) r^2} - \frac{\alpha E \Delta T}{2(1-\nu)} \left(1 - \frac{r_i^2}{r^2}\right) \tag{12}$$

$$б_{\theta\theta} = \frac{2(p_o r_o^2 - p_i r_o^2)(1-\nu) + \alpha E \Delta T (r_o^2 - r_i^2)}{2(r_o^2 - r_i^2)(1-\nu)(1-2\nu)} + \frac{2(p_o^2 - p_i^2)(1-\nu) r_o^2 r_i^2 + \alpha E \Delta T r_i^2 (r_o^2 - r_i^2)}{2(1-\nu)(r_o^2 - r_i^2) r^2} - \frac{\alpha E \Delta T}{2(1-\nu)} \left(1 + \frac{r_i^2}{r^2}\right) \tag{13}$$

$$б_{zz} = \frac{4(p_o r_o^2 - p_i r_o^2)(1-\nu) + \alpha E \Delta T (r_o^2 - r_i^2)}{2(r_o^2 - r_i^2)(1-\nu)(1-2\nu)} - \frac{\alpha E \Delta T (1-2\nu)}{(1-\nu)} \tag{14}$$

Whereas,

p_o…Collapse Pressure (psi)

p_i…Burst Pressure (psi)

r_o…Casing external radius (in)

r_i…Casing internal radius (in)

r…Radius at which stress occurs (in)

ν…Poisson's ratio (-)

α…Casing thermal expansion coefficient ($°F^{-1}$)

ΔT…Temperature change (°F)

E…Young's modulus (psi)

Based on these formulas, a tri-axial casing design according to the Van Mises failure criterion was conducted for the 13 3/8 in casing during the cement cure and a fully cemented string during temperature loading while heating the inner string.

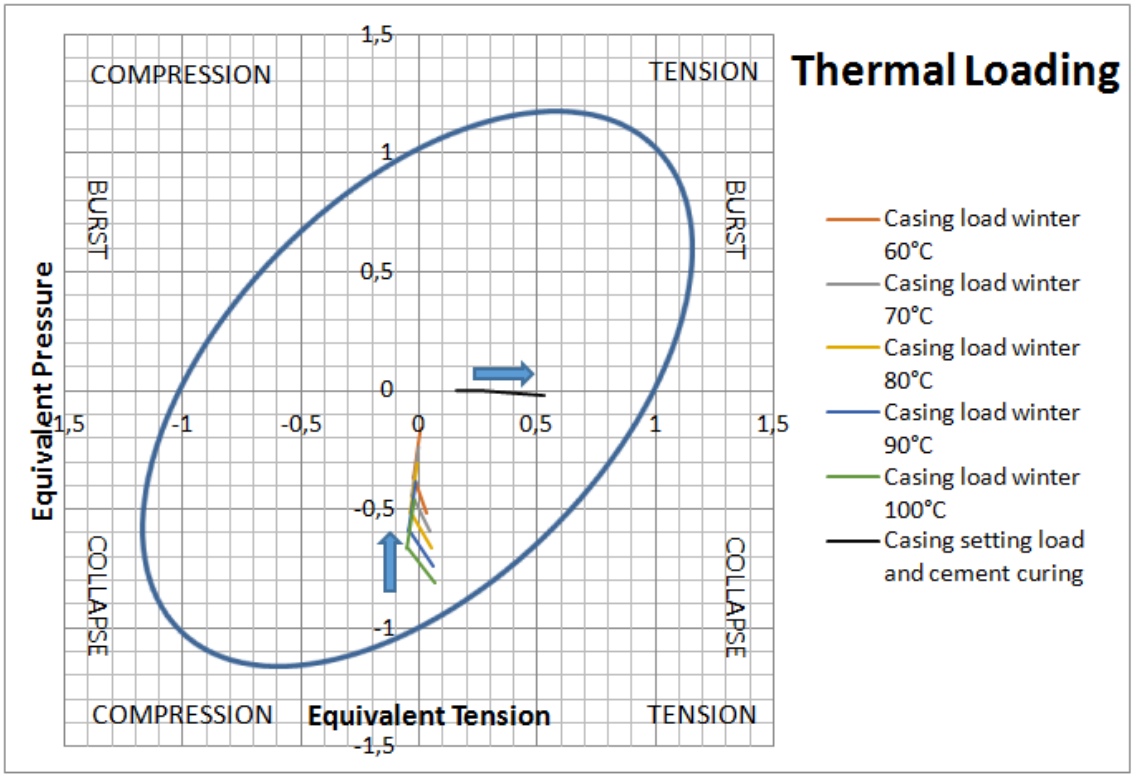

Figure 21: Van Mises stress equivalent of combined loads for the 13 3/8 ", 54,5 lb/ft, J55 surface casing after setting and cementing as well as thermal loads during the winter season. The arrow shows the hoop stress state of the casing from surface to bottom compared to the degraded yield strength of 52,250 psi. The failure envelope resembles a 100% (fraction) equivalent of the degraded yield strength.

Even though J. Wu [21] mentions, that for engineering purposes, the differential pressure between the external pressure and the internal pressure of the casing can be seen as zero, the yielding of the solid cement at the cement-casing interface was added to the outside pressure term p_0 of equations 4, 5 and 6 in order amplify the stresses to

imitate a more realistic approach without conducting an additional analog model for a cement sheet by rearranging equation 9 to a stress expression and exchanging A_t with the casing outside surface. The thermal and geomechanical properties for this modification were taken from Z. Shen [20].

During the cement cure, one can observe that the setting loads are dominantly tensional with a slight transition into the collapse region as the trend progresses towards the envelope, due to the hydrostatic pressure differential of cement and mud at the casing shoe, which are typical load curves for casing setting.

The incremental heating loads during winter are the focus of this failure envelope, as the other seasonal loads pose no threat to the casing integrity by comparison. The thermal loads show similar trends, starting from near the envelope on the tension-compression quadrant moving upward to the compression-collapse quadrant and stops approximately at a neutral collapse state. Without exceeding the envelope boundary, the major loads clearly feature a collapse stress state and the load path show highest stress concentrations at the surface.

Another concern arising, is the cement sheet integrity or rather, durability with respect to the long term cyclic thermal loading at the cement-casing interface. The cement sheet will experience radial compression as well as tensile loading exerted by the constrained casing string. This undertaking is primarily to visualize the stress magnitudes awaiting the cement sheet and narrowing down the unknowns. This seems to be more appropriate, as no actual cement specimens have been tested on these particular load cases. By exchanging the Poisson's ratio ν, young's modulus E and the coefficient of linear thermal expansion α from steel to cement properties, the equation 13 can be fitted to illustrate the maximum seasonal tangential stresses, as shown in figure 22.

The adapted parameters originate from the studies conducted by D. Stiles, with measurements performed on Class G with 40% By Weight of Cement (BWOC) silica flour, for thermal fortification [22]. The tangential stresses are purely thermal in nature, as the external and internal pressures are assumed zero in terms of fluid pressure and only a rearrangement of equation 9, in form of contact pressure from the expanding casing onto the cement is implemented for p_i, in order to visualize thermal interaction of cement and casing more clearly.

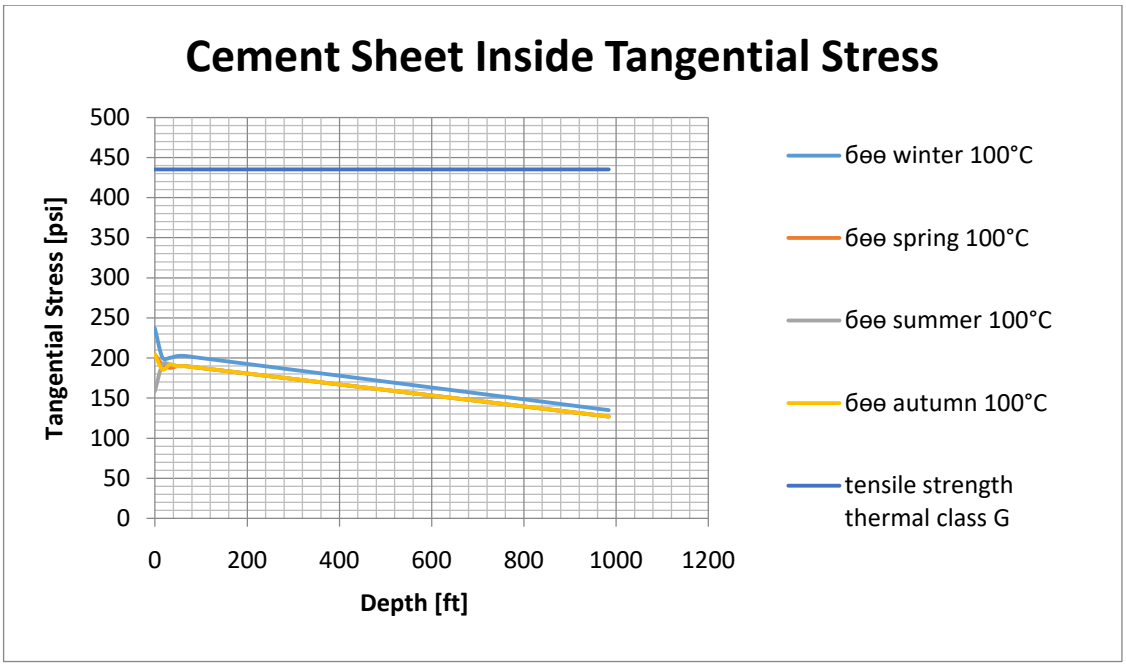

Figure 22: Seasonal tangential stresses at maximum thermal loading onto the cement sheet and its corresponding tensile strength.

According to D. Stiles, rising tangential stresses in the cement sheet, exceeding its tensile strength, strongly suggests the occurrence of tensile failure. This phenomenon is even more profound, with greater degree of decentralization between the casing and cement as stated by A. Albawi [23],where thermally cycled cement-casing specimens were post examined after a set of Computer Tomography (CT) scans, showing severe radial cracks and debonding compared to centralized casing samples. For this particular case, the adopted parameters and cement composition withstand the maximum requirements with significant amount of tolerance.

It is open for debate, if this surplus justifies the proposition of a thermally fatigue resistant cementation and can't be guaranteed at this point. Referring to the conclusion of N. Gaurina-Medimurec [24], geothermal cements are subjected to a wide variety of complex chemical interactions, which need to be considered for a particular situation. For this particular case, this means on one hand, 35 to 40 % BWOC of silica flour with 15 µm in particle size should be added to class G to prevent strength retrogression, should static temperatures exceed 110°C. On the other hand, calcareous environments pose serious problems for Portland cement systems even at ordinary temperatures, bearing in mind, that calcareous shale makes up most of the involved formation and silica flour should be reduced from 35 to 20 % BWOC in this case to improve cement resistance against carbonation.

Nevertheless, serving as a good vantage point, E. Nelson conducted extensive screening programs on class G and B Portland cement systems for geothermal applications, resulting in 6 recommended systems. One of the normal density slurries suggests class G with 35% (BWOC) silica flour and 54% BWOC of H_2O, to be amongst the best base formulations [25]. Referring back to D. Stiles' research, a low cement tensile strength by no means signifies an incompetent sealing barrier, as this matter is a function of the Young's modulus regarding the cement composition.

Quite the opposite is the case for flexible cements, as the tangential stress concentrations are reduced, due to the elastic nature of solid polymer additives, such as Vinyl Acetate-Ethylene copolymer (VAE) or Styrene Butadiene Rubber (SBR). Extending the base formulation by integrating these simple additives, may present an improvement to the arising fatigue problem. In order to assure the durability under thermal cyclic loading for the designated cement system.

Table 3: Cement system formulations for fatigue pilot testing.

Pilot Test	Cement Class	Constituents [%] (BWOC)		
Cement system 1	G	H_2O-54%	SiO_2-35%	-
Cement System 2	G	H_2O-54%	SiO_2-30%	VAE-5 %

For Health Safety and Environment (HSE) regulations alone, it is reasonable to conduct fatigue pilot tests along side of a chemical compatibility test for calcareous environments, regarding the proposed cement systems listed in table 3. Unfortunately these tests prove to be quite expensive and time consuming according to C. Kasinovski [26], who studied Class G cement fatigue for geothermal wells using experimental investigations.

The tests concluded that a cement sheet withstanding 100 low fatigue cycles is adequate for the service life of a well, which would offer a reference point in conducting the pilot test of cement system 1. Should the requirements on cement system 1 not be fulfilled, than cement system 2 should be tested, by gradually increasing the percentage of VAE and simultaneously decreasing the percentage of silica flour by the same amount to fulfil 100 low fatigue cycles or more based on C. Kasinowski. Other options must be considered regarding the constituents, if both pilot tests result in a negative manner, such as resin or self healing cement, illustrated by C. Thonhofer, to increase durability [27].

2.3 Subsurface Stock Component Modifications

It is a natural occurrence, to encounter design difficulties due to technical limitations during the initial stage. The resulting design, that fulfils the first 3 thesis objectives, come with problems of its own, which arises from the fact, that the 9 5/8 in casing is hung off into a circulating completion fluid. These issues are mainly caused by torsion and elongation of the inner string within the outer string during the drilling tests.

2.3.1 Considerations on Torsion

One problem considering the 9 5/8 in casing is the torsion, as it is customary to hang it off in one of the wellhead segments via casing hanger and no notable active torque loads are normally anticipated for an immersed string in completion fluid, except for casing drilling as a separate approach. In this particular case, it is assumed, whilst drilling off the cement, the torque source travels with depth within the cement fill, which transmits the load onto the casing, visualized in figure 23.

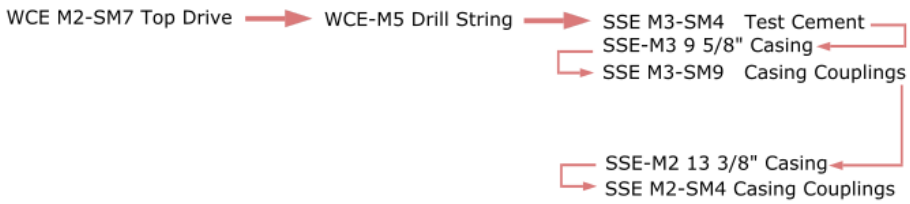

Figure 23: The load path amongst the component interfaces.

The magnitude of twisting, assuming a full torque transmission of the top drive's 7100 Nm as a worst case, increases with depth. The solution to this problem is shown in figure 24, by locking the casing in the direction of the bits rotation by means of a torque locking mechanism based on form closure.

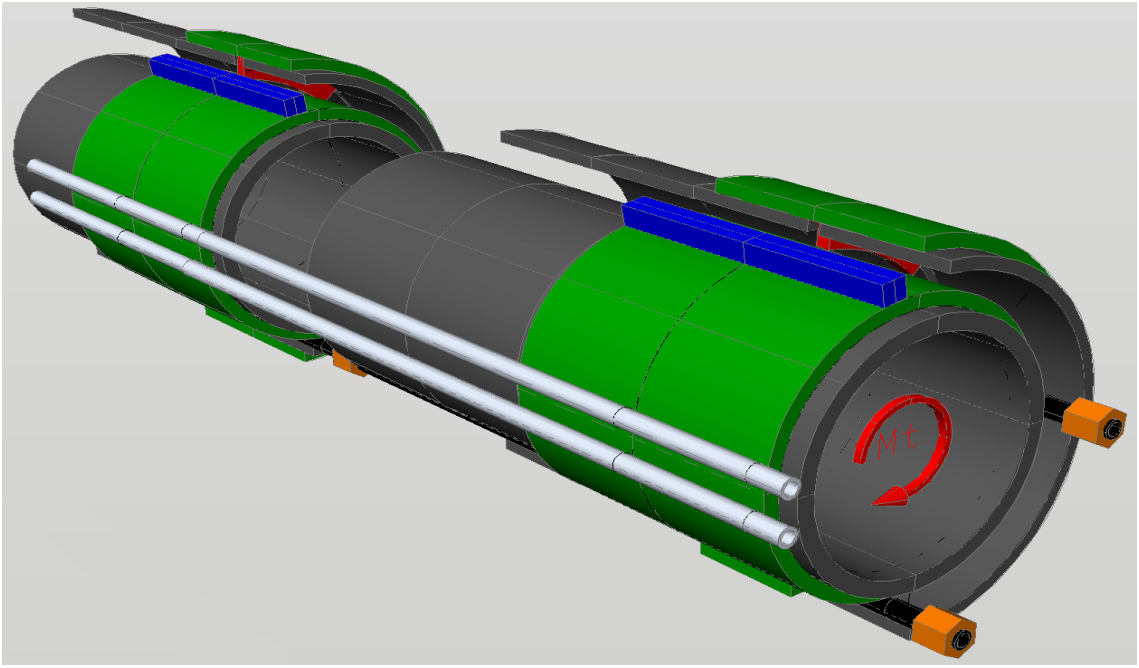

Figure 24: The 3D draft represents the positions of the first and last casing couplings paired together, forming the torque locking mechanism. The narrow clearance leaves only enough space for the maximum allowable hydraulic tube body to pass between couplings. Consequently the influx tube connectors have to reside before the restriction. The chosen alignment of the tubes are offset by 90 degrees, being behind the torque bushing (blue), in order to eliminate the risk of pinching any conduits as the inner string rotates onto the radial welded steel plate (red) on the outer coupling for its final positioning after the casing run.

Another issue to realize the torque lock, is the material pairing. It is highly recommended, to choose the same coupling material as the casing body. The 13 3/8 in J55 Short Thread Coupling (STC) is weldable, whereas for the 9 5/8 in L80 Long Thread Coupling (LTC) casing, only the low carbon alloy variations are appropriate for welding. The proposed welds on both sides are 5 mm thick in radial progression of the steel plate, centred in the free space between the two casing body ends after makeup. The welding inside the outer coupling is verified, by means of practical dimensioning in mechanical engineering [28], for allowable shear stress $\mathcal{T}_a$ in N/mm² compared with the maximum shear stress $\mathcal{T}_{max}$ in N/mm², according to equation 15.

$$\mathcal{T}_a = \nu_1 \nu_2 \frac{R_{eh}}{\sqrt{3}} \geq \mathcal{T}_{max} = \frac{3F}{2A_n} \tag{15}$$

Whereas,

ν_1…Dynamic load coefficient for T-joint (-)

ν_2…Static and dynamic coefficient for weld grade (-)

R_{eh}…Upper yield strength of material (N/mm²)

F…Force (N)

A_n…Weld throat area (mm²)

This particular design set up is simple and effective, as it can withstand double the torque amount, imposed by the top drive and is a function of the throat area. It can be easily fortified by increasing the platelet's radius and the accompanied welding. The torque bushing is welded parallel to casing axis on the circumference of the 9 5/8 in L 80 LTC coupling. The t-joint is welded with a 5 mm fillet weld along the entire length of the torque bushing on both sides. Even though the positioning of the weld is not optimal for bending and shear loads, compared to the alignment of the radial welded steel plate, the fillet length makes up for these short comings. The equivalent stress $б_v$ in N/mm² compared to the allowable stress according to equation 16.

$$б_w = \frac{\alpha_w R_e}{Y_m} \geq б_v = \sqrt{{б_b}^2 + {\mathcal{T}_h}^2} \tag{16}$$

Whereas,

Re… Yield strength of coupling material (N/mm²)

α_w… Coefficient for hub material (-)

Y_m… Safety factor for uncertainty (-)

$б_b$… Bending stress (N/mm²)

$\mathcal{T}_h$… Shear stress (N/mm²)

This particular design, withstands momentums 4 times greater than the applied torque, should it be considered to increase the top drive's power output.

2.3.2 Considerations on Elongation

The API 5CT casing lengths usually have an average of 28 feet, but can be varied upon costumer agreement and are delivered on the rig site with one coupling already installed. The implied casing lengths for this application are 12 m including one casing coupling for both casing strings as these lengths are the most common, assuming both being under tension due to self weight, before the cement cure, resulting in a flush alignment of the both upper most coupling edges as shown in the 3D model. This ensures that the torque locking mechanism will not pass each other out. Furthermore, the nominal weight, diameter, material grade are different for each string and have different impact upon strain, in terms of stretching due self weight and thermal expansion. Figure 25 presents stress strain curves of different casing material grades recorded in the published work of N. Morita, analyzing short casings during plastic deformation [29].

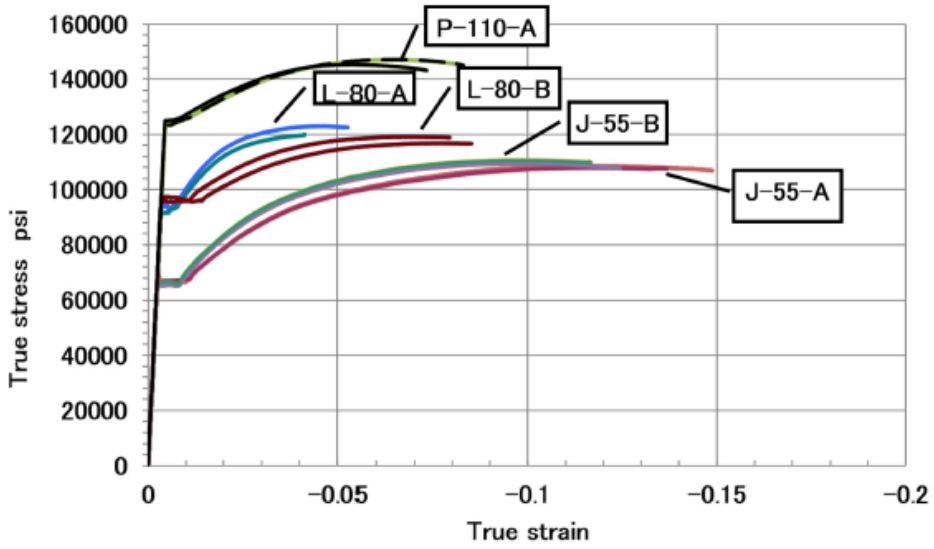

Figure 25: Stress strain curves measured on short casings for true stress and true strain ([29], p.5).

By implying Hooke's law in equation 17 and the already expressed linear thermal expansion in equation 11, this time as a positive term, because the casing is allowed to expand, one can evaluate the total elongation ΔL of the 9 5/8 in casing, whilst only equation 17 is used for the 13 3/8 in casing, assuming its position is preserved after cementing.

$$\frac{F}{A} = \frac{\Delta L}{L_0} E \tag{17}$$

Whereas,

F…Buoyed weight of casing (lb)

A…Cross section area of pipe (in^2)

L_0…Initial Length (in)

ΔL…Elongation (in)

E…Young's elastic modulus (psi)

Subtracting each elongation for every casing segment with one another, gives the offset per casing coupling with depth. Referring to figure 24, the total offset movement results in approximately 47 mm, shifting the last coupling position of the 9 5/8 in casing upward compared to the first coupling. This shows, that the form lock is verified for all coupling positions, not passing each other out.

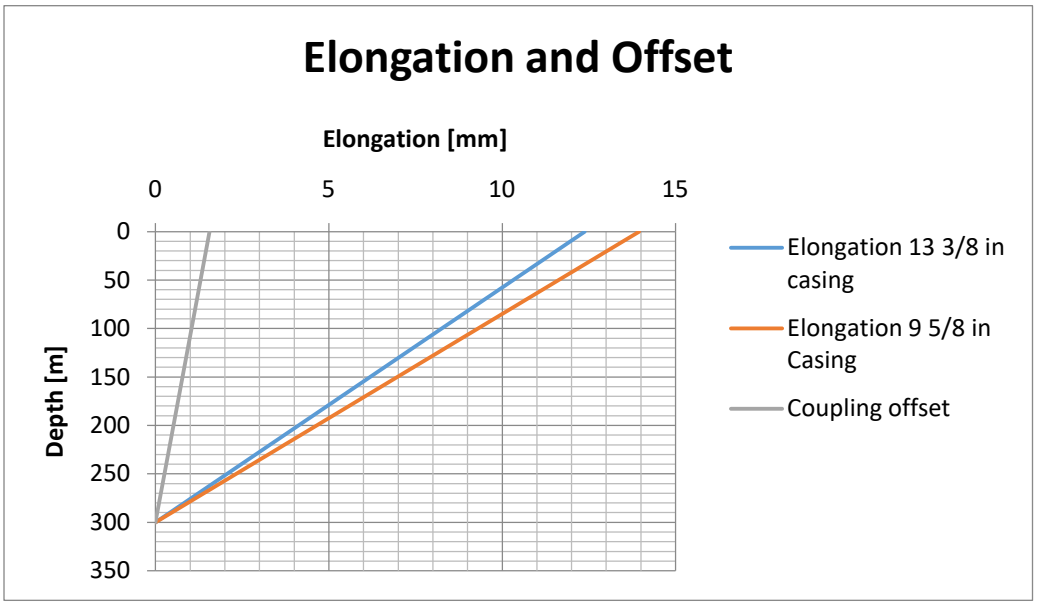

Figure 26: The magnitude of elongation is greater for the 9 5/8 casing string. The stretch due to string weight is more dominant than the thermal expansion and is more prominent for the upper most casing segments. The coupling offset can be observed incrementally for each coupling pair with depth.

This also means, that the influx tube lengths have to be scaled accordingly for a strain free installation at all times. A further problem arose through the limited clearance between both casing strings, regarding the influx conduit diameters, considering flow rate and back pressure, due to fluid friction. The influx conduits are made up of fragmented tubes and connections shown in figure 27, normally used for hydraulic circuits [30].

Figure 27: Fortified hydraulic tube segments of durable steel spiral layers, combined with threaded couplings. The check valve accompanies the angle port and represents the lower most segment of the design. The influx application is a closed circuit, leading into the pup joint through the casing annulus, whereas the heating application is an open circuit in the casing annulus ([30] pp. 3, 67).

Each influx tube is secured with one check valve, to insure there is no reverse flow into the tubes with a working pressure rating of 350 bar and opening pressure response of 0.1bar [31]. The technical parameters of both applications are summarized in table 4.

Table 4: Summary of conduit parameters residing within the casing annulus.

Specification	Influx Conduits	Heating Conduits
Temperature Rating	150 °C	700 °C
Pressure Rating	350 bar	207 bar
Connector Diameter	30 mm-M20x1.5	-
Tubing Outside Diameter	17 mm	18 mm
Tubing Inside Diameter	10 mm	12.7 mm

More severe, was realizing the setup of filling the inner string with drillable test cement without plugging the injection ports and initiating kicks while tripping. The design configuration which solved these issues is presented in figure 28.

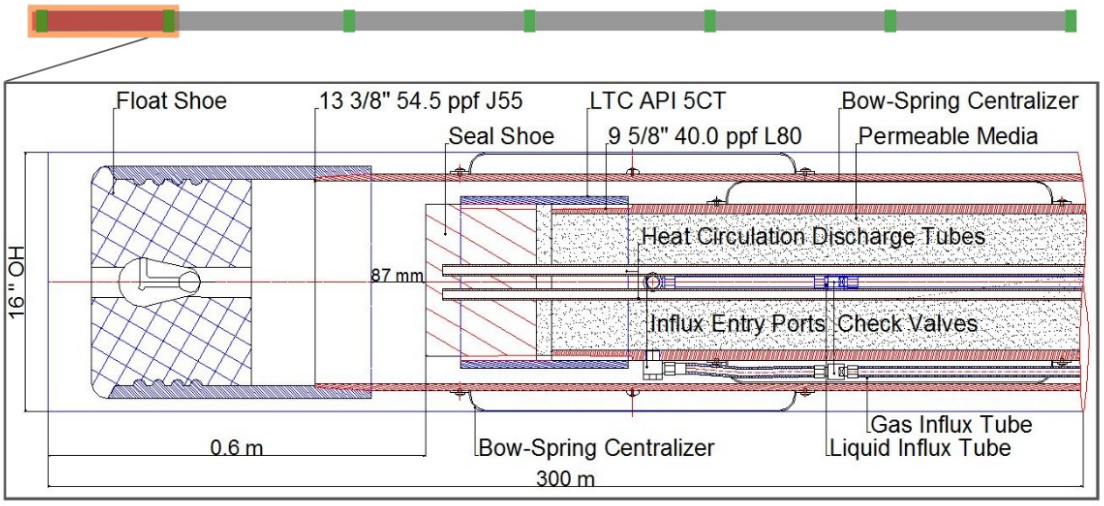

Figure 28: The cutaway drawing resembles the last casing segment. The 9 5/8 in pup joint is 0.6 m shorter than the predefined regular casing length.

By installing a regular long threaded coupling and the designed seal shoe made of solid steel, the clearance to the upper edge of the stab in float shoe results in 87mm, accounting for thermal and buoyed weight stretching of the inner string. It is intended to fill up the outer string to this level with cement residue to fortify the drillable material of the float shoe, when the inner string elongates upon contact. These casing alignments represent the default position of cement free 9 5/8 in casing.

The default position as mentioned in figure 28 shows the inner string under tension as its natural state. The thermal expansion under 100°C, as well as the buoyed weight

stretch, had been accounted for, with an allowance of 87 mm for further elongation. A full test cement fill elongates the casing and tags it on bottom, keeping the string under tension, which eliminates the potential of buckling completely for this application. Once WOB is established, the compressive loads are carried by the cured cement, while the casing stays under tension.

The pup joint is deployed with a complete fill of quartz gravel as a permeable membrane, with a grain size range of 3 to 5 mm and a bulk density of 1.6 t/m^3 [32]. It can be cemented upon, with foam cement as a primary barrier, as it is not as intrusive as regular cement slurries, regarding the injection ports located approximately 9 m further down. The equations 18, 19 and 20, resemble the radial stress $б_{rr}$, the tangential stress $б_{\theta\theta}$ and the axial stress $б_{zz}$ of the 9 5/8 casing, under unconstrained conditions according to J. Wu [21].

$$б_{rr} = \frac{P_b - P_a}{b^2 - a^2}\frac{a^2 b^2}{r^2} - \frac{P_b b^2 - P_a a^2}{b^2 - a^2} \tag{18}$$

$$б_{\theta\theta} = -\frac{P_b - P_a}{b^2 - a^2}\frac{a^2 b^2}{r^2} - \frac{P_b b^2 - P_a a^2}{b^2 - a^2} \tag{19}$$

$$б_{zz} = \frac{F}{A_s} - 2\mu\frac{\Delta P_b b^2 - \Delta P_a a^2}{b^2 - a^2} - \alpha E \Delta T \tag{20}$$

Whereas,

P_b… Casing external Pressure (psi)

P_a… Casing internal Pressure (psi)

a… Casing internal radius (in)

b… Casing external radius (in)

r… radius of occurring stress (in)

F… Buoyed weight (lbs

A_s… Casing cross-section area (in^2)

μ… Poisson's ratio

α…Casing thermal expansion coefficient (°F^{-1})

E… Young's modulus (psi)

ΔT… Temperature change (°F)

By implementing these equations within the tri-axial casing design and increasing the tangential stress by the top drives torque, the Van Mises failure criterion can be displayed for an immersed casing in Potassium Chloride (KCL) based completion fluid of 10 ppg and the potential of withstanding internal pressures exerted by heavy cement slurries of 22 ppg [33] while curing, as shown in figure 29.

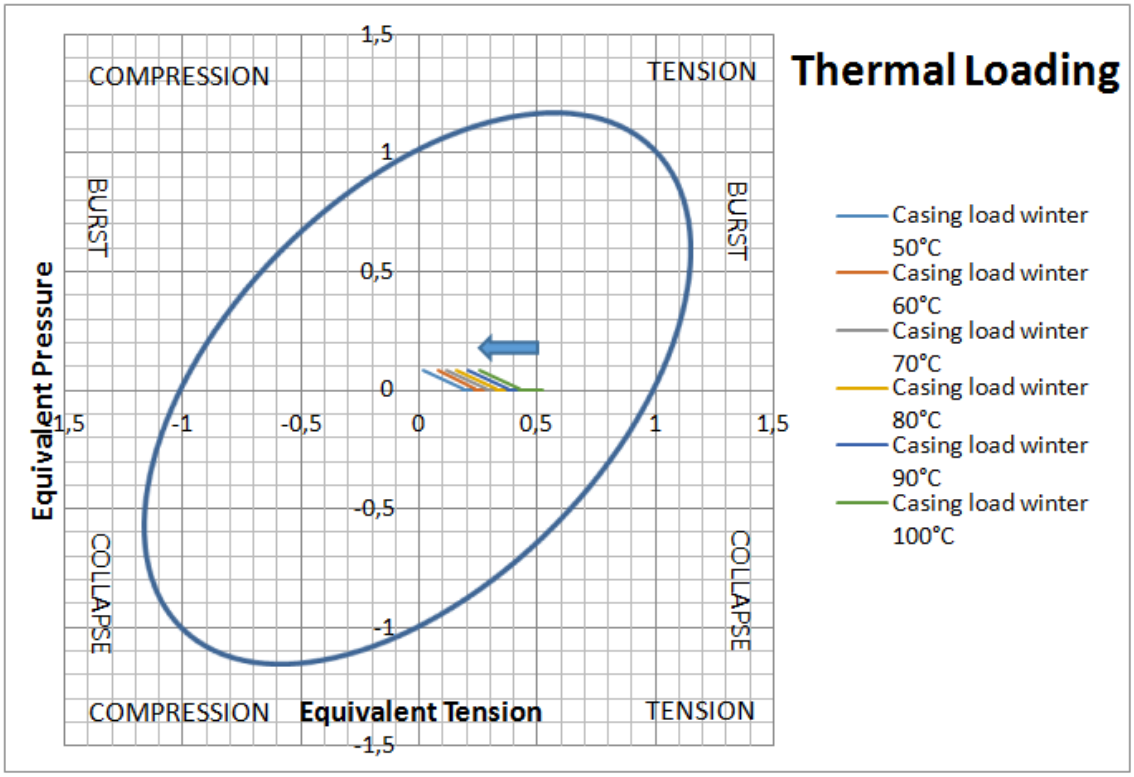

Figure 29: The Van Mises failure criterion shows the load path of the 9 5/8 in casing while curing heavy slurry, under temperature loading from 50°C up to 100°C. The arrow shows the stress state from surface to bottom. The degraded yield strength is 76,000 psi and resembles the equivalent failure border.

The stress check is displayed for the winter season, as it poses the greatest differential temperatures for the inner string, especially near the surface. The stresses per temperature stage, show the load paths rising towards the envelope, from bottom to surface, having the highest tangential stresses near surface. The combined stress state resides within the tension-burst quadrant.

2.3.3 Considerations on Installation

The fact being, that this well design is out of the ordinary, presumes extra ordinary preparations for installation. A usual casing run on land rig applications, are basically not much different as running in drill pipe, where the appropriate connection torque needs to be established and the pipe body alignments are ignored. Unfortunately, this convenience can't be carried out onto this particular operation, as the radial positioning between coupling and casing is significant. The end position of the coupling relative to the casing is dependent on thread pitch and make up torque. This fact is evident for both casing strings, regarding the consistent radial alignment of the torque locking mechanism with depth. The steel plate positioning can be managed on the rig floor continuously prior welding, after the connection torque has been established and the casing is hung off. This also means, that carrying out a cement job by means of a bottom and top plug becomes obsolete, due to the obstructions by the steel plates inside every coupling. That is why an inner string cementation as a deployment method is proposed for this step and described in figure 30.

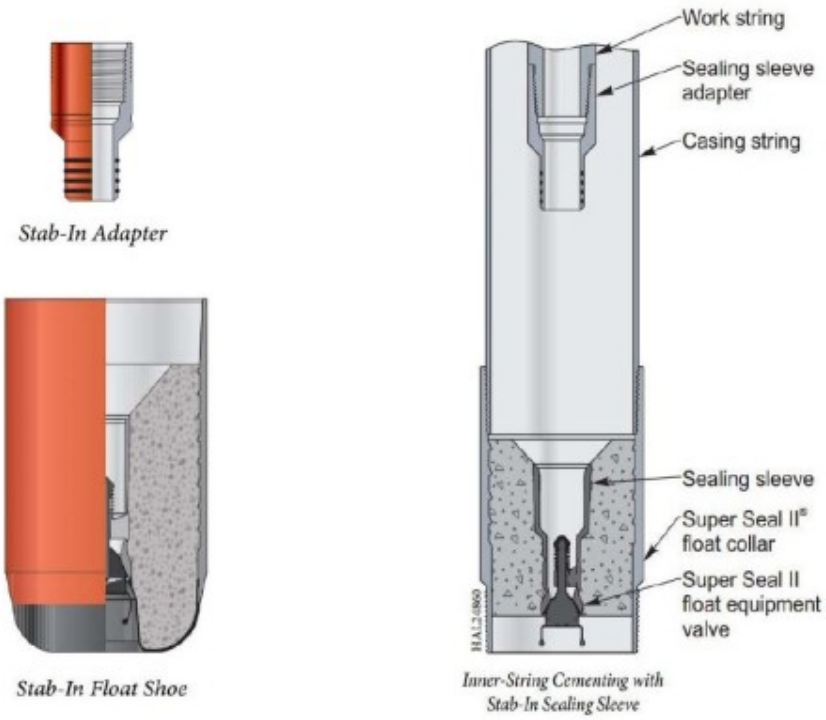

Figure 30: The inner string method is a common practice to cement large size casings and requires a drill pipe with a stab in adapter at the bottom, which is guided into the stab-in float shoe ([34], p.459).

The cement is pumped through the drill pipe with a wiper plug, which is displaced by drilling fluid. The proposed mixture of "cement system 1" for pilot testing, mentioned earlier, is addressed at this point. Following the precise BWOC of constituent percentages with respect to the open hole volume, would result in a 16 ppg slurry for this application, which is not justifiable regarding the fracture pressure gradient as seen in the mud weight window in figure 13. According to J. Craig, a mud-cement density difference of at least 0.5 ppg should be given, to prevent movement, when the pump stops [35]. The new slurry density is designed with 11.5 ppg, with unchanged BWOC of silica flour, but a greater water cement ratio of 10 gal/ sack. This reformulation yields 2.1 ft^3/sack of cement slurry, expressed in more detail in table 5.

Table 5: Cement system reformulation for pilot testing and proposed deployment based on API cement bulk weight of 94 lb/sack.

Constituent	Class G	Silica Flour	Sodium Chloride	Water
SG	3.14	2.65	2.16	1.00
BWOC %	100 .00	35.00	5.00	88.60

Solving the radial positioning problem of the 9 5/8 in casing, requires the same steps as with the 13 3/8 in casing. The steel plates are welded inside the coupling after the makeup torque is established and positioned in a defined orientation for alignment. While the 9 5/8 in casing is run into the 13 3/8 in casing, an angle offset needs to be chosen when the torque bushing is welded in order to not to hit off the radial steel plates already in place. This orientation need to be preserved throughout the entire operation. The proposed installation procedure is sketched in figure 31.

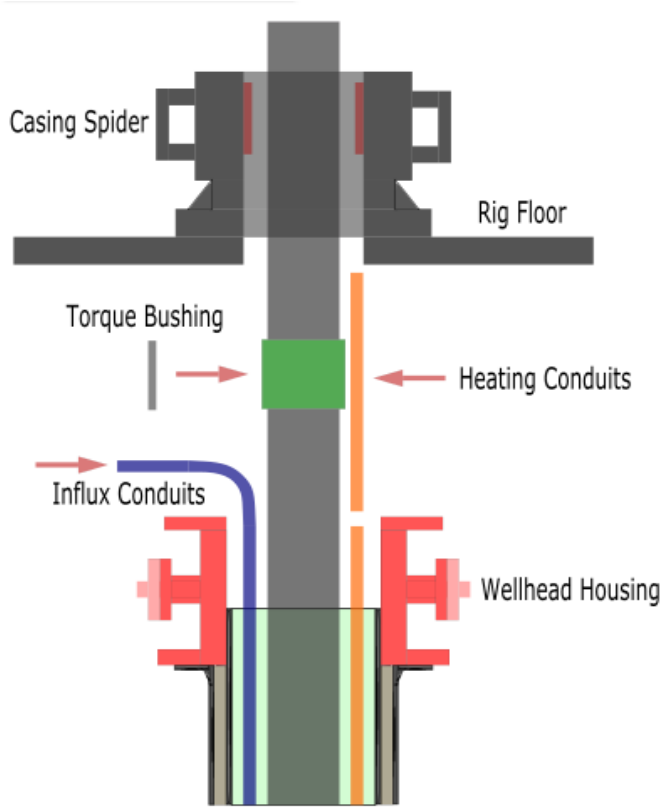

Figure 31: The torque bushing is welded on the coupling after passing the spider. The flexible influx conduits make it possible to be inserted in sideways into the wellhead housing and lowered down together. As for the steel heating conduits, the tube lengths need to be fitted on site, depending on the radius of bending with respect to the height of the rig floor.

It is uncertain if a fully mounted torque bushing at the rig floor can pass the clearance of an open spider. Should this be the case, the installation can be executed on the rig floor along with bow-spring centralizers, as it is more convenient. For a vertical well, one centralizer is used for every two casing joints.

The amount of centralizers required, in order to centre and dampen the inner string during drilling test procedures, depends on the stiffness and side forces the bow-spring can exert onto the wall of the outer casing, not to mention the obstruction issue by the steel plates. Therefore it is proposed to use more centralizers per joint, but with fewer bows. Another option would be to install thermoplastic centralizers, shown in figure 32.

Figure 32: An option to the spring bow centralizers would be thermoplastic centralizers, where form and properties can be customized according to the application and features slots for tubing and control lines ([36] p.2)

Neither way, this dampening topic needs to be examined more thoroughly and is not within the scope of this thesis. To ensure a high welding quality of torque bushings and steel plates, it is proposed to locally pre heat the casing couplings according to the metallurgical properties if necessary.

2.4 Surface Stock Component Modifications

The changes performed on the wellhead, are intended to enable a permanent drilling operation of the intermediate section. This means, that, the wellhead housing for the surface section is already installed in place, accompanied by the drilling spool as well as annular Blow Out Preventer (BOP) for well control measures as a permanent rig up setting. As the stacking height of the wellhead components, dictate the resulting height of the rigs substructure, it was essential to keep this as low as possible, without restraining any of the individual components regular functions. Figure 33 shows, a typical rig up setting on land for a 13 3/8 in x 9 5/8 in x 5 ½ in casing program.

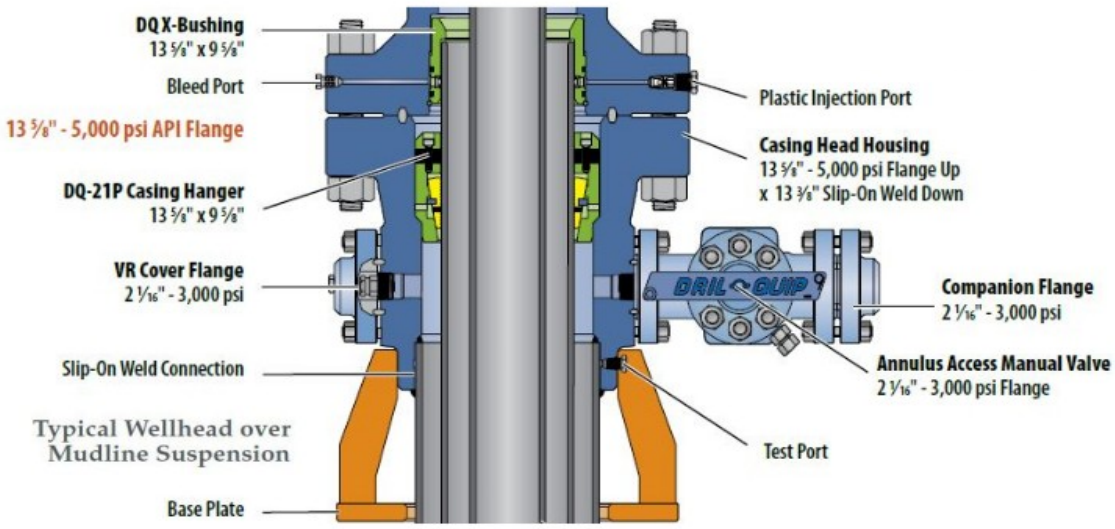

Figure 33: The casing head housing is a slip-on type, welded onto the surface casing and supported by a base plate. The connection of bottom to top flange, from the casing head housing onto the intermediate casing spool is established by 13 5/8 in API Flange rated with 5000 psi ([37], p 4).

One can observe that the 9 5/8 in casing is hung off in the casing head housing and extends into the casing spool where it is furnished with the "DQ X-Bushing". The side outlets are equipped by a cover flange on the left and a covered "Annulus Access Manual Valve". These mentioned component settings are the basis of comparison for the actual rig up setting, to highlight the differences caused by the modifications depicted in figure 34.

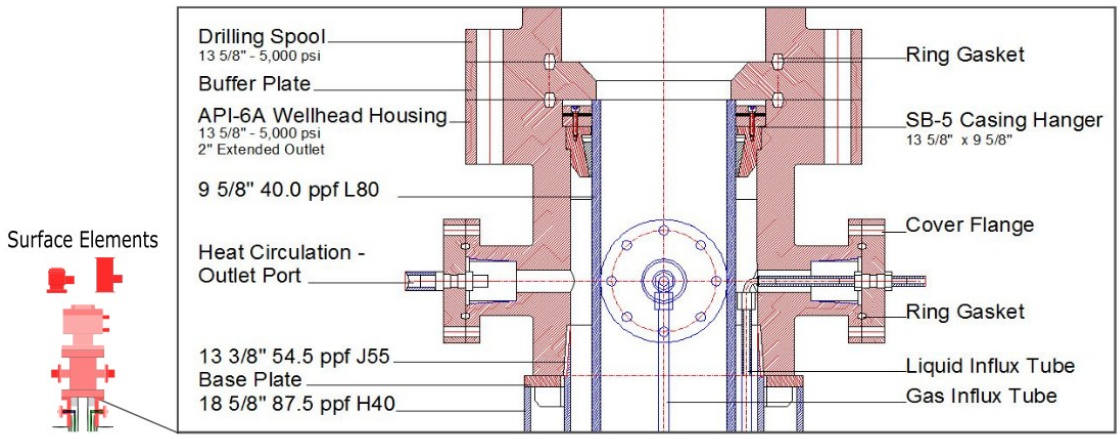

Figure 34: The cut away drawing resembles a threaded well head housing, with four side entry ports instead of two. The connections for bottom and top flanges for the permanent installation of the wellhead housing, drilling spool and annular BOP are based on 13 5/8 API and pressure rated with 5000psi.

In order to reduce height, the additional casing spool to support the 9 5/8 in casing was excluded, compared to the regular approach. Bearing in mind that the casing stretch upon contact as illustrated in the previous chapter in figure 28 as well as the buoyed weight load would result in 12,144 psi overall axial strain onto the casing hanger according to Hooke's law. This is 11 % of the pipe body yield strength and is

significantly lower than the allowed 50 % of the "IC-series" [2] in figure 35, sufficiently complying with the load limits. However it is uncertain how this hanger type would behave under temperature loading. For this reason, the SB-series was taken into account.

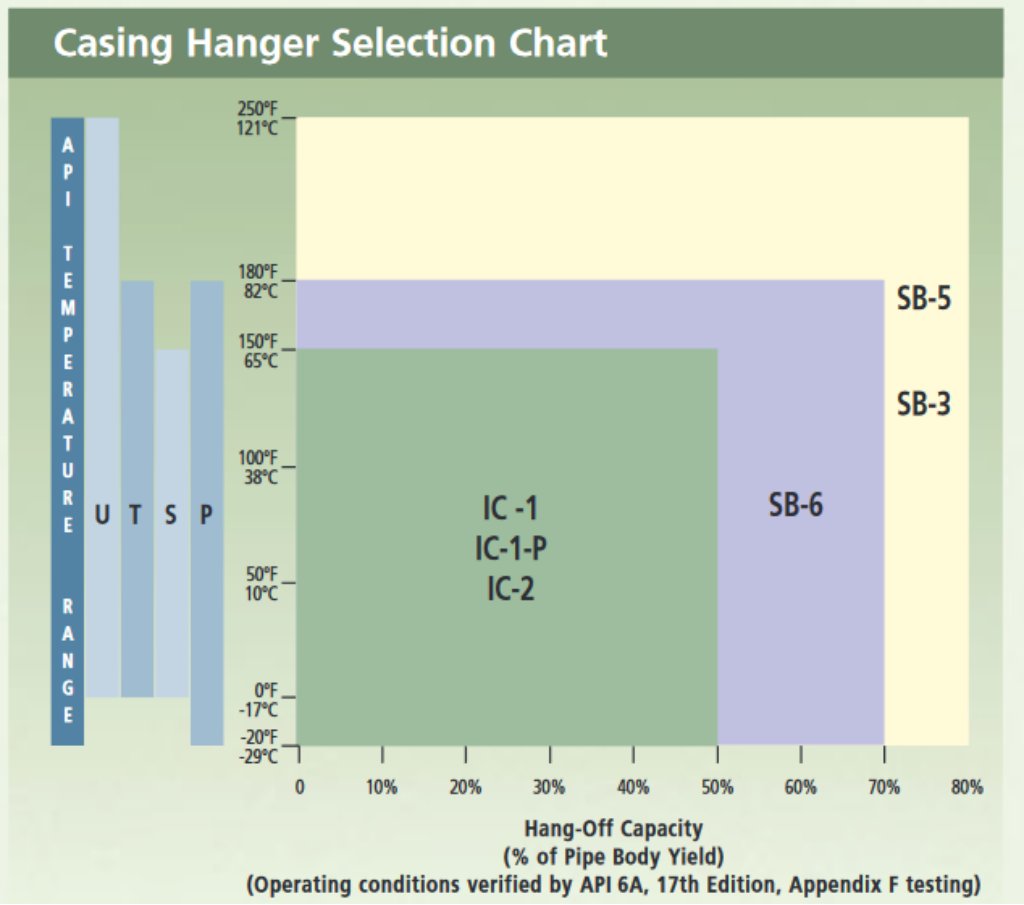

Figure 35: Casing hanger selection chart, according to Cameron Conventional Wellhead Systems ([38], p. 1.).

The casing bushing, normally housed within the casing spool, as illustrated in figure 33, is exchanged by a regular buffer plate depicted in figure 34, preserving the protective function for the casing and casing hanger, when the bit is guided in as well as anchoring the assembly when the drill string is pulled. The annulus is sealed with the built in sealing element in the casing hanger and assisted with the steel to steel sealing between casing and buffer plate. The influx and heating tubes, find their entry through cover flanges, which are initially blind flanges furnished with threaded bores, matching the tube connectors mounted on the side entry ports of the wellhead housing. Both the buffer plate and the modifications on the blind flanges are simple components and can be easily realized in house.

2.5 Well Construction Equipment

This chapter contains the re-utilization of equipment, once in service for the former bit test stand, in conjunction with a considerable amount of reconstruction. Two sub chapters are devoted to the functionality of the substructure and mast. It also includes the extension of new equipment needed to realize the objectives, however only the essential modules and sub modules are presented.

The layout of the entire testing facility is shown in figure 36, where components are partially indoors. The majority of the drill rig is left out in the open, as well as equipment, which are not prone to weathering. The L-shaped design of the building was taken from a reference workshop located in Leoben [39].

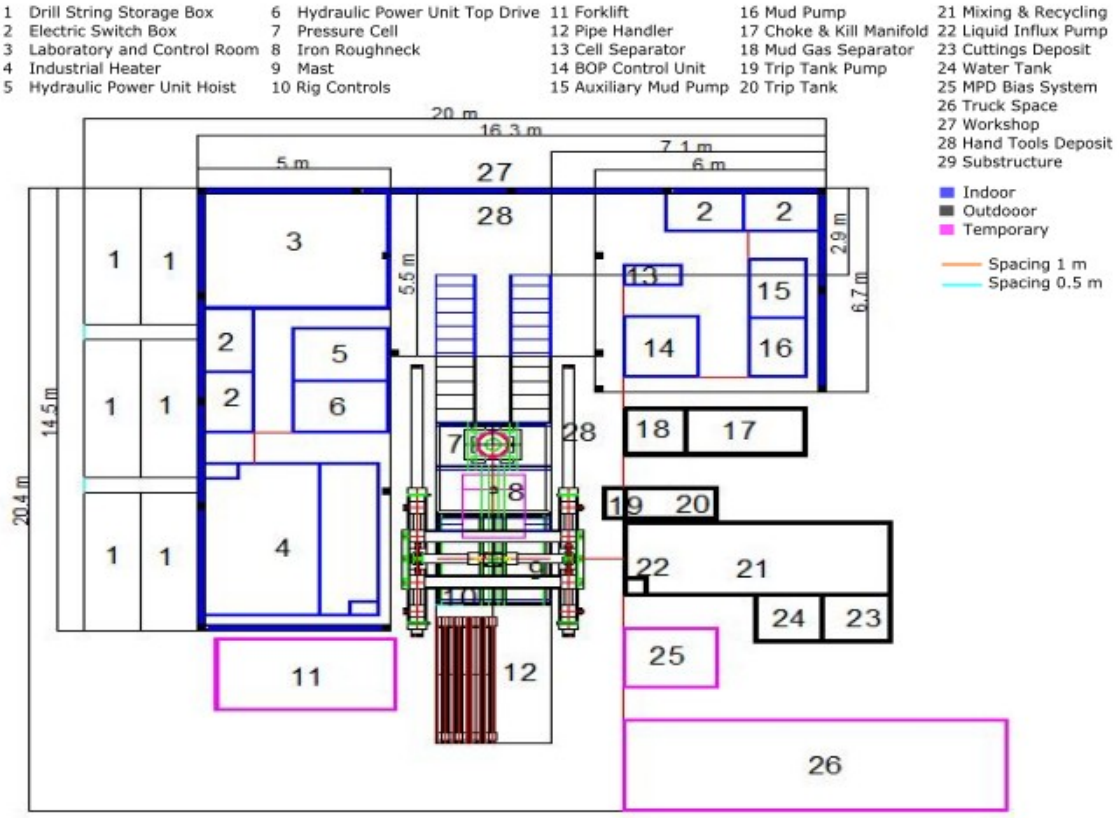

Figure 36: The layout configuration is similar to a full-fledged drilling rig. As former hydraulic power units were designed to be indoors, a sheltering structure became necessary and offers the opportunity to establish a small independent laboratory within the complex, for measurements and evaluations of the test cement.

The dimensions for the workshop are given in absolute values on which the positioning of the drill rig is based on at the outer corner of the right stair. From this point on, the spacing for every piece of equipment is continued incrementally, with respect to its own dimensions on a concrete foundation.

2.5.1 Redesign

The frame work of the mast and substructure are based on semi-finished materials, assembled by a combination of welded and bolted connections, common to general mechanical engineering. There is a vast extent of possibilities and techniques in performing different kinds of strength analysis on specific areas of these structures. However the practical approach common to general mechanical engineering is applied in this case. Like any other construct, loads get channelled and diverge into one component, due to the design. These critically stressed elements are the main focus of evaluation.

2.5.1.1 Substructure Design

The loads in this chapter are predominantly static in nature. The dimensioning and material strength selections were performed based on the strain sources, depicted in figure 37.

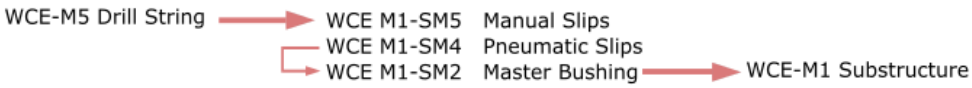

Figure 37: The load path between mechanical interfaces for the substructure when the string is hung off.

The rigs substructure provides an elevated working environment, primarily designed around the surface well elements as a permanent platform, with an attachment to incorporate the pressure cell as sketched in figure 38. The steel beams involved are listed in table 6 [40].

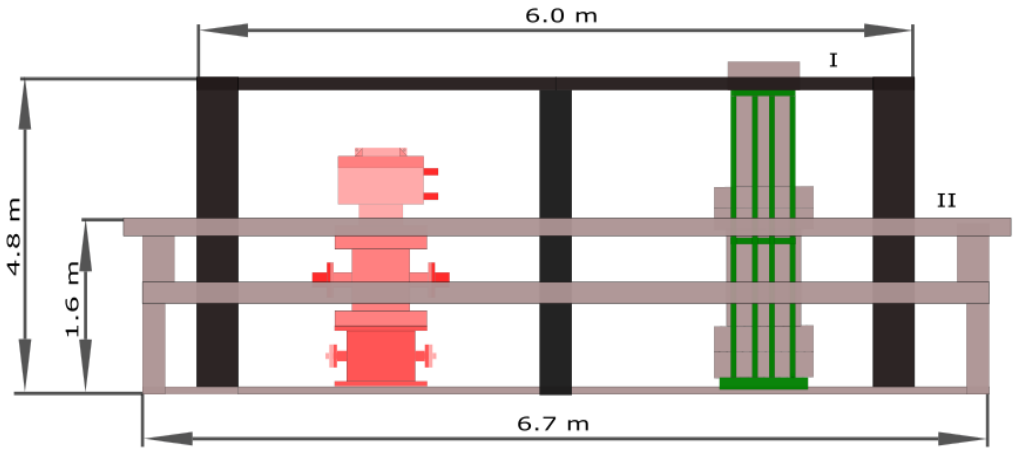

Figure 38: The substructure encloses both the well stack on the left and the pressure cell on the right. The frame work (I) is for elevation and is 4.8 m high, 3m wide and 6m long. The grey structure (II) serves as guide rails and supports a movable mast, both combined as one unit.

Table 6: Summary of the substructures semi-finished beam profiles ([40], pp. 43-84).

Profile		Dimensions (hxbxt) [mm]	Axial Section Modulus [cm³]	Material	Standard
1	Angle Steel	45x45x5	2.2	S235JR	EN10025
2	U-Steel	400x110x18	1020	S235JR	EN10025
3	I-Steel	450x170x24.3	2040	S235JR	EN10025
4	I-Steel	400x307x21	5571	S235JR	EN10025
5	Flat Steel	500x40	-	S235JR	EN10025

2.5.1.2 Master Bushing

The socket for the master bushing is a square welded seat, made and supported by I-beams, listed in table 6 at position 3. The master bushing is a solid body pin drive type bushing normally inserted into a rotary table. In this application it is inserted and locked into place with steel plates.

Figure 39: The bushing comes with 3 different insert bowls, one capable of handling 2 3/8 in to 8 5/8 in OD tubulars. The master bushing can be equipped with pneumatic slips at the corner bores or a bit breaker adapter plate ([41],[42]).

The designed load onto the bushing and subsequently onto the 2 supporting beams, is exerted by a basic drill string assembly for vertical wells as shown in figure 40.

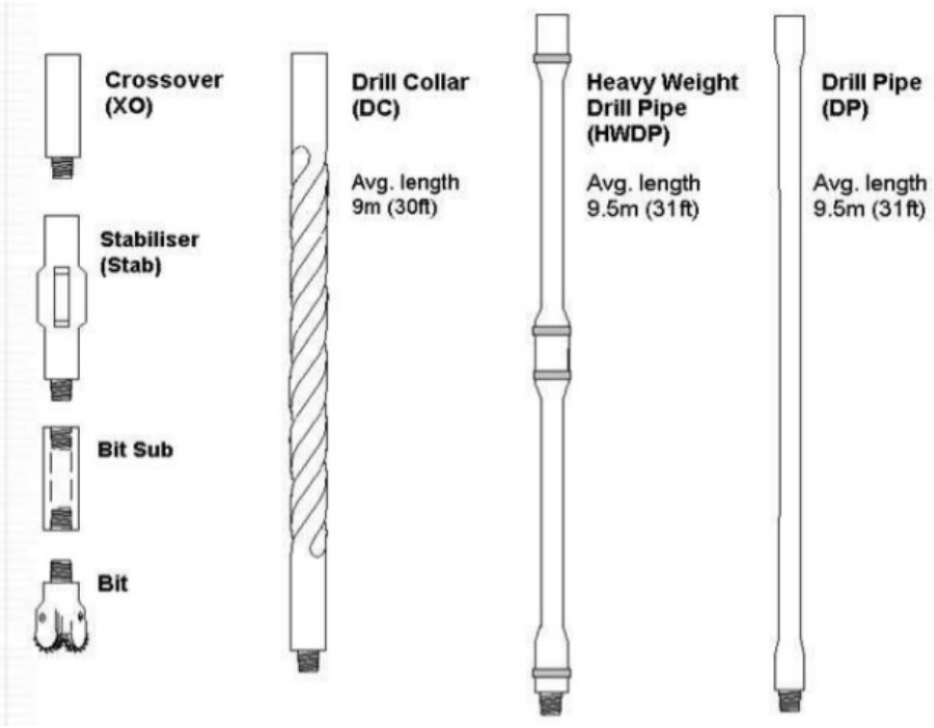

Figure 40: A typical vertical drill string assembly ([43] p.13).

The drill string components result from the design, to drill soft to medium formation categories with a compressive strength of 2,000 to 20,000 psi according to the bit manufacturer. Taking a 8 1/2 in bit as a reference, by implying the manufacturers recommended benchmark, ranging from 2,000 to 4,500 lbs/in would result in a required Weight On Bit (WOB) of 27,625 lbs [44]. Tackling this formation strength with a tri-cone bit, requires higher WOB and therefore an overall heavier string as with a PDC. The equation for a buoyed Bottom Hole Assembly (BHA) and Drill Collars (DC) required for WOB is shown in equation 21 expressed as total length in mud in ft.

$$total\ length\ in\ mud = \frac{WOB \times BF}{Ws\ \times 0.85} \tag{22}$$

Whereas,

WOB…Weight on bit (lb)

BF…Buoyancy factor (-)

Ws…Nominal weight (lb/ft)

Setting the neutral point within the drill collars leaves 85% of this segment in compression and the rest of the string under tension and results in a drill string for gaging purposes listed in table 7.

Table 7: Specifications of the drill string elements for designing the supporting beams of the master bushing.

String Type	DP-S	HWDP	DC
API Standard	NC 50	NC 50	NC 50
Makeup Torque [ft-lb]	38,040	26,800	26,675
OD [in]	5	5	6 3/4
ID [in]	4 9/32	3	2 13/16
Ws [lb/ft]	19.5	50	100.7
Length [ft]	527	62	372
Piece	17	2	12
Σ weight [lb]	10,276.5	3,100	37,445.5

2.5.1.3 Substructure Beam

The weight exerted onto the beams is illustrated in figure 41, which resembles the most critical area of this structure.

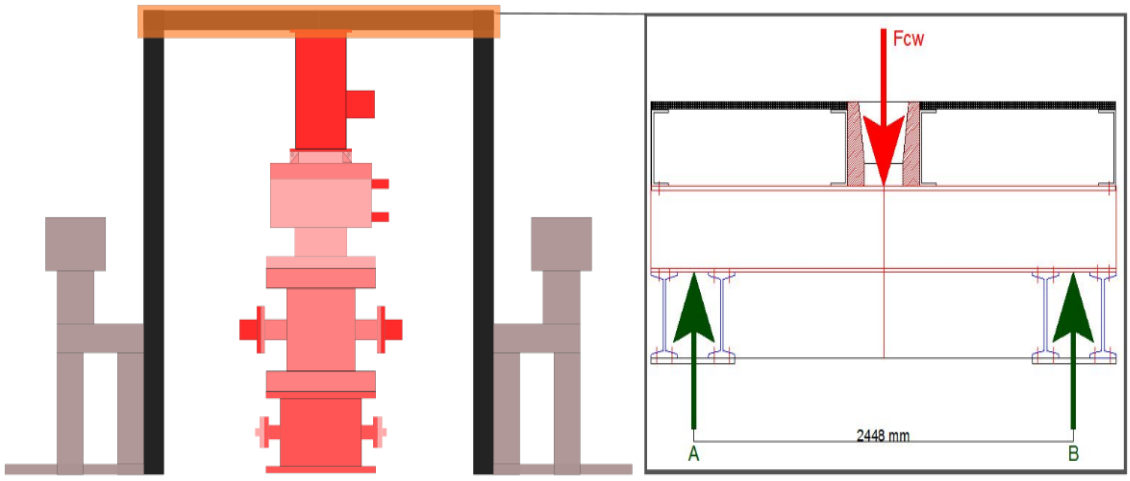

Figure 41: F_{cw} is the weight of the entire string hung off onto the master bushing. The sustaining two beams (red) are depicted on the right partial cutaway side view with 3m in length.

The allowable bending stress $б_a$ for this material under static loading is 180 N/mm² [45], dimensioned after the equation 22.

$$б_b = \frac{F_{cw}\, l}{W_b} \leq б_a \tag{22}$$

Whereas,

F_{cw}…Drill string in air (N)

l…Lever arm (mm)

W_b…Section modulus (mm^3)

The resulting calculations indicate that the selected beams can easily support triple the designed weight, offering enough opportunity to hang off heavier test strings in various combinations.

2.5.1.4 Iron Roughneck

The entire pipe connections can be realized within the OD range of 4 ¼ in to 8 ½ in by an ST-80, or 4 in to 9 ¾ in by an ST-100 Iron Roughneck from NOV, featuring maximum make up torques of 60,000 ft-lb to 100,000 ft-lb [46].

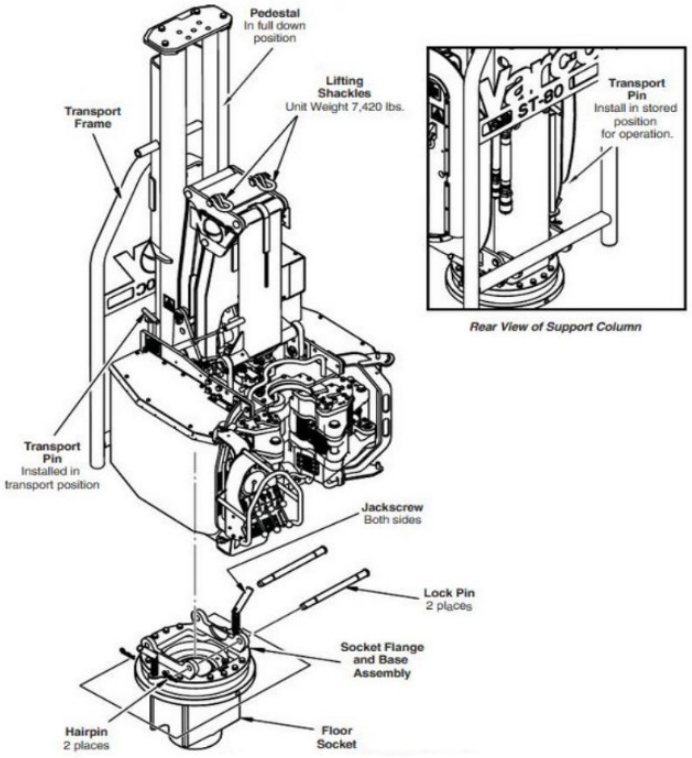

Figure 42: Pairing the ST-80 Iron Roughneck with its socket ([47].p.42).

The Iron Roughneck is located on the other half of the platform and can easily extend onto the bushings centre. The frame work of the substructure can easily house the floor socket in the same way as the master bushing, however its specific design is not included in this work. Another benefit of the I-Beam design is that similar to rails, it can guide a fitted trolley system on which a cable winch is mounted, in order to move and enable fine adjustments on the annular BOP, Rotating Control Device (RCD) or bell nipple, while installing.

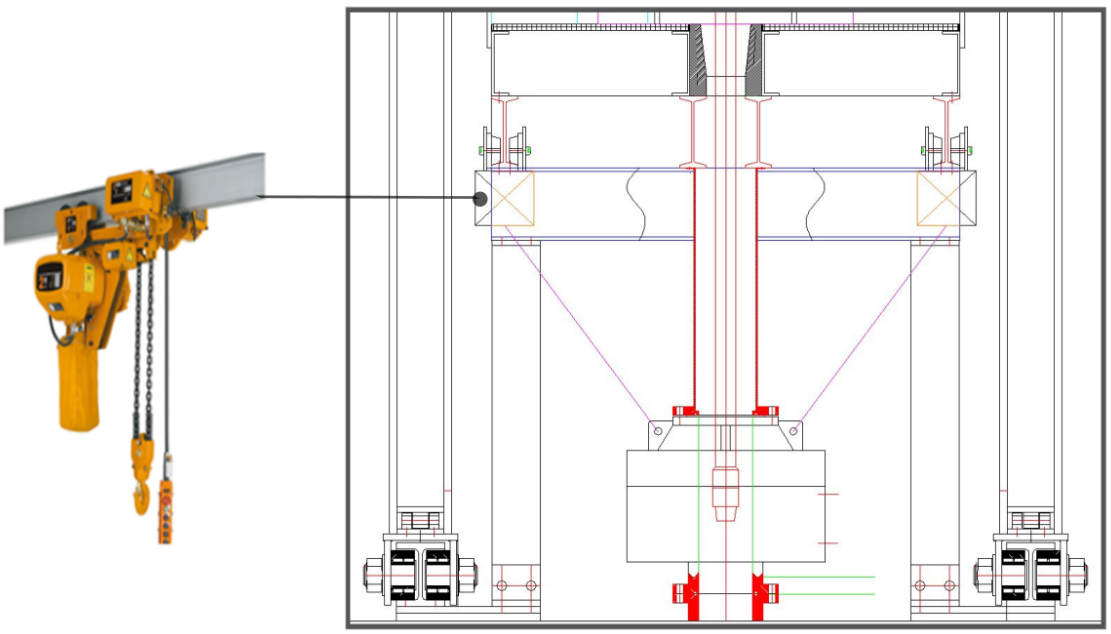

Figure 43: The cutaway front view of the partially visible substructure supporting the master bushing and the trolley system [48].

The idea is to lift these equipments past the pipe handler by means of the forklifts extendable arm and perform a transition mount onto the trolley system.

2.5.1.5 Mast Design

The loads discussed in this chapter, are predominantly static loads or low frequency pulsating loads at most, implemented by the top drives torque depicted in figure 44. Dynamic high frequency pulsating loads subjected to the mast during drilling, for instance vibrations or resonant frequencies related to the interaction of RPM and the drill strings current position (centre of mass and moment of inertia), are certainly a field which needs to be covered in more detail, open for FE fatigue strength analysis.

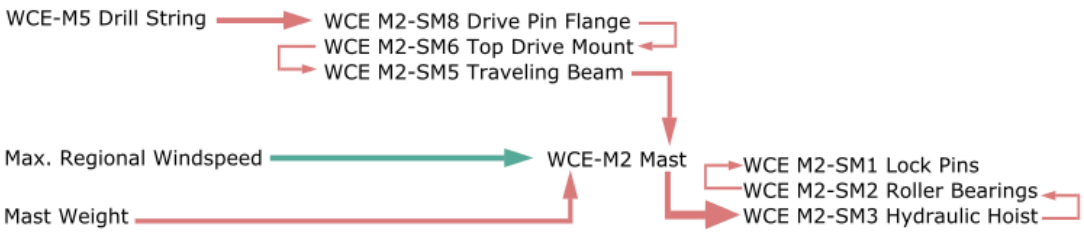

Figure 44: Load sources and its progressions through the components within the mast. Critical areas within the load path are the travelling beam, roller bearings and lock pins.

The mast is subjected to loads, which are not typical for a regular mast as encountered on drilling rigs, as the truss is predominantly free from compression loads, normally imposed by the drill string, when ran in or pulled out. This load is diverted from a central beam, on which the top drive is mounted, onto two powerful hoisting cylinders, located on the sides within the mast.

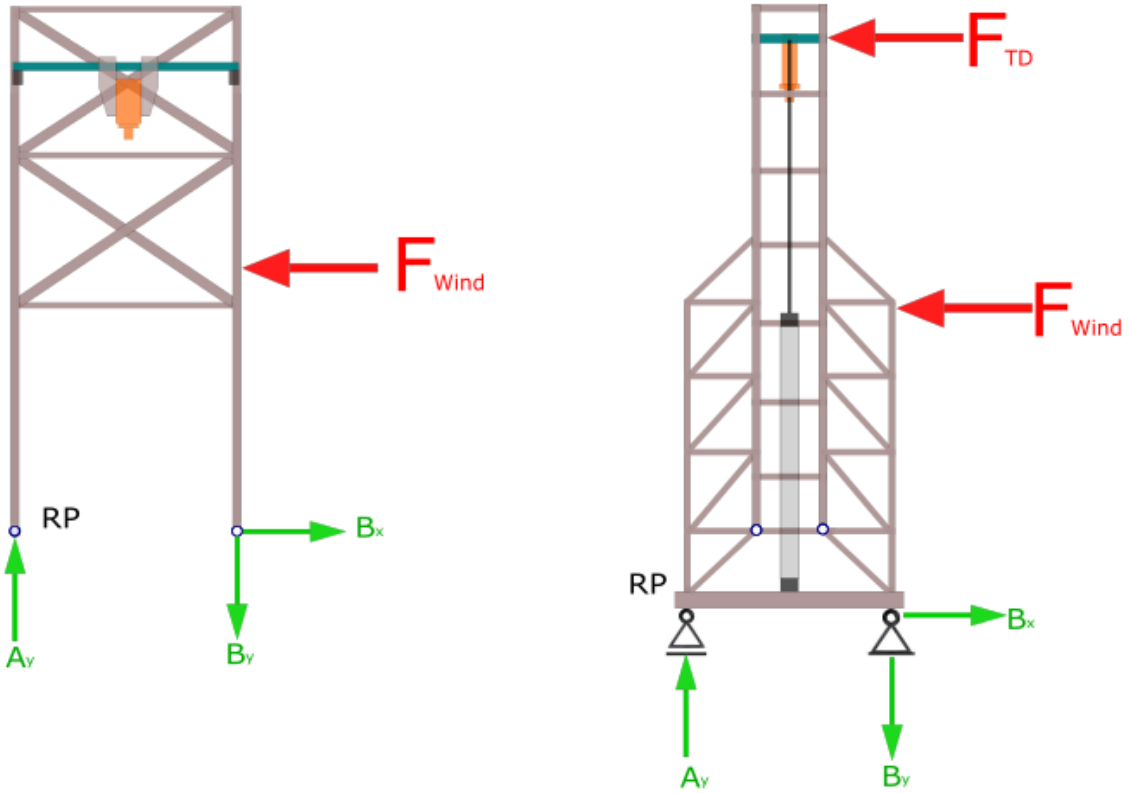

Figure 45: Truss simplified layout with active forces and reaction forces. The guided central travelling beam (dark green) is moved by two hoisting cylinders. The static calculations have been performed in this configuration, as the structure is subjected to the highest forces.

This configuration rather resembles the dynamic loads of a portal crane or a gantry Numerical Control (NC) milling machine, with a vertical travelling beam. The wind force is a function of regional wind speeds [49], and the presented open area it captures [50]. Table 8 shows the classification of force magnitude of regional wind load.

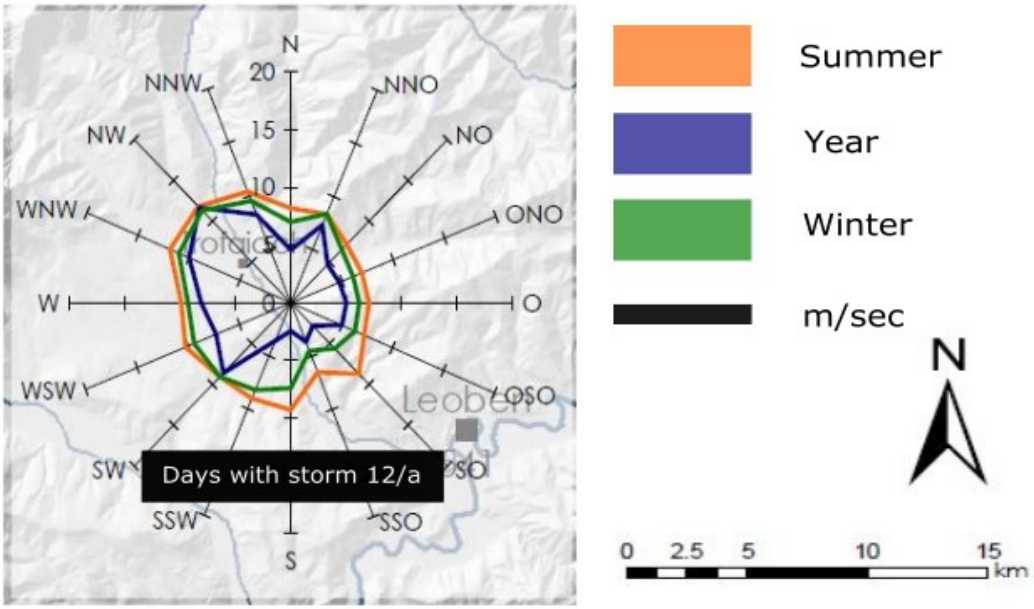

Figure 46: Maximum wind speeds for Leoben and Trofaiach from the Styrian Climate Atlas. The highest wind speeds were recorded with 10 m/sec in a north west to south east orientation ([49] p. 50).

As both sides of the structure are symmetric, the area of focus extends centrally, with 5.8 m in height for the left perspective in figure 45 and 5.2 m for the right perspective. It can clearly be seen, that the method of construction in the side view is more pronounced with rods, as it is subjected to more forces.

Table 8: Wind load in 10 m height [50].

Wind Load	
Mean Wind Speed [m/s]	10.9
Velocity Pressure [kN/m²]	0.07
Velocity Pressure [kg/m²]	7.14

The power balance which result the reaction forces for dimensioning the critical elements of the structure are presented in table 9.

Table 9: Mast power balance calculation. The force originating from the top drives maximum torque rates 3630 N.

Layout	Power Balance [N]			
Front View	F_{wind} = 2,590	A_{yl} = 7,240	B_{xl} = 2,590	A_{xl} = 7,240
Side View	F_{wind} = 3,850	A_{y} = 21,967	B_{x} = 7,480	A_{x} = 21,967

The most critically stressed segments within the truss are the rods number 38 in the front view and rod number 3 in the side view, rod number 38 being greater, viewable in Appendix A. The static constraint in trusses has been performed according to the Polplan, which shows the degree of static stability *f*, verified with the value of zero, shown in equation 23 [51].

$$f = 2 \times k - (r + s) \tag{23}$$

Whereas,

k…Number of nodes (-)

r…Bearing value for floating and solid bearings (-)

s…Number of rods (-)

By means of equation 24, the allowable stress $б_a$ can be compared, if the selected semi-furnished profile is appropriate for application [45].

$$б = \frac{F}{A} \leq б_a \tag{24}$$

Whereas,

б…Rod stress (N/mm²)

F…Rod force (N)

A…Truss profile cross section (mm²)

The mast truss profiles are listed in table 10, with allowable strength values for pulsating tensile and compression loads of 205 N/mm², for material S355 JRH [45].

Table 10: Summary of the masts semi-finished beam profiles ([40], pp. 43-117).

Profile		Dimensions [mm] (hxbxt)	Axial [cm³]	Section	Modulus	Material	Standard
1	I-Steel	432 x 307 x 21	4820			S235JR	EN10025
2	Hollow	400 x 400 x 6.3	1270			S355JRH	EN10025
3	Hollow	200 x 200 x 6.3	301			S355JRH	EN10025
4	Flat	4,600 x 40				S235JR	EN10025

As expected, the allowable stresses exceed the apparent loads more than 10 fold with the least profile thicknesses. This might leave the impression of an overdesigned structure, however this is not true, as the fatigue strength due cyclic loadings are left out in this application and a subject for more detailed analysis as mentioned before. The truss configuration resulted from the needs of its functionary requirements and serves as a blueprint.

2.5.1.6 Travelling Beam

The travelling beam is dimensioned similarly to the master bushing supporting beams according to equation 22. The beam is mounted directly onto the hoisting cylinder fork stubs and secured into place by means of a lock pin on each side, which can be seen in figure 47. The only direct connection to the truss, are mounted rollers, guided within an I-Beam, which is the similar principal of the skid mount in the next sub chapter. For this reason the lock pins are assumed to be free of the winds influence.

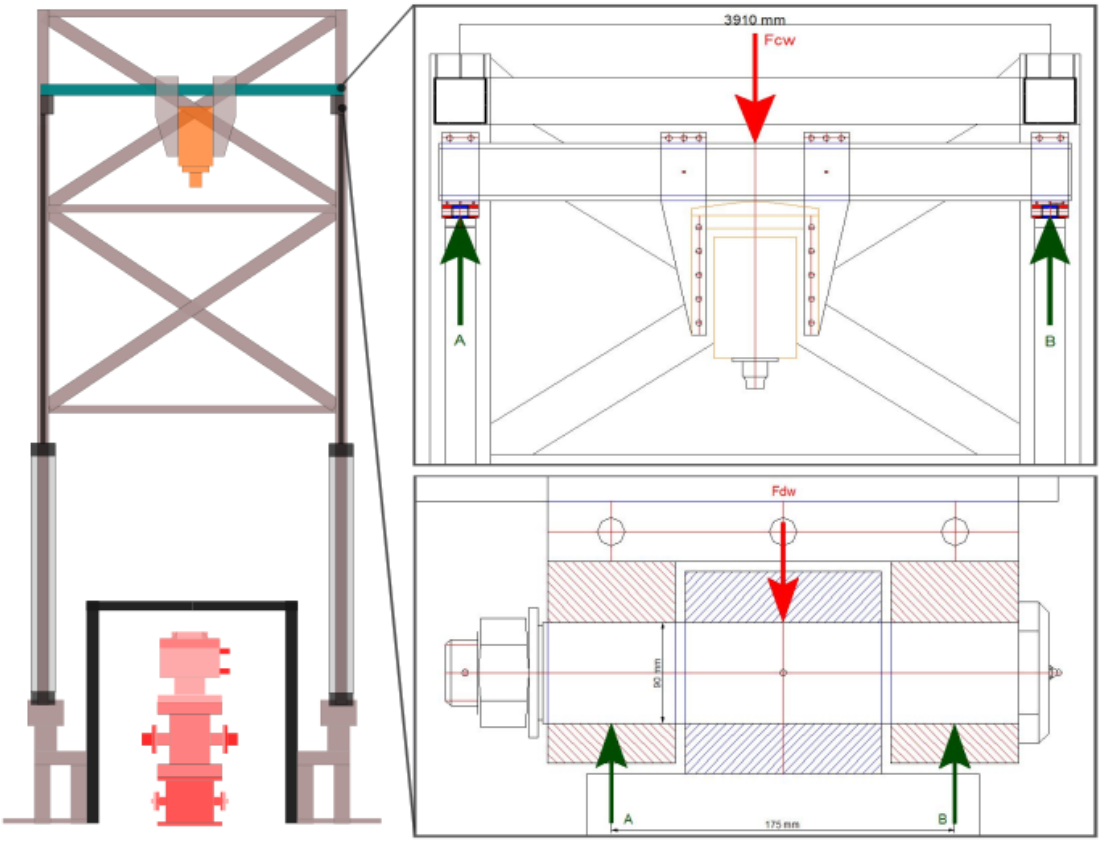

Figure 47: The top drive is remounted onto an adapter, which is primarily a bolted construction of steel plates clamping the original frame with steel spacers in between in order to lock its position. The force F_{cw} and F_{dw} resemble refracted loads of the previously discussed drill string. The bottom cutaway drawing shows the shear pin connection between travelling beam and hoisting cylinder dimensioned with a diameter of 90 mm for the top and bottom of the hoisting cylinder.

The lock pins have been designed in the same manner as shown in equation 25, which could withstand triple the strings weight using tempered alloy steel, which is 42CrMo4 in this case.

2.5.1.7 Skid Mount

Depending on which test is intended to be run, the mast can be moved from either the well stack to the pressure cell or vice versa. The mast is part of a movable platform, guided on rails, located at the sides and is part of the substructure. The movement is

facilitated by means of roller bearings, which can be obtained as a semi-furnished ready to mount unit. In this chapter, the previously discussed loads still apply, but with the addition of the masts weight of 11.9 t, which needs to be included at this point, as the referred elements reside at the lower most area of the structure.

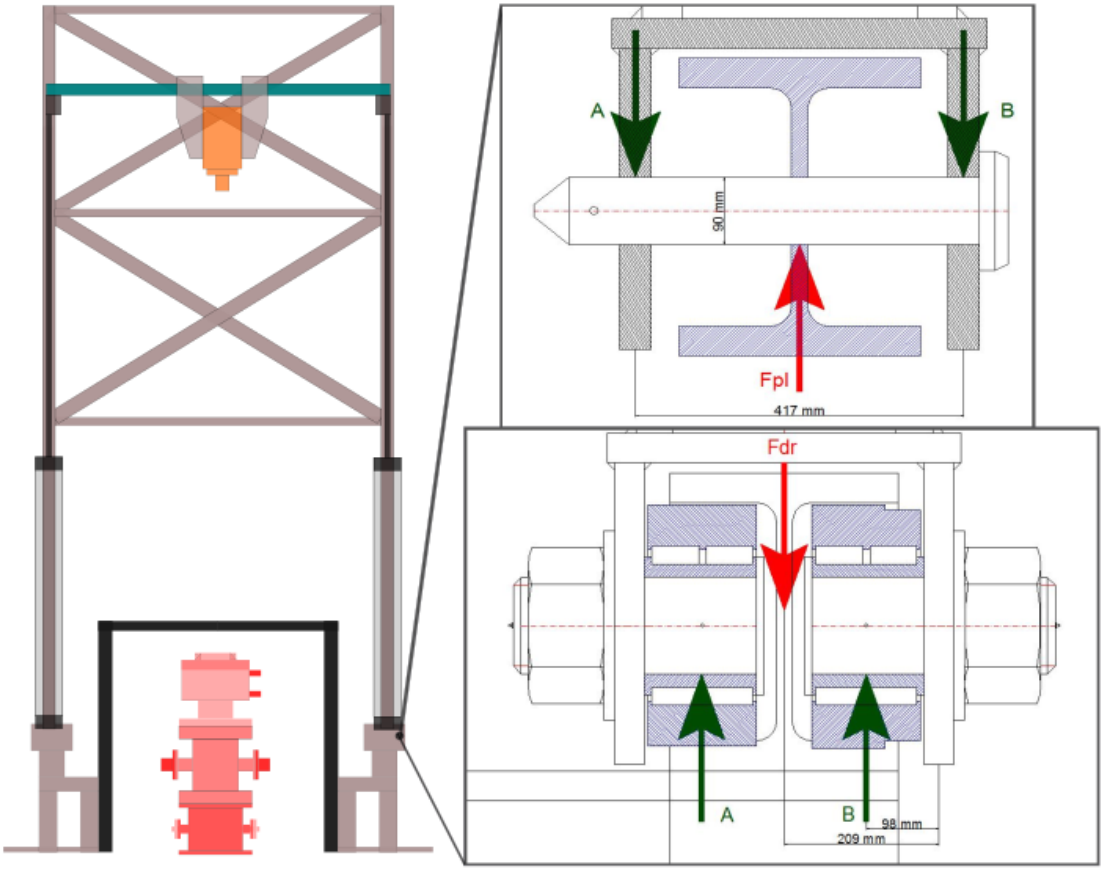

Figure 48: The mast is fixated by 4 lock pins on each side of the structure with 90 mm in diameter shown at the upper cutaway draft. Five roller bearing pairs on each side of the mast as depicted in the lower cutaway drawing are guided by an I-beam. The bearings static load rating C_{rw} is 1,600 daN and dynamic load rating C_{0rw} is 1,020 daN ([52] p45.).

The dimensioning results from the assumption of pivoting the whole structure around the reference point depicted earlier in figure 45. As the roller bearings are predominantly static in nature, dynamic lifespan calculations would have been a redundant effort. However the lock pins have been evaluated on bending, shearing and contact pressure, as the pin is not supported properly, being prone the approach a line load manner. Evaluation on bending $б_b$ in N/mm², shear $\mathcal{T}$ in N/mm² as well as contact pressure P in N/mm² has been conducted according to equations 25, 26 and 27 [45].

$$б_b = \frac{F_{pl}\,32}{d^3\pi} \leq 0{,}2 \times R_m \tag{25}$$

$$\mathcal{T} = \frac{2F_{pl}}{\pi d^2} \leq 0{,}15 \times R_m \tag{26}$$

$$P = \frac{F_{pl}}{2ab} \leq 0{,}15 \times R_m \tag{27}$$

Whereas,

F_{pl}…Refracted force (N)

d…Pin cross section (mm)

a…Height of contact area (mm)

b…Width of contact area (mm)

R_m…Tensile strength of material (N/mm²)

The highest stresses result from bending with distributed loads onto a total of 8 pins, suggesting tempered alloy steel made from 42CrMo4. The load comparisons are listed in Appendix A 2.

2.5.1.8 Hoisting Cylinders

The selected hoisting cylinders are two double acting hydraulic cylinders located in the masts flanks. As viewed earlier the former configuration of installation, was one double acting cylinder, with a stroke length of 2m, extending downwards. This is due to the main purpose of producing the highest amount of thrust required for WOB, for the former tests. However, the requirements for this application have become more diverse, as it is necessary to pull out a considerable amount of string weight on one hand and on the other, provide sufficient WOB while drilling, while WOB has not yet been established by the DC in the early drilling stage. For this reason the main force is prioritized in an upward motion, hence two double acting cylinders installed upright.

Another problem encountered in the past, is the lack of an automatic feed, as the string was moved with manual controls. Looking at the big picture, it becomes obvious that the requirements are similar to a numerical control machine-tool, even closely similar to a gantry mill. These machining centres of today are highly sophisticated, regarding their working axis and automatic feed. However for this particular case, 4 main functions, and therefore at least 4 Programmable Logic Controller (PLC) adjustable control interfaces need to be established, for rotating, downward feed, upward feed and circulation, similar to a lathe while performing ejector deep drilling on round metals.

The only difference is that the product of interest in this case is making hole with highest possible ROP and therefore the cutting velocity is not constant, while the interest of a machine-tool is to fulfil the tolerance of the work piece in an efficient manner with constant cutting velocity. An analogy can be tied regarding the equation 28, showing the feed force in N for constant feed during drilling [53].

$$F_f = zbh^{1-m_f} \tag{28}$$

Whereas,

z…Amount of cutters (-)

b…Width of cut (m)

h…Thickness of cut (m)

m_f…Kienzle constant (-)

$k_{f1.1}$…Theoretical specific feed force material dependant (N/m²)

The mentioned process variable is one of many, which need to be integrated into a PLC control, which actuate the control valves for cylinder movement depicted in figure 49.

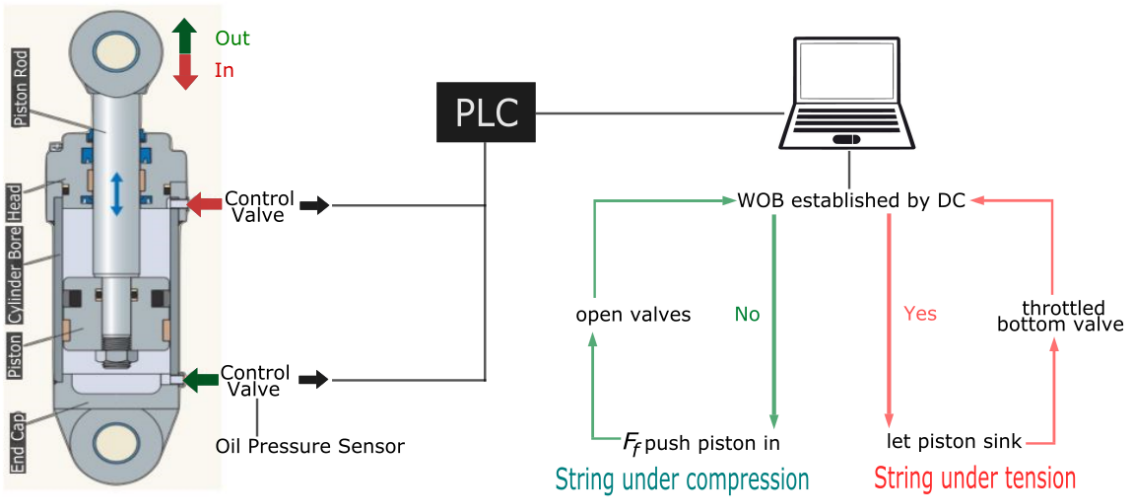

Figure 49: Logic circuit actuation for the hoisting cylinder. The left circuit (green) is repeated until the condition is fulfilled switching to the right circuit (red).

In the early drilling stage, the ROP is usually rather low, due to the lack of string weight. This can be rectified by using the down stroke of the cylinder to increase ROP, which would not be possible with a conventional drawworks. This process is repeated while adding pipe until the required WOB is established by the DC.

A measurement method on hook load, is described by M. Ramsauer, where the oil pressure value within the lower chamber can be tapped and converted [54]. Feeding the sensor values into the PLC, can enable to switch into an operating mode as encountered in genuine drilling, where the string is under tension to its neutral point.

Table 11: Summery of hydraulic cylinder design parameters [55].

Design Parameters for one cylinder			
Piston diameter [mm]	200.0	**Thrust force [N]**	314,159.0
Rod diameter [mm]	160.0	**Pull force [N]**	113,097.0
Stroke [mm]	5,000.0	**Area ratio [-]**	1:2.8
System pressure [bar]	100.0	**Availability [%]**	100
Piston area [cm²]	314.2	**Extending velocity [mm/sec]**	10.6
Ring area [cm²]	113.0	**Retracting velocity [mm/sec]**	29.5
Piston volume [dm³]	157.1	**Extending time [sec]**	471.2
Ring volume [dm³]	56.5	**Retracting time [sec]**	169.7
Rod volume [dm³]	100.5	**Pump capacity [l/min]**	20

The required hydraulic cylinder design and its working parameters are listed in table 11. In the early days, the feed rate of the working axis, were managed hydraulically with high precision. Nowadays the feed rates are managed electrically via spindles, for maintaining constant cutting forces. For this particular case, the realization will be based on a hydraulic platform, as the hydraulic power units are already in place.

Chapter 3 Testing Preparation

One essential step in conducting drilling tests, is to create the artificial lithology for the bit to drill upon. This is enabled through various cement compositions and subsequently countless combinations in ratios of mixture constituents. An important aspect is to prevent cement from entering the discharge ports in the pup joint. Therefore a lead foam cement is placed directly onto the permeable media and allow this segment to gain premature strength to act as a non protruding barrier.

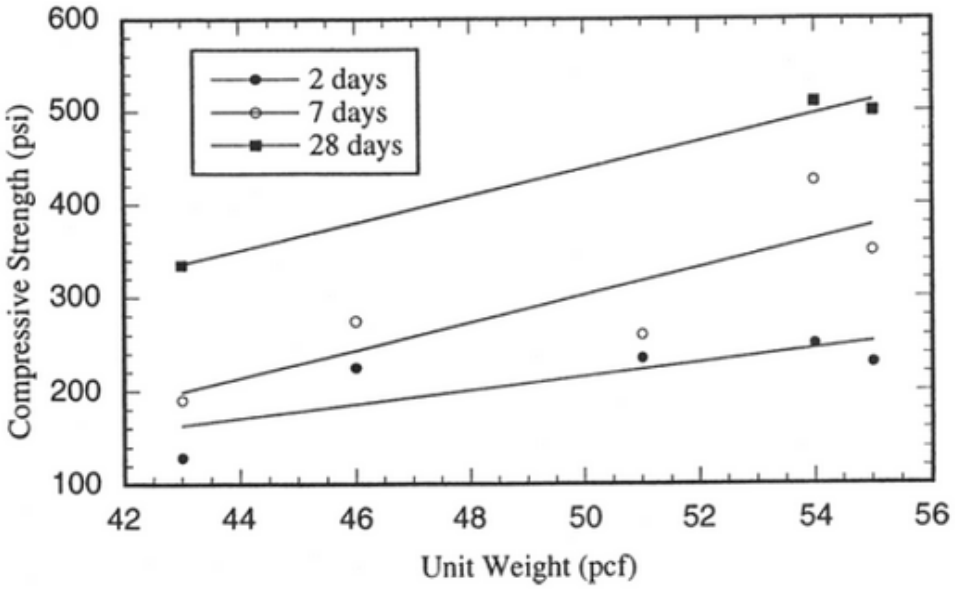

Figure 50: Various compressive strengths of foam grout as a function of curing time for different densities ([56] p.2).

This will rule out the danger of intrusion into the permeable media, which might plug the influx ports. The foam cement hast to be dense enough to displace the water, initially residing within the 9 5/8 in casing. Afterwards, the actual slurry composition of interest for drilling can be deployed using a method of annular space grouting as shown in figure 51. The difference is that the tremie pipe is substituted by a flexible conduit, retracted simultaneously as the cement height moves up during filling while inserted in the 9 5/8 in casing

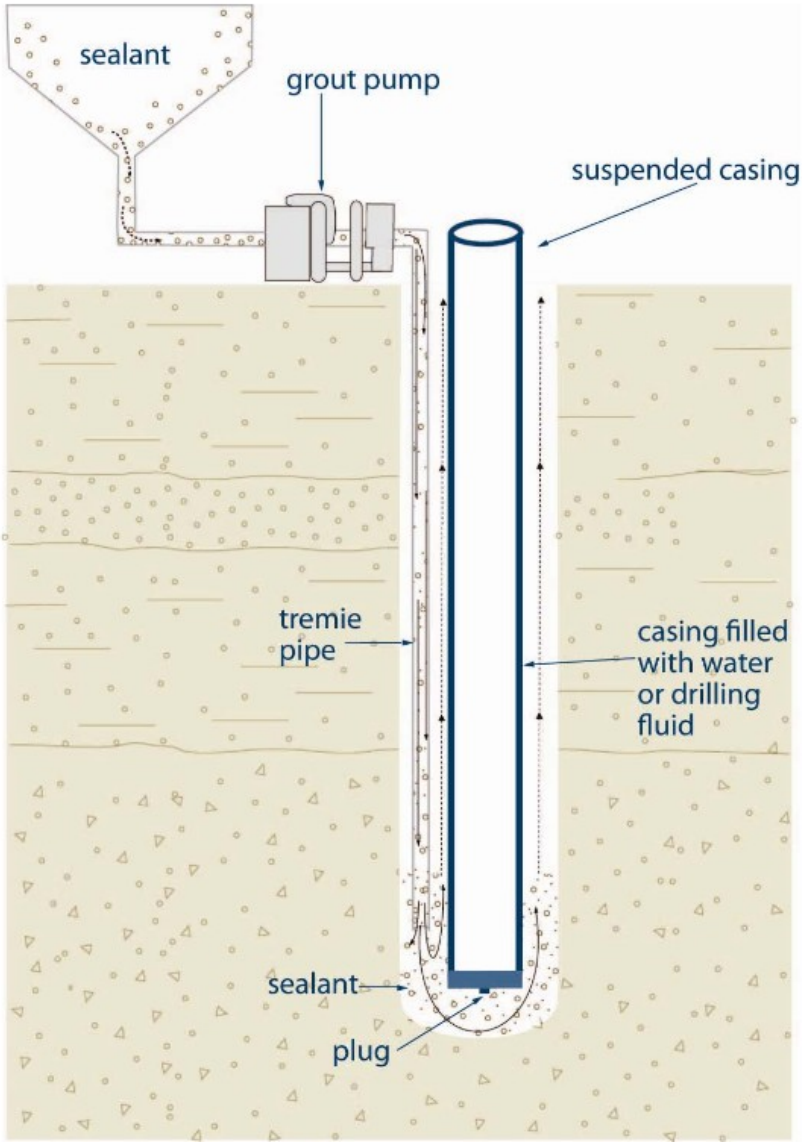

Figure 51: Cementing annular space with a tremie pipe ([57] p. 41).

The annular BOP is therefore mounted off to gain access to the wellhead housing, in which the grouting tube is hung into the depth of the substrate. After deploying a defined volume of foam grout, the pump is stopped, and the water filled tremie pipe is slightly lifted, allowing the grout to cure enough for further cementing. Afterwards the actual test cement can be deployed in the same manner as shown in figure 52.

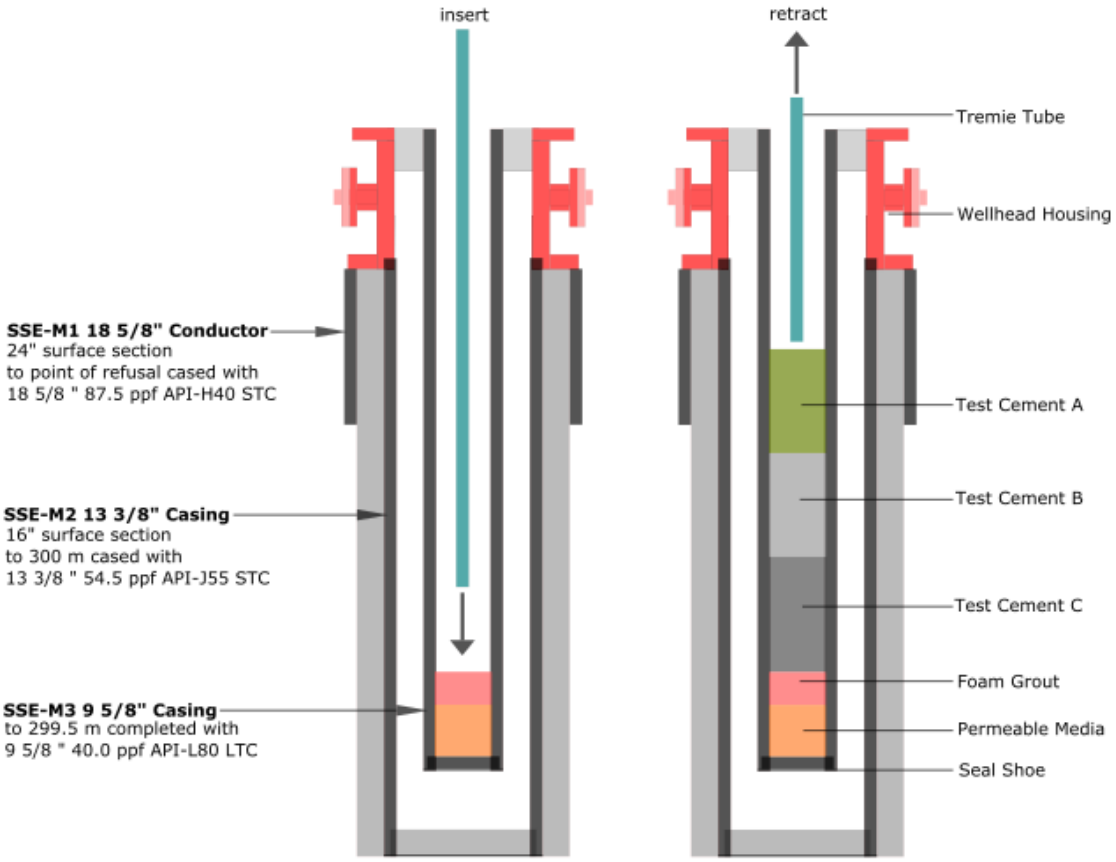

Figure 52: Cementing onto prematurely cured grout. The tremie tube is inserted on the left. Test cement is pumped by simultaneously retracting the tremie pipe, placing the test cement compound into the 9 5/8 in casing.

At this state the measures to accelerate the curing process is facilitated by the heating system [58]. This is achieved by circulating the completion fluid in which the casing is immersed. While curing the filling, a laboratory set up with identical cement samples can be cured under similar conditions in a smaller scale, to track the progress of the established compressive strength build up, by performing compressive strength tests with a press as shown in figure 53.The selected test cements are high strength marine grouts, designed to cure immersed in water. The technical data is presented in table 12, on which the calculated ROP for the drilling tests are based on [59], [60], [61].

Table 12: Underwater foam grout compressive strengths in a cured state, with similar ranges of sedimentary rock strengths ([62], p. 52).

Test Cement	Cured Density [kg/m³]	Compressive Strength [psi]
A Shale	1,860	8,500
B Sandstone	2,100	13,053
C Limestone	2,250	15,229

Figure 53: A cured cement specimen, tested on compressive strength [63].

A proposed set up for the laboratory includes several open curing chambers partially immersed in a water bath, to mimic the curing on a smaller scale.

3.1.1 Heating System

The heating system essentially consists of an industrial electric heater, a service pump, an inlet pump and steam pressure control valves.

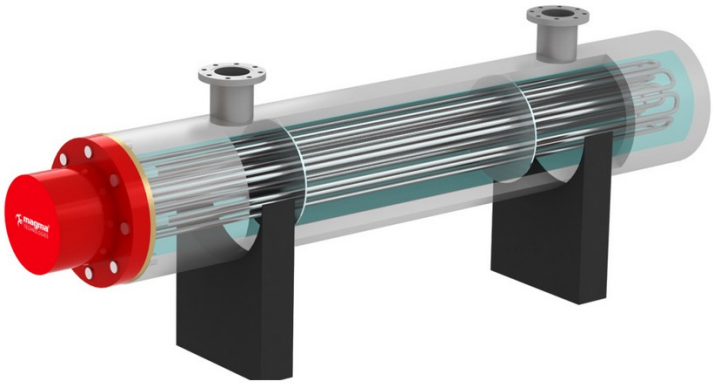

Figure 54: One heating pod of an electric industrial heater. Several pods can be combined to form a heating cluster [64].

During facility maintenance, the pumps can either be synchronized, or the exiting pump from the wellhead housing can be configured as fluid level actuated, only pumping when a certain fluid level has been reached when heaters are off. The discharge pump with a flow rate of 76 l/h has a discharge pressure of 50 bar for fluid phase applications [65].

The facility design is based on a saturated steam pressure of 90 bar according to the steam tables, capable of providing 2,558 kJ/kg of steam mass flow at 303°C.

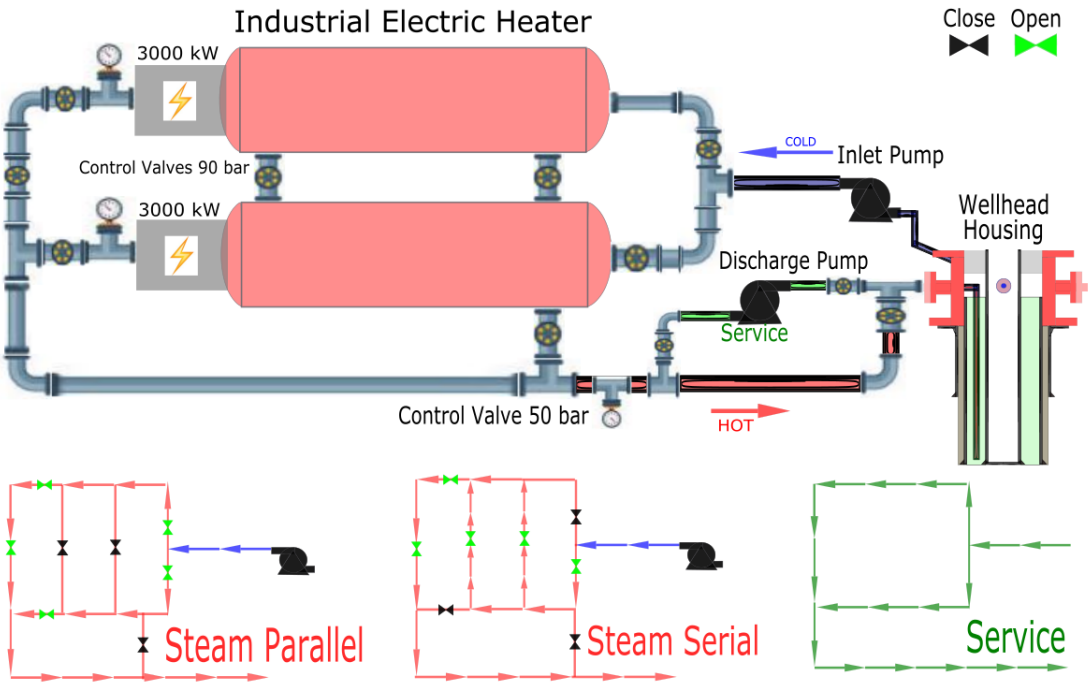

Figure 55: The layout depicts two pods, each with 2,500 l capacity. Depending on steam amount and pressure output, the heater can be operated in serial or parallel mode. Each pod is capable of generating 1,3 kg of steam per second. During the initial phase, the heater is operated parallel in tandem maintaining 90 bar shell pressure to guarantee a continuous supply of steam at 50 bar. When the well is heated at the desired temperature, the heater can be operated in serial mode in order to heat in increments of steam to maintain the well temperature. The service mode is for completion fluid and facility maintenance.

By solving equation 29 for specific heat Q in J and equation 30 for mixed temperature T_m in °C, one can estimate the energy load needed to heat up the stored water within the lower pod and the energy needed to overcome the temperature difference when cold water chosen with 76 l, is immediately mixed with the entire hot shell fluid.

$$Q = c_w m_w \Delta T \tag{29}$$

$$c_w m_1 (T_1 - T_m) = c_w m_2 (T_m - T_2) \tag{30}$$

Whereas,

c_w…Specific heat (J/kg K)

m_1…Mass of hot water (kg)

m_2…Mass of cold water (kg)

T_1…Temperature of hot water (°K)

T_2…Temperature of cold water (°K)

$T\Delta$…Differential temperature (°K)

T_m…Temperature of mixture (°K)

Even though this is not the case, this would yield a mixing temperature of 302 °C and it would take 7.2 sec to reheat the new temperature volume up to 303°C. Knowing this, one can assume a constant supply of steam not overloading the heating system with cold water on one hand and deploying enough heat per volume of mass flow on the other hand, to achieve a positive energy balance, in order to be certain that the well is heated up. This cannot be taken for granted with a conventional fluid phase heater, as the delivery of energy with mass flow, is restricted due to the conduit limitations of the system and energy deployment in the fluid phase. It is assumed that the 13 3/8 in casings outer surface is the only source of heat loss and the cement and casings are heated with direct fluid contact, depicted in the heating procedure of figure 56.

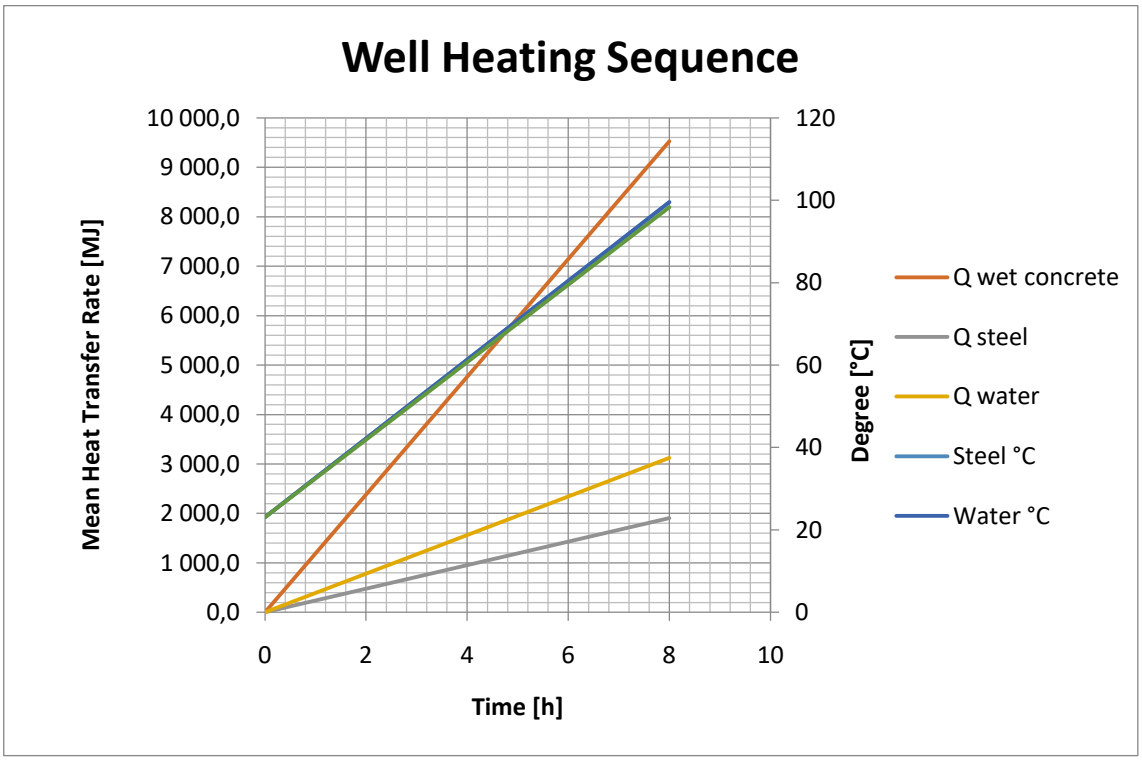

Figure 56: The individual energy consumptions of each element from energy mass flow over time have their origin at the primary axis, showing that concrete consumes most of the power input. At the secondary axis the entire system as a whole can be observed individually during heating from an average well temperature of 23°C to 100°C within 8 hours with 1226 kg of saturated steam.

The test cement fill therefore cures within a radial expanded casing due to the induced heat. As the system cools down prior to drilling tests, the retraction of the casing to its original state is prevented by the cured cement, as the thermal expansion of steel is greater than cement. This confirms a present force, frictionally gripping the cement fill.

3.1.2 Wellhead Injectors

The initiation of fluid influxes are preformed in order to test the drill string prototype sensors to automatically shut in the well once a kick is detected. This facility is designed to inject gaseous and fluid influxes into the wellbore.

3.1.2.1 Gas Influx Compressor

The gas influx is produced by compressor, capable of establishing a continuous supply of air under 100 bar and a flow rate of 0.8 m^3/min [66]. Figure 57 shows the intended operational modes of the unit.

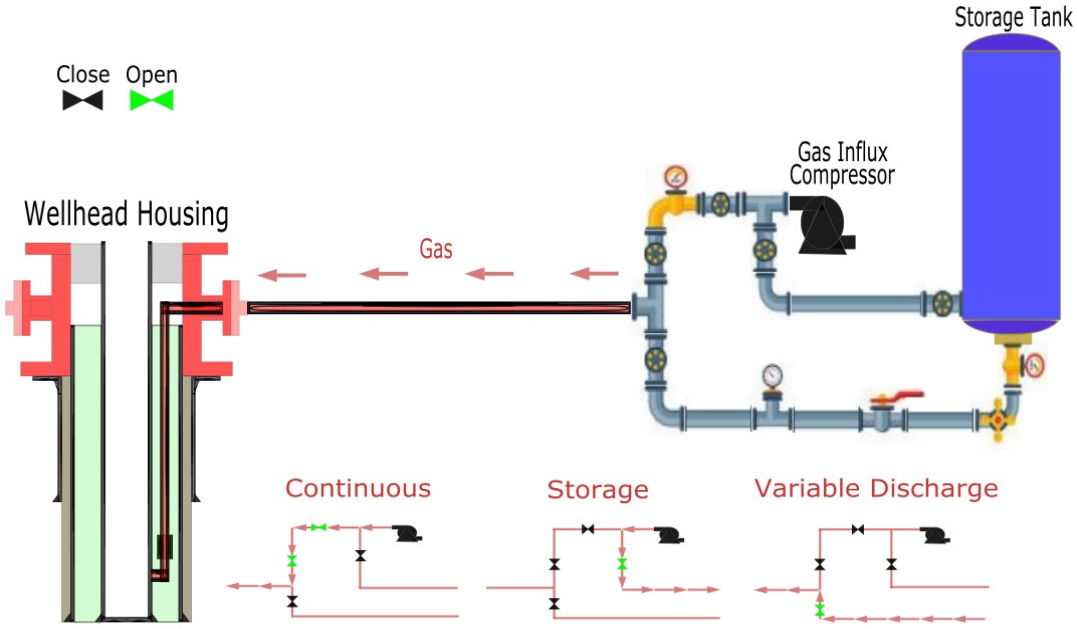

Figure 57: Besides operating continuously for simulating a producing well for managed pressure drilling purposes, a predefined volume of discharge pressure can be injected into the well.

There are many documented ways and degrees of sophistication to calculate the migration speed of a gas kick, due to the fact that gases as well as the drilling fluid vary in compositions. However, the relationships between volume and pressure settings are ideal gases according to Boyle-Mariotte, as they behave as such at high pressures shown in equation 31.

$$P_1 V_1 = P_2 V_2 \tag{31}$$

Whereas,

P_1…initial pressure (Pa)

P_2…final pressure (Pa)

V_1…initial volume (l)

V_2…final volume (l)

The migration speed V_g in ft/sec for a shut in well is estimated by the equation 32.

$$V_g = 12 \times e^{-0.37\rho_{mud}} \tag{32}$$

Whereas,

e…base of nature logarithm (-)

ρ_{mud}…mud weight (ppg)

For WBM of 10ppg being the drilling fluid in this application, the migration speed results in 0.54 ft/sec meaning the influx will arrive in 29 minutes at the surface [67]. Should a gas kick remain undetected, it is assumed for this application, that the influx travels the same speed as the annular velocity when circulating after an influx was initiated. For safety reasons the BOP should be shut in.

3.1.2.2 Liquid Influx Pump

For liquid influxes, an additional pump is installed near the mud tanks as being part of the "Mixing & Recycling" unit, where fresh mud can be injected into the well as shown in figure 58 [68].

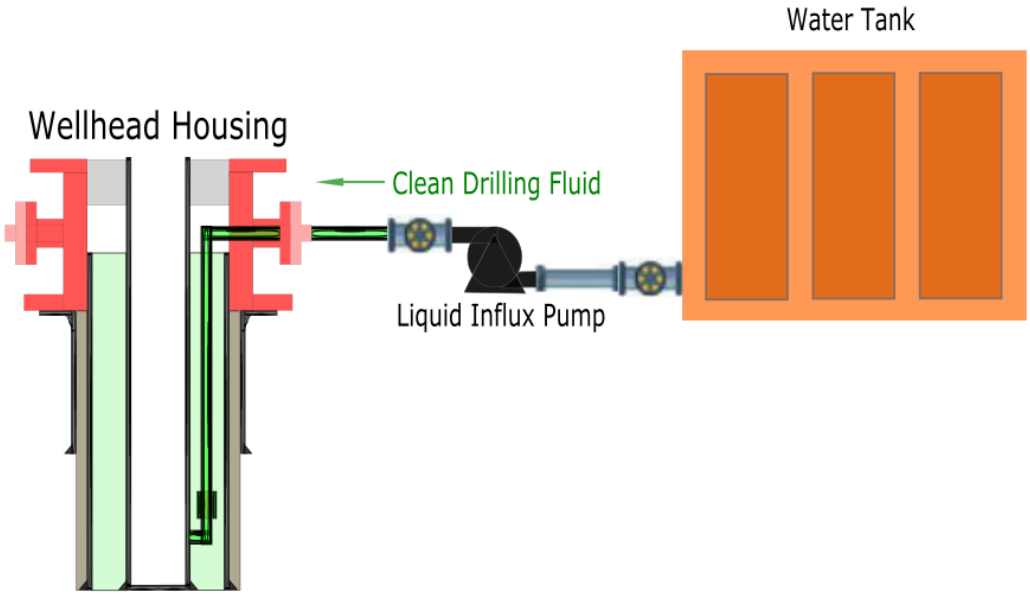

Figure 58: The influx pump is part of the mud circulating system.

An arising concern, due to fluid friction within the long and low diameter influx conduits, was the back pressure. Equation 33 from Bernoulli was applied to validate the conduits use, solved for pump pressure P_{pump} in Pa using the recommendation of the manufacturers guide on pipe friction [69].

$$P_1 + \rho g h_1 + \frac{\rho v_1^2}{2} + P_{pump} = P_2 + \rho g h_2 + \frac{\rho v_2^2}{2} + \rho g h_T + \frac{\lambda l \rho v^2}{2d} + \xi \frac{\rho v^2}{2} \quad (33)$$

Whereas,

P…Static pressure of fluid at the cross section (pa)

ϱ…Density of flowing fluid (kg/m^3)

g…Acceleration due to gravity (m/sec^2)

v…Mean velocity of fluid flow at the cross section (m/sec)

h…Elevation head of the cross section with respect to a datum (m)

d…Cross section (m)

l…Tube length (m)

λ…Tube friction coefficient (-)

ξ…Local loss coefficient (-)

The design of the pump rate is at 100 bar discharge pressure, offering a flow rate of 9.4 l/min [70]. The friction losses at the selected flow rate result in 8 bar including the hydrostatic head, which can be overcome by the pumps discharge pressure, without jeopardizing the tubes integrity on pressure rating.

3.2 Test Drilling Procedure

The systems concept is visualized in figure 59, offering two main testing procedures. The main focus of the depicted system is the extension of the facilities capabilities in drilling over- and underbalanced. As the top drive is limited in its functions of only providing circulation and torque, the widespread interaction between a cat walk and the secondary function of the top drives bail operated elevator for pipe handling cannot be realized in this case.

For this reason, a pipe handler is intended to be installed, handling pipes with 4 m in length to ease the labour of pipe connections [71]. This set up can be observed in water well drilling applications, only that the horizontal pipe rack is located on ground level, heaving pipes onto the rig floor with an extendable arm as depicted in figure 61.

Often used for water wells, are compact mixing and recycling systems. As shown in figure 60, the system shows a mixing station, a shale shaker, de-sander unit and compartmentalized tanks combined into one system. In addition, the unit is stacked over a 10m^3 mud tank with equal foot print. [72].

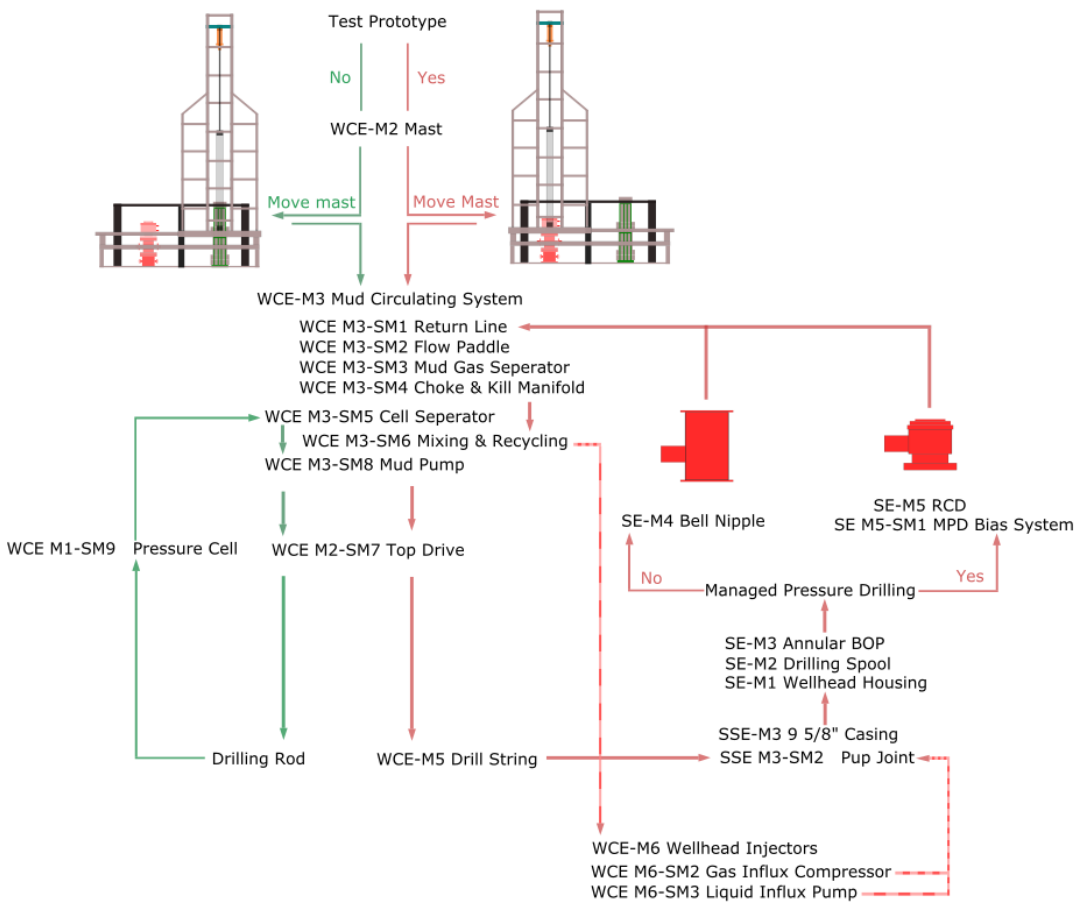

Figure 59: Overview of the system architecture on functionality for the testing facilities extension. The former test functions can be followed on the left (green) involving the pressure cell and the extended capabilities on the right (red trend) for testing the prototype for overbalance and manage pressure drilling.

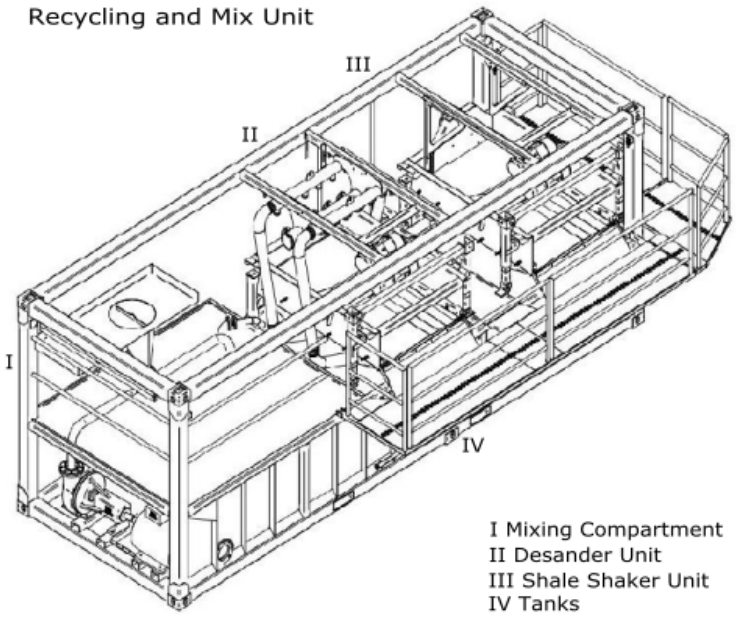

Figure 60: Indicative drawing of the 7m version, RM 1000 mixing and recycling system.

Figure 61: The pipes are clamped and centred onto the top drives axis in order to make the connection, normally performed by the integrated single direction tong of the top drive.

Whenever pipes are meant to be moved vertically, the connection between pipe and top drive needs to be established with the pipe handler, while the make and break up torque for the NC 50 connections are managed by the iron rough neck.

The fact being that this facility is designed to accumulate test performance data, it is obvious that the handling performance of the facility will not be able to compete with drilling rigs built for commercial applications.

Handling 4m pipes will ease the working process, but will increase the overall duration of the operation due to the amount of connections. Recorded time of a Slip to Slip connection within a best practice Weight to Weight connection duration is at 3.4 minutes in literature [73].

Table 13: Duration of the estimated "Slip to Slip " connection during trip out operation.

Operation	Duration
POOH	7.9 min
• Slip in	-
• **Break grip (pipe handler)**	7 sec
• **Break/Spin TD**	5 sec
• **Roughneck**	
-Extend	8 sec
-Height adjustment	2 sec
-Clamp/Break/Spin	12 sec
-Retract	
• **Lay down pipe (pipe handler)**	8 sec
• **Retract hoist**	-
• **TD/pipe-connection**	2.8 min
• Slip out	5 sec
	-

The estimated slip to slip connection for this drilling facility is listed in the table 13, Resulting in 3.6 minutes, slightly above the duration of the referenced best practice value.

3.2.1 Overbalanced Drilling Test

The drilling fluid circulation is managed by the HT-400 mud pump from Halliburton, with the specifications listed in table 14.

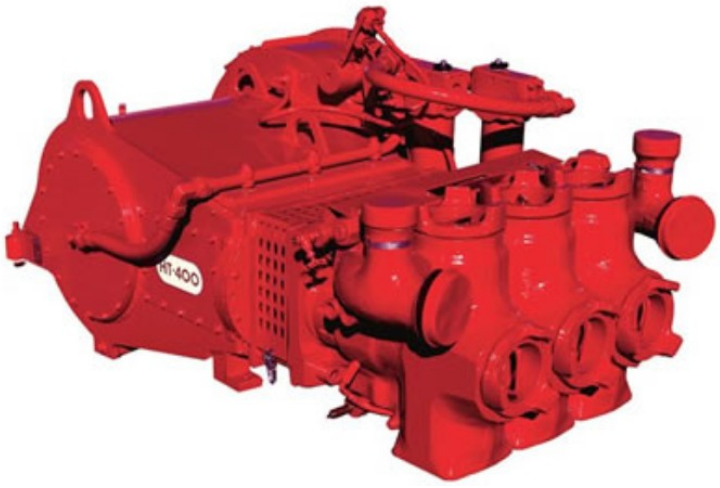

Figure 62: The light weight horizontal triplex pump by Halliburton ([74] p.1).

This unit is present in the TDE Equipment and Manufacturing equipment arsenal and is therefore intended to be a permanent operating asset of the testing facility.

Table 14: Pump specifications, set to perform the drilling tests ([74] p.2).

Pump Specifications	
Plunger Diameter	6 in
Maximum Pressure	3,000 psi
Maximum Rate @ 75 Crankshaft RPM	221 gpm
Maximum HP Input	275 hp

3.2.1.1 Hydraulics

The system pressure loss caused by WBM with 10 ppg is displayed in figure 63. Its design is listed Appendix B1. The ECD is calculated with the Bingham plastic and a power-law fluid model. The settings are adjusted to ensure best hole cleaning conditions, by aiming towards a pressure drop of 65 % from the total pump pressure across the bit. Hole cleaning efficiency across the annulus are shown in figure 66 and are calculated using the Moore correlation, to verify high efficiency in hole cleaning.

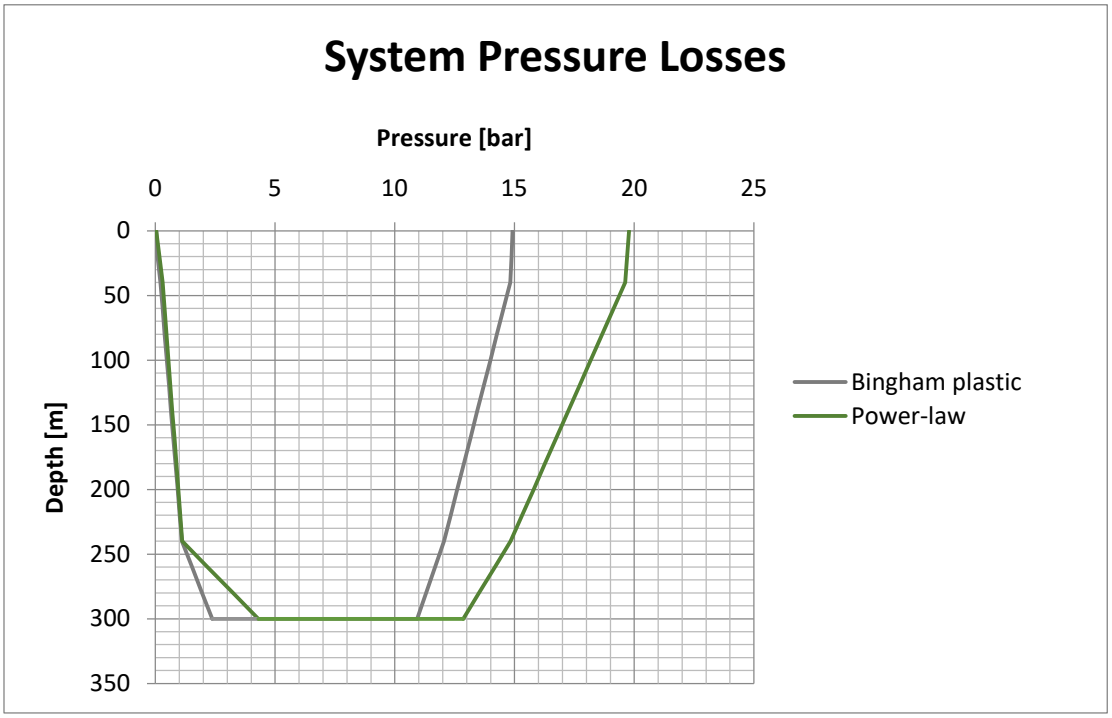

Figure 63: System pressure loss according to the Bingham plastic and power-law, for optimal jet impact force across the bit.

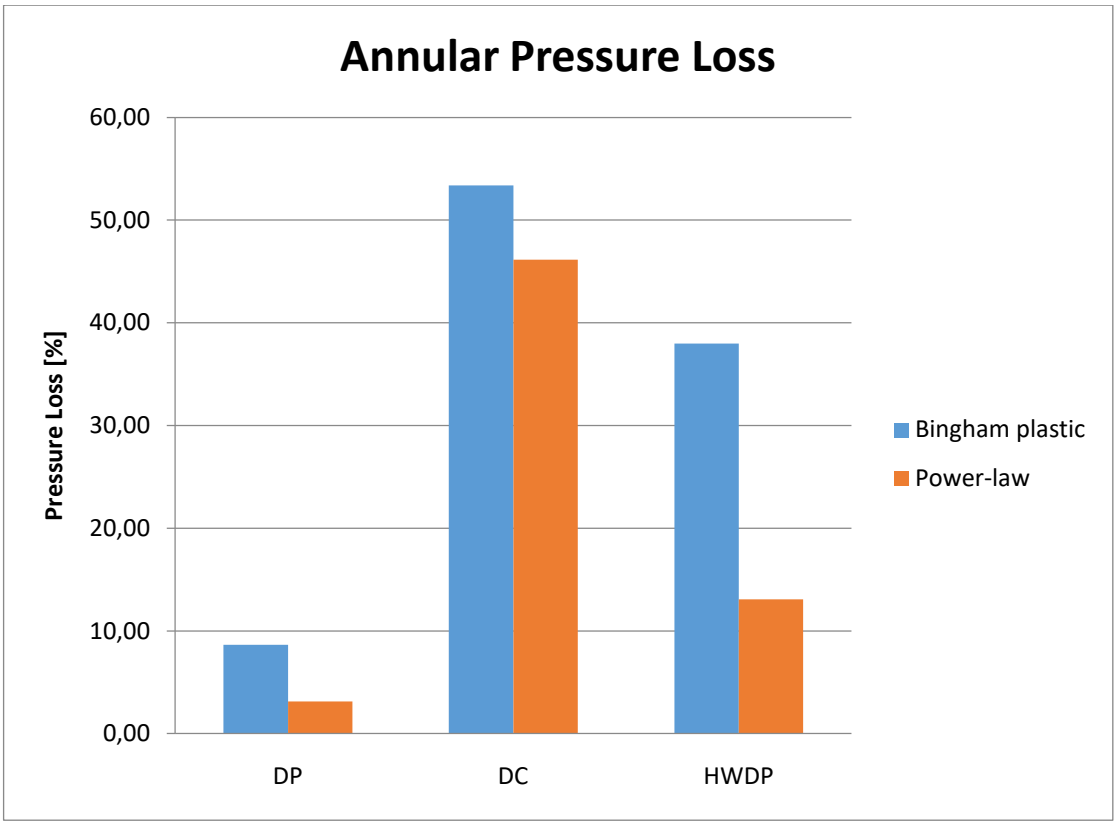

Figure 64: The pressure loss distribution across the annulus, showing a large portion at the drill collar section for both fluid models.

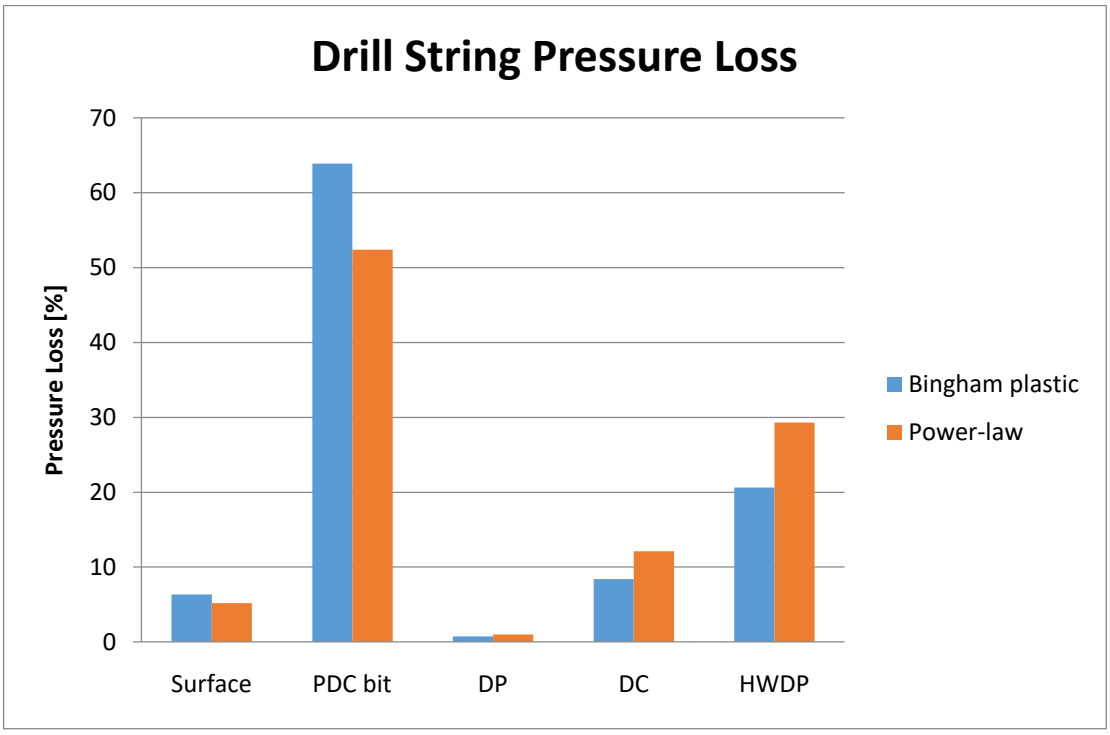

Figure 65: Pressure drop across the bit resulting in 64% of the total pump pressure, leaving 1080 psi for the system for the Bingham fluid model. For the power-law model, the pressure drop across the bit is 52 %, leaving 1440 psi for the system.

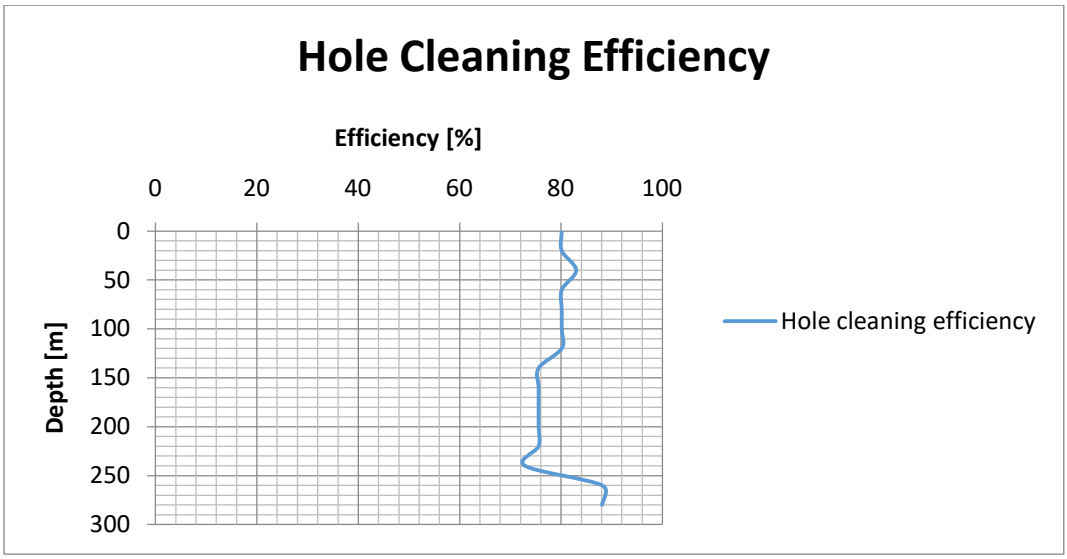

Figure 66: The cuttings transport performed by the Moore correlation.

After reaching Total Depth (TD), the permeable membrane is exposed and the tripping operation can begin. In this test, 6 single stands were pulled and laid down before influx initiation.

3.2.1.2 Operations Monitoring

Bearing in mind, that the 9 5/8 in casing hast stretched to its lower most contact point, due to the cement fill, the applied WOB needed for the PDC bit is applied onto a self sustaining cured cement column and was evaluated with equation 34 for the ROP in ft/h [75].

$$ROP = \frac{13.33\mu N}{DB\left(\frac{CCS}{EEF_M\, WOB} - \frac{1}{A_B}\right)} \tag{34}$$

Whereas,

μ…Bit specific sliding friction coefficient (-)

N… Rotary speed (rpm)

DB… Bit diameter (in)

CCS…Confined compressive strength (lb)

EFF_M…Mechanical bit efficiency (%)

WOB…Weight on bit (lb)

A_B…Bit area (in^2)

Prior to the sensor response in kick detection, the assumed kick data and calculation is presented in table 15.

Table 15: Depending on how fast the sensors can detect the influx, the injected volume is set at 0.5 m^3 by the gas influx compressor at 40 bar.

Kick Calculation	
Section Depth	967.80 ft
Mud Weigh	10.00 ppg
Gas Gradient	0.59 psi/ft
Kick Hight	69.00 ft
Kick Volume @ Bottom Influx	0.50 m^3

The influx may be initiated either with a connected or disconnected drill pipe. In the second case, a Kelly Cock needs to be mounted.

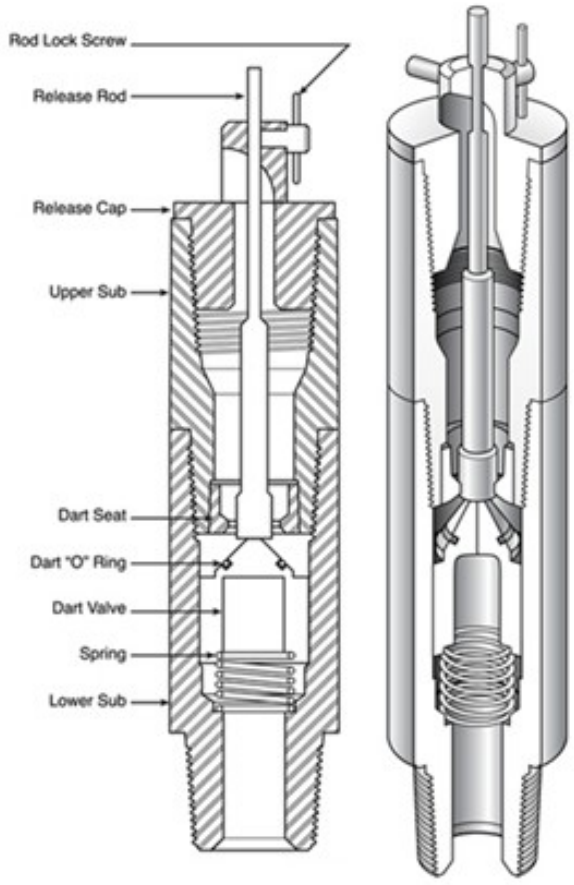

Figure 67: The Kelly Cock should be in short reach, located on the drill floor [76].

Monitoring the casing integrity while conducting various tests, is always advised. Depending on the sensor response in closing the annular BOP, the casing stress triggered by the influx is depicted in figure 69.

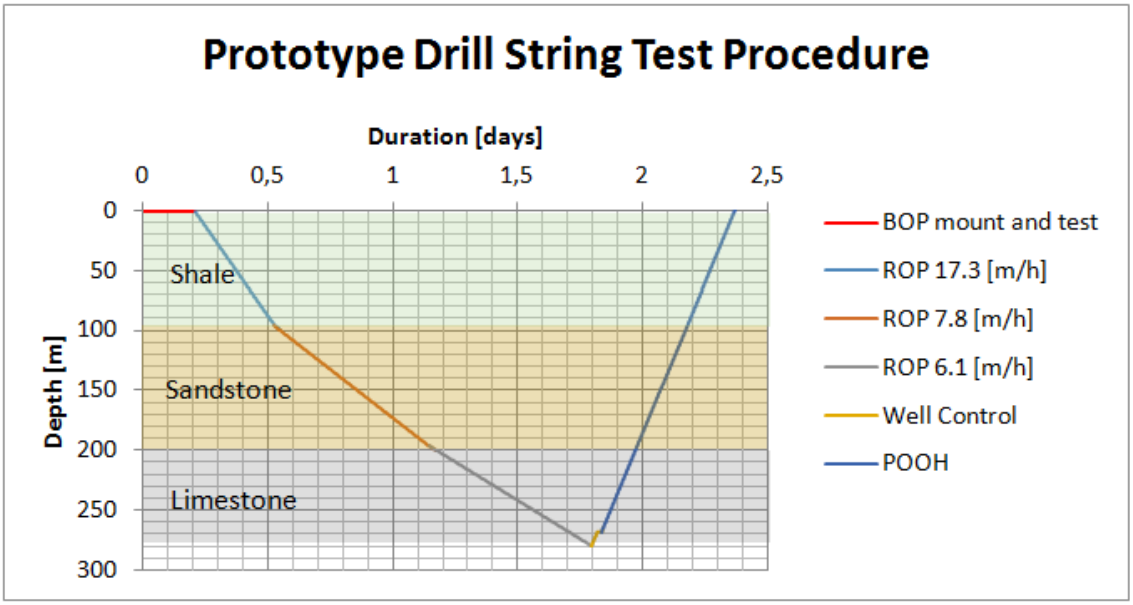

Figure 68: The test starts with mounting and testing the annular BOP. including the assumed curing time of 7 days for the test cements A, B and C under heat, expecting fully developed compressive strengths. The Weight to Weight connection times are assumed with 5 minutes.

Table 16: Critical path of operations for overbalanced drilling with well control. The most time consuming procedure is curing the cement slurry.

Critical Path Operations				
Step [Nr.]	**Depth [m]**	**Operation**	**Duration [h]**	**Cumulative Duration [days]**
1	0	Mix foam cement 342 [l]	0.30	0.1
2	0	Mix test cement A 3,725 [l]	1.30	0.1
3	0	Mix test cement B 3,725 [l]	1.30	0.1
4	0	Mix test cement C 3,725 [l]	1.30	0.2
5	290	RIH tremie pipe (speed 720 m/h); suction pump for displaced well water	0.50	0.2
6	290	Pump slurry/ retrieving tremie pipe (output 150 l/min); activate suction	1.5	0.3
7	0	Activate electric industrial heater; cure cement	168.00	7.3
8	0	Make BHA; Conduct frequent UCS tests; mix drilling fluid; prepare spud	0	7.3
9	0	START 7 7/8" section	0	7.3
10	0	Rig up and test annular BOP	5.00	7.6
11	290	Drill Cement (Gross ROP 6,7 m/h); record drill data; mix kill mud	39.40	9.1
12	290	Pull 6 stands (pull speed 118 m/h); prime compressor tank for 500 l, 40 bar	1.50	9.2
13	290	Initiate Kick volume; verify sensor function; start well control	0.40	9.2
14	290	POOH (pull speed 118 m/h)	15.80	9.8
15	290	END 7 7/8" section	0	9.8

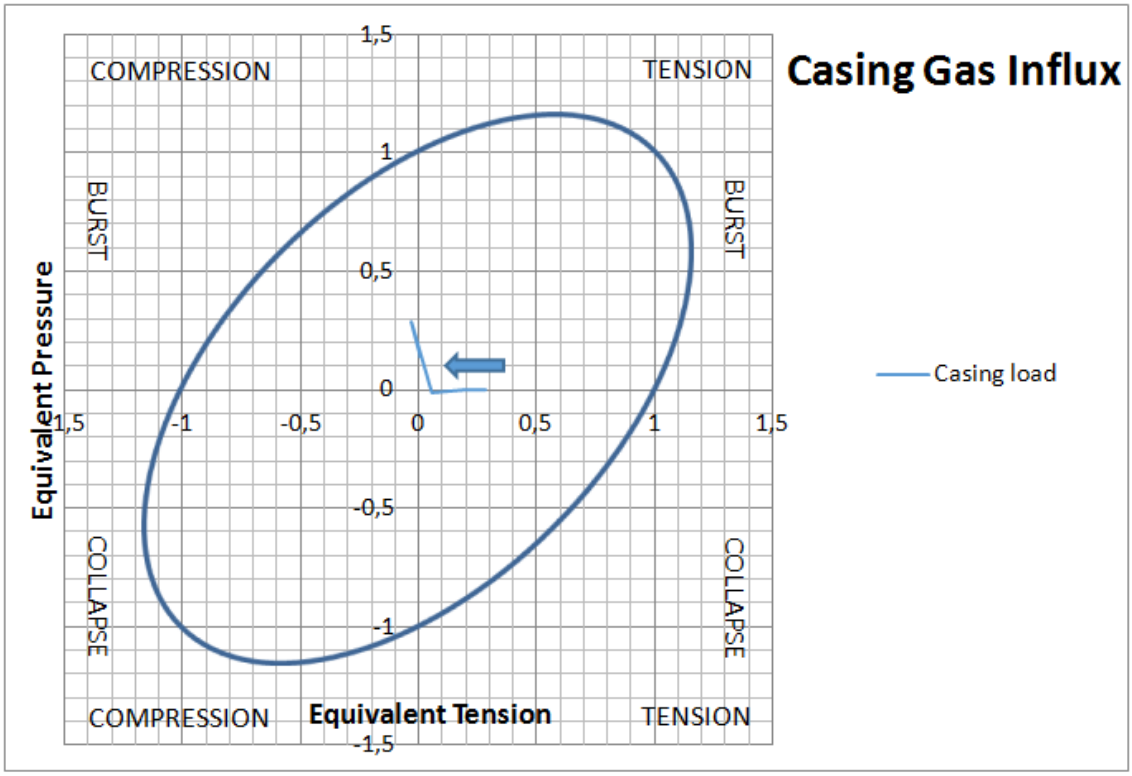

Figure 69: The Van Mises failure criterion shows the load path of the 9 5/8 in casing, during a shut in well according to the kick data, indicating no threat to the casings integrity. This means that higher test pressures may be selected in performing further influx tests. The arrow shows the stress state from surface to bottom.

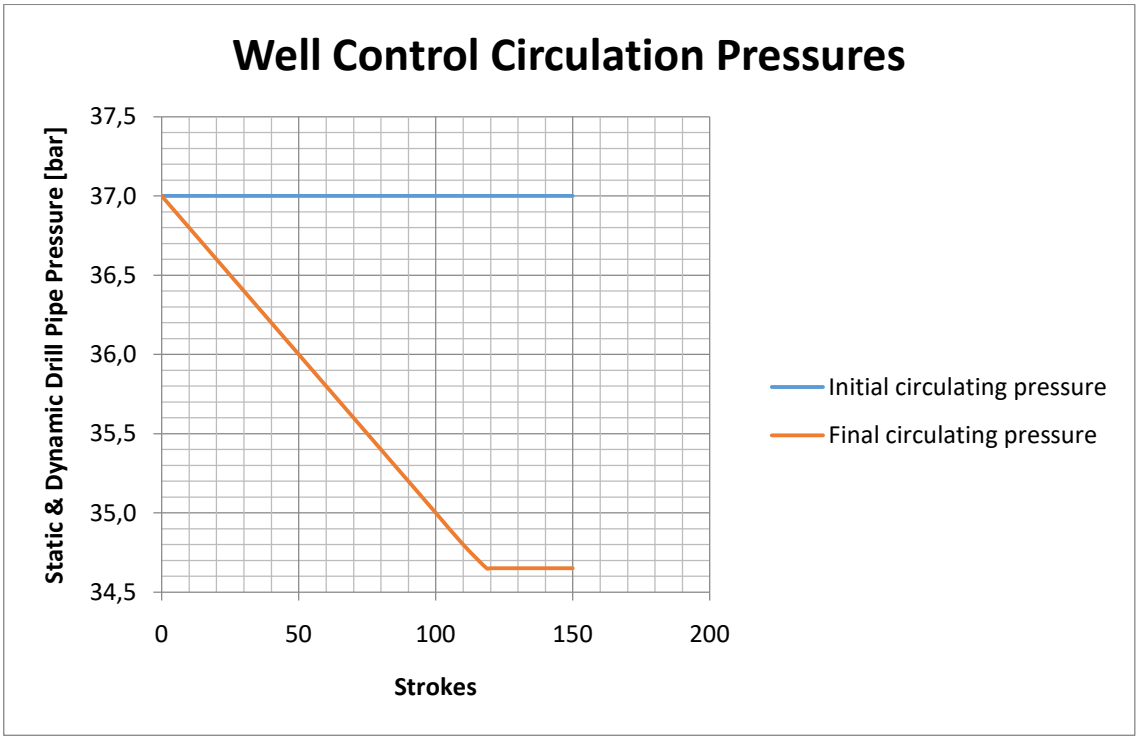

Figure 70: The second circulation of the driller's method is performed with a 12.8 ppg kill mud. The Shut In Casing Pressure (SICP) is 58.8 bar and the Shut in Drill Pipe Pressure (SIDPP) is 10.0 bar.

The completed kill sheet for vertical wells, containing the simulated formation strength data in order to create a kick intervention scenario is provided in Appendix B. It may be advised particularly in this situation for weighing up the drilling fluid, to have it premixed, as 268.4 lb/sack for every sack of the initial mixture is needed for preparation while the well is shut in [77]. Depending on the actual duration of kill mud mixing, it might exceed the migration time of the kick in a shut in well. Bleeding off the kick may also be an option.

3.2.2 Managed Pressure Drilling Test

After completing the drilling procedure under at overbalanced conditions and optional well control, a continuation onto dynamic pressure containment can be applied. By refilling the borehole within the 9 5/9 in casing with underwater foam grout and simultaneously aerating the filling continuously with the gas influx port as it gets deployed, channels are allowed to form to the surface, in order to ensure an artificial scenario of a flowing reservoir for balanced or underbalanced drilling with Managed Pressure Drilling (MPD) applications. The drilling continues with the kill mud from the previous test.

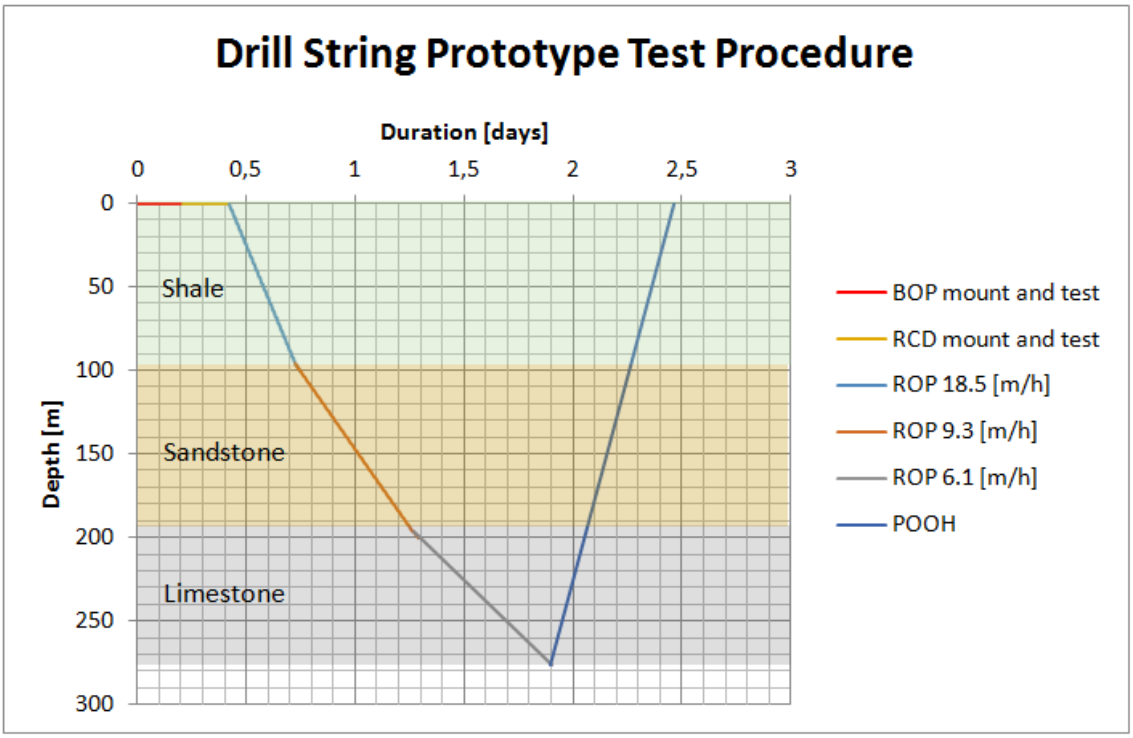

Figure 71: The test starts with mounting and testing the annular BOP and the RCD. The curing time of test cements A, B and C under heat are assumed identical to the prior test, expecting fully developed compressive strengths after 7 days.

Table 17: Critical path of operations for managed pressure drilling. The most time consuming procedure is curing the cement slurry.

Critical Path Operations				
Step [Nr.]	**Depth [m]**	**Operation**	**Duration [h]**	**Cumulative Duration [days]**
1	0	Mix foam cement 342 [l]	0.25	0.1
2	0	Mix test cement A 3,725 [l]	1.30	0.1
3	0	Mix test cement B 3,725 [l]	1.30	0.1
4	0	Mix test cement C 3,725 [l]	1.30	0.2
5	290	RIH tremie pipe (speed 720 m/h); suction pump for displaced well water	0.50	0.2
6	290	Pump slurry (pump capacity 150 l/min); activate air compressor	1.50	0.3
7	0	Activate heater; constant air compressor output; cure cement	168.00	7.3
8	0	Make BHA; Conduct UCS tests; mix drilling fluid; prepare rig for spud	0	7.3
9	0	START 7 7/8" section	0	7.3
10	0	Rig up and test annular BOP	5.00	7.5
11	290	Rig up and test RCD	5.00	7.7
12	290	Drill cement (Gross ROP 8 m/h); adjust RCD backpressure; record data	36.00	9.2
13	290	POOH (pull speed 118 m/h)	15.80	9.8
14	290	END 7 7/8" section	0	9.8

3.2.2.1 Operations Monitoring

MPD is displayed in figure 74 for a balanced and under balanced demonstration. The additional components needed are an RCD and its bias system, which are equipped onto the permanent integrated circulation system, fit for closed loop application [78].

Figure 72: The fitting RCD for the annular BOP top flange is the SafeShield Model 1000 from Weatherford ([79] p.1.).

The back pressure control can either be adjusted by manual chokes for constant influx, as intended for this particular test or automatically with the MPD bias system, should the desire arise for an ongoing influx pressure and flow rate manipulation. The constant setting of the gas influx pump is at a flow rate of 0.8 m^3/min at 100 bar to simulate pore pressure.

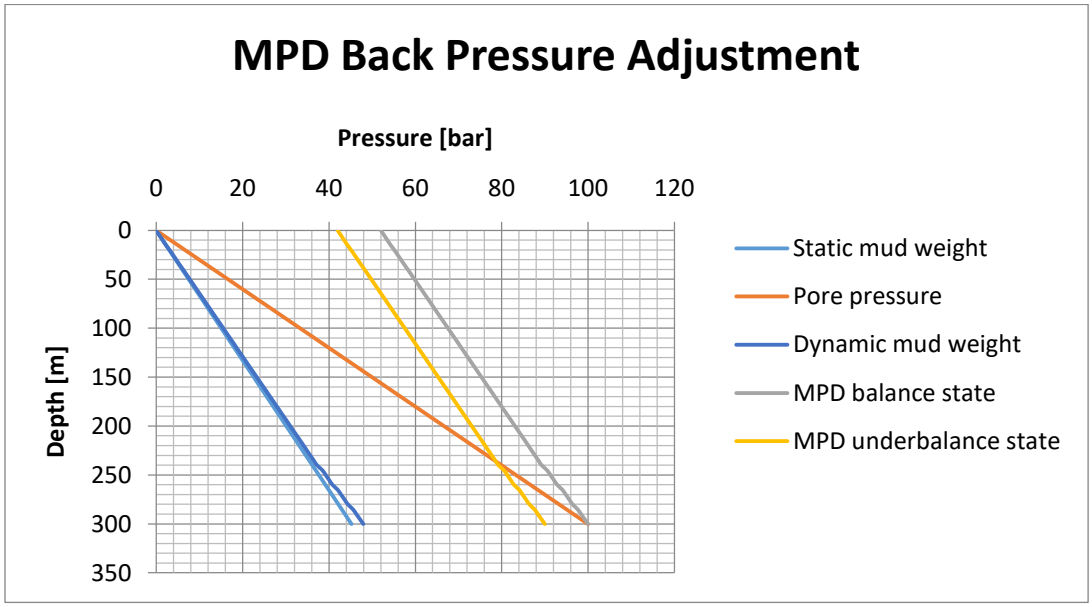

Figure 73: The pressure profile during the drilling operation with 10 bar underbalance for a flowing well.

Monitoring the casings integrity during this test shows the combined pressures of ECD, back pressure and influx pressure in a balanced state, resulting in 200 bar at a depth of 290m.

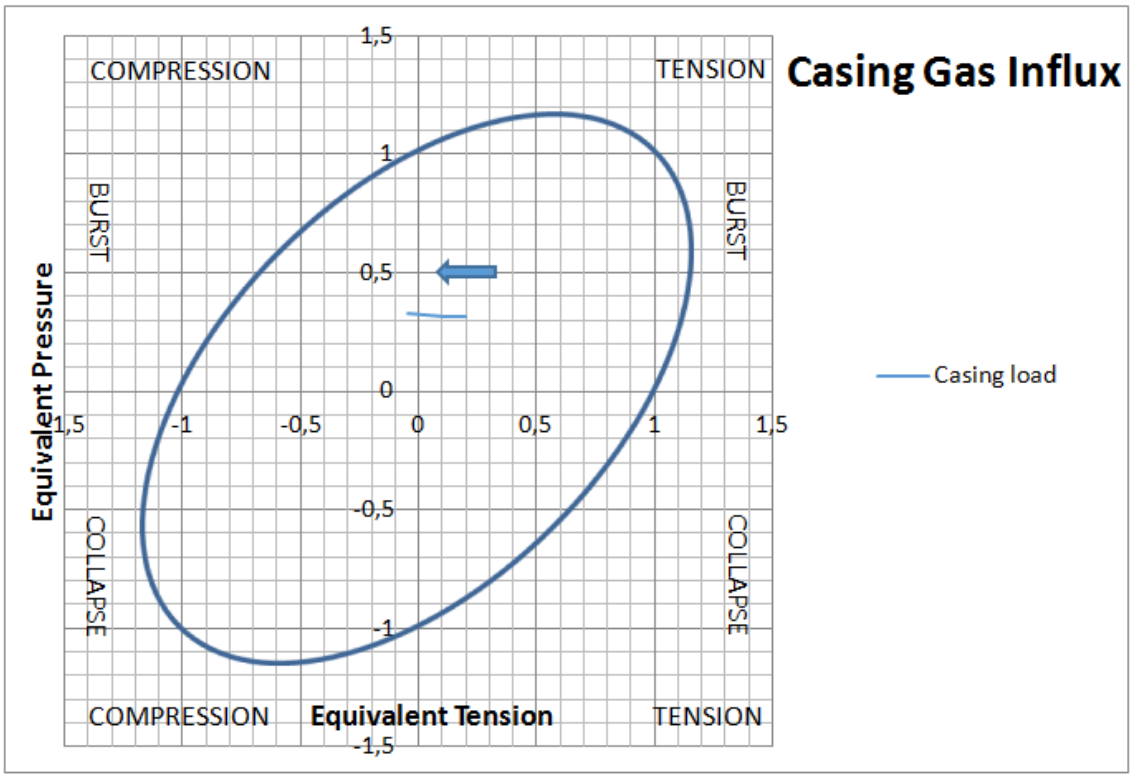

Figure 74: The Van Mises failure criterion shows the load path of the casing at balanced drilling. Higher pressures can be applied onto the casing without damaging its integrity, however the dynamic pressure limit of the utilized RCD, in this case 1000 psi should not be exceeded and lays above the balanced state back pressure of 754 psi at the surface.

Chapter 4 Cost Estimation

The facilities design purpose as stated in this thesis, is mainly for gathering a wide range of performance data, to improve the prototype and is free from the intent of commercial application.

4.1 Acquisition Cost

The acquisition costs involve all elements within the modules and sub modules, displayed in the system architecture. Equipment which already is pre existing from the former drilling test stand are included in the cost estimates within the contingency margin, refurbishment costs. A more detailed list can be viewed in Appendix C.1.

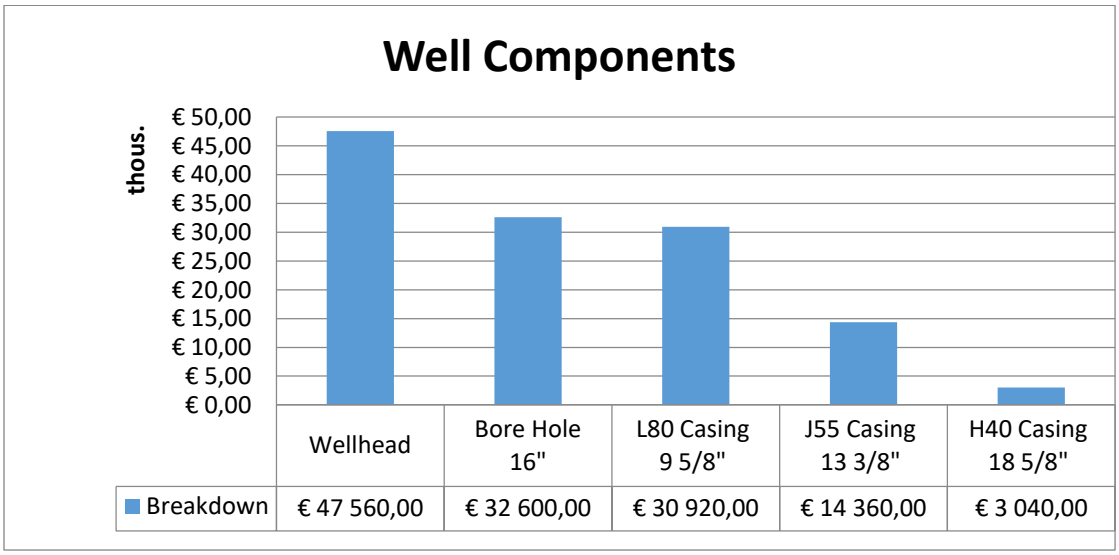

Figure 75: The largest cost driver amongst the well equipment is the well head, mainly the annular BOP and its control unit. The drilling and completion costs show similar values to the 9 5/8 in casing equipment costs. This is due to the casings interior and modifications.

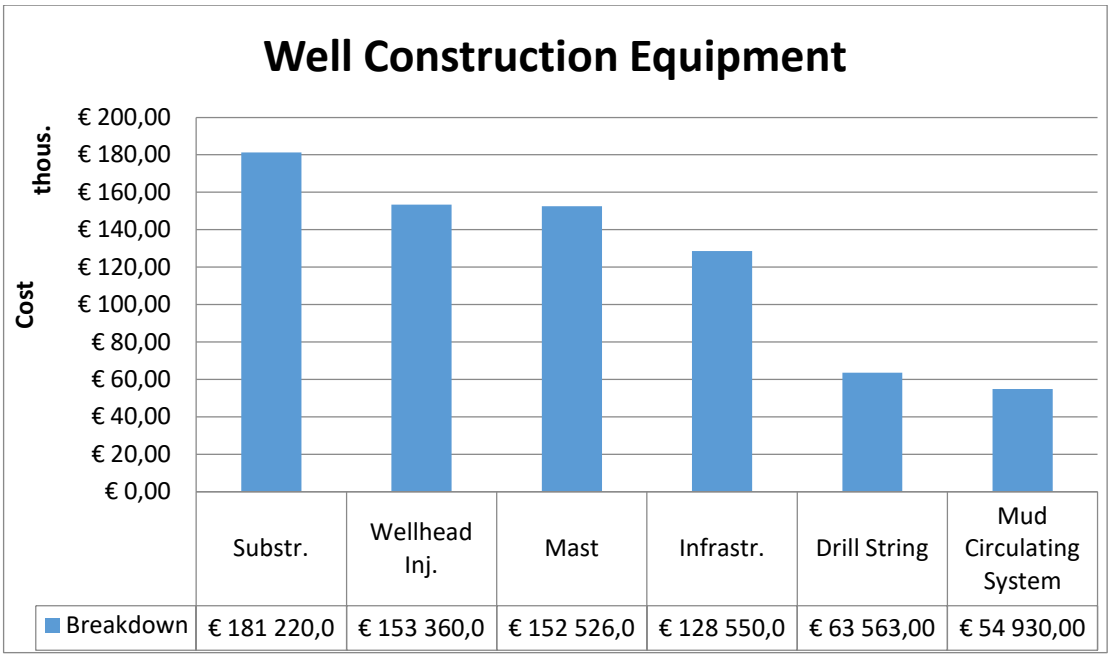

Figure 76: The cost breakdown shows the highest amount for the substructure. The major cost drivers for this portion are the iron roughneck and the automated pipe handler. For the well head injectors, the largest cost can be booked for the electric industrial heater and for the infrastructure the fully furnished work shop.

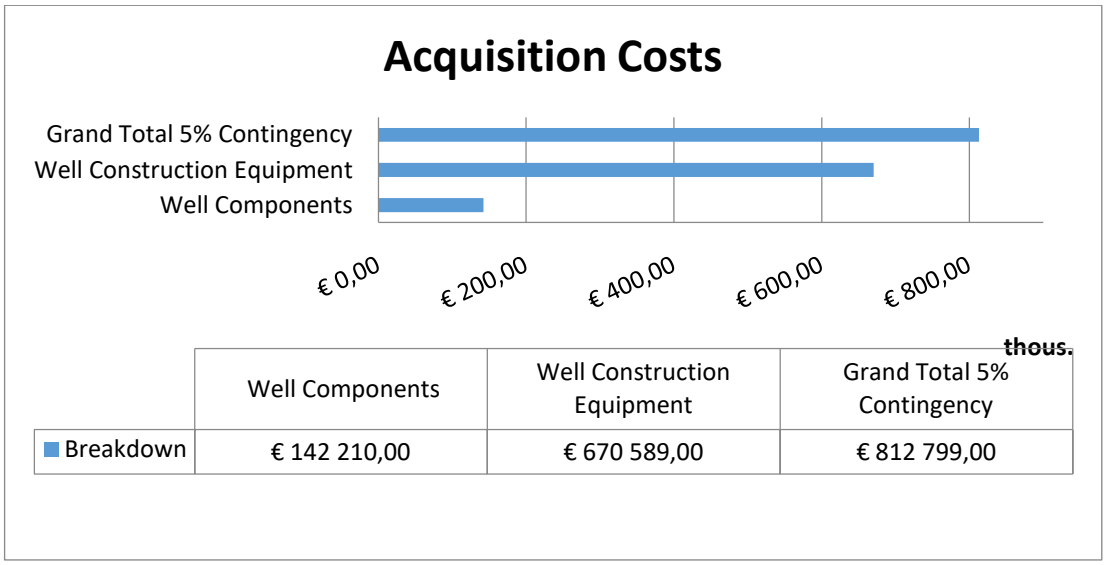

Figure 77: Cost comparison of the two main groups and the overall cost for the facility extension. A 5% contingency to the acquisition costs were added as an estimate to refurbish the former equipment based on inspection, such as gaskets, conduits of various auxiliary hydraulic units, hydro motors of the top drive. It may occur, that among inspection, it would be more cost effective to invest into new equipment, as minor repairs might present a temporary solution, however more expensive on the long run.

4.2 Test Cost Estimation

The cost breakdown for both tests are grouped into 4 categories and compared with one another. A tabular form of each cost for both tests can be viewed in more detail in Appendix C.2. In general the test durations and the resulting costs can vary, depending on how much acquired data is necessary to interrupt an ongoing test. However to illustrate the emerging cost drivers, it is necessary to prepare the sight to its full capacity.

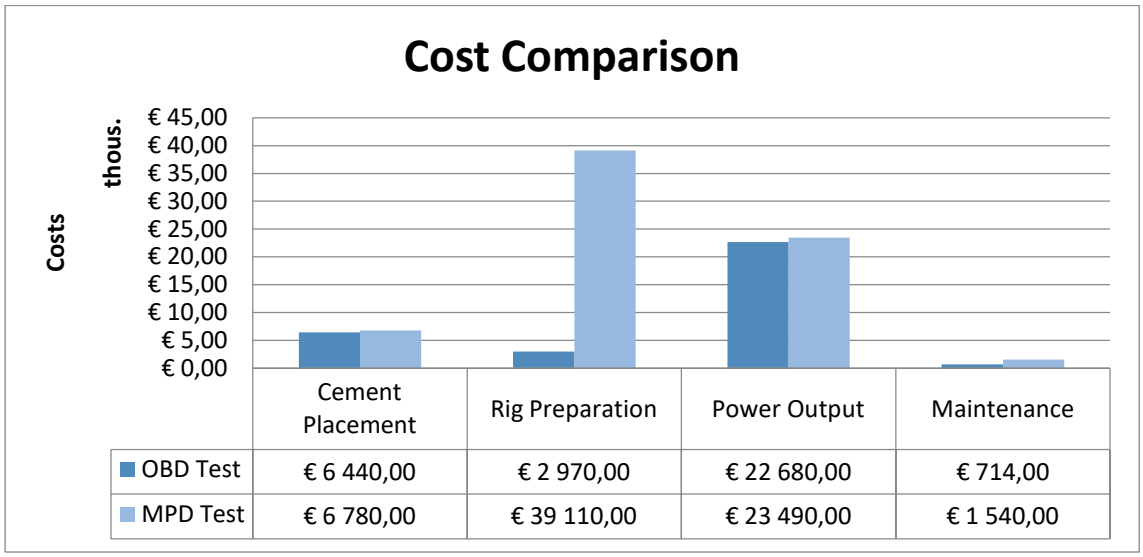

Figure 78: Comparison shows similar overall group costs. The cement fill is slightly higher due to the foaming agent and the influx compressor power consumption. Main cost driver in power output for both cases is caused by the industrial electric heater. An obvious peak can be observed in the rig preparation, initiated by the MPD system rental and day rates of two staff members.

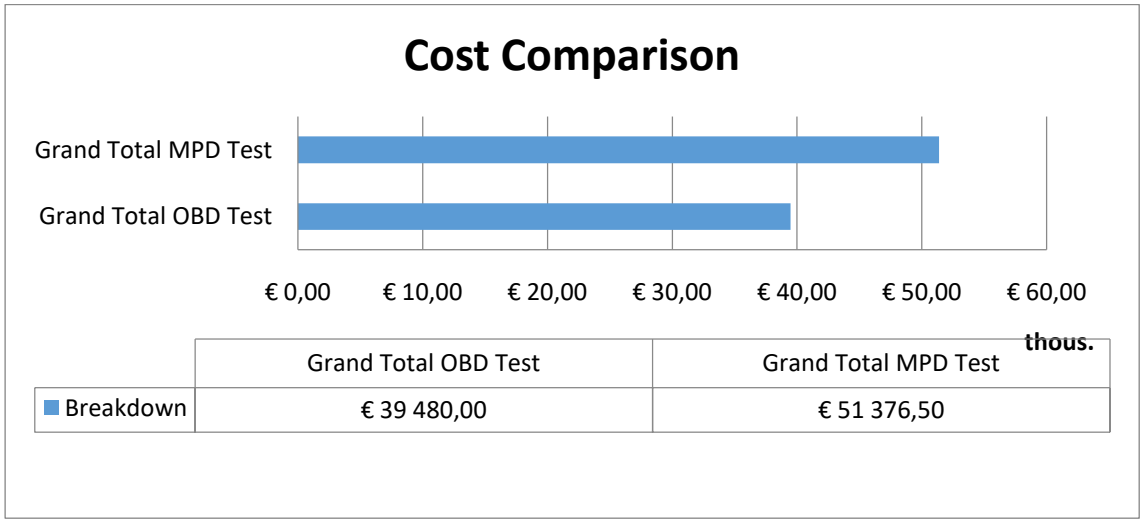

Figure 79: Comparison of the overall costs per test run resulting in higher costs for MPD conditions.

Chapter 5 Further Research

5.1 High Temperature Sensors

As the global trend expands to access deeper reservoirs, in order to counter the increasing demand of hydrocarbons, the technical conditions imposed by the down hole environment becomes more challenging. HPHT wells often have temperatures above 140°C at pressures of at least 700 bar. These conditions force the down hole tools to stretch onto new operational limits in terms of integrity, durability and functionality. This is not only true for equipment on which one can address physical strength to, but also on the interior life, made up of measuring equipment, which might evaluate erroneous data or worst, break down completely under these extreme conditions.

5.1.1 High Temperature Environment

The only option is to make changes on the present casings due to their stress states on higher temperatures and pressures. The currently installed Industrial heater is designed for a pressure drop from 90 bar to 50 bar to ensure a vapour phase before injecting steam down hole, in order to overcome the hydrostatic pressure within the annulus with a surplus of less than 20 bar and heat loss, without suffering a water hammer due to a phase change according to the water phase diagram [80].

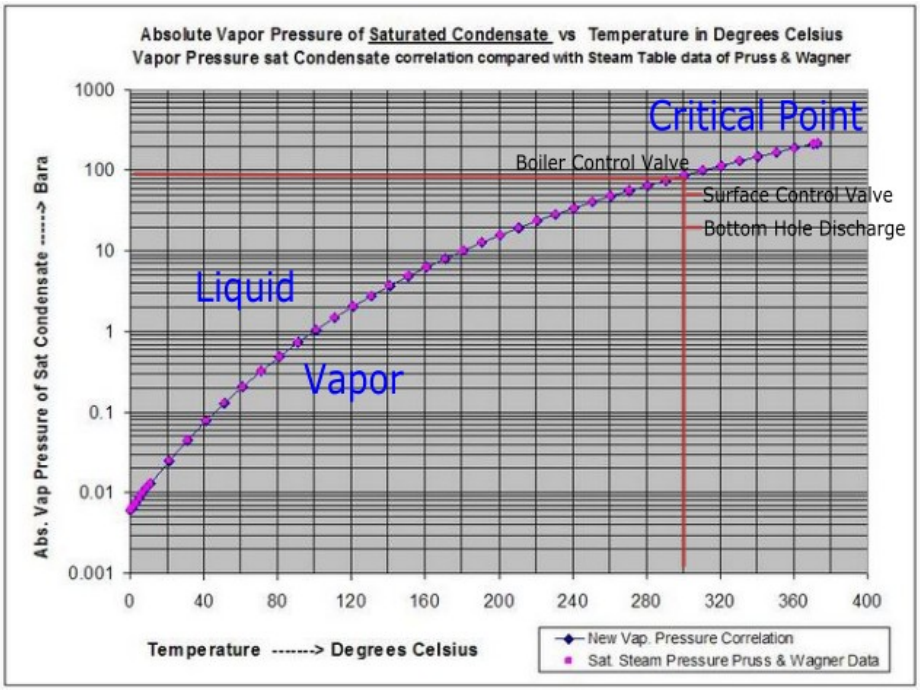

Figure 80: Steam pressure drop, assuming constant temperature.

Therefore it is capable of supplying approximately 303°C of steam for higher heating temperatures, therefore throttled with a thermostat and failsafe measures like strain gouges on the casings in case of malfunctions. This also means that the influx conduits need to be fitted to sustain higher temperatures than the currently installed hydraulic tubes rated with 150°C, similar to the heating conduit material made from alloy steel for high pressure, high temperature applications [81]. Moreover, the redesign of 13 5/8 in casing and its cement sheet need to be evaluated to guarantee its long life integrity.

5.1.2 High Pressure Environment

The limiting factors to increase the internal pressure of the 9 5/8 casing, is the RCDs static and dynamic pressure limitation. As shown by the side glances to the casings integrity on every critical operation, it leaves sufficient room to increase the casing load in terms of internal pressure. By choosing the right MPD system, regarding pressure rating prior to rental, a higher pressure environment for the drill string prototype can be achieved.

5.1.3 Drill String Dynamics

The last ingredient to build a most realistic environment in order to test these sensors is to excite vibrations onto the drill string as most of them are encapsulated by a silicone substance [82]. Vibrations are natural to occur in every drilling operation as soon as the bit rotates off its natural geometric centre of rotation. More specific is the phenomenon addressed as, bit whirl, the backward whirl being the most hazardous for drill string life, however in literature others claim that axial vibration mechanisms are the reason for this phenomenon [83]. However the case may be, an amplification of axial vibrations can easily be achieved, in adding determined amounts of inhomogeneities into the test cement compound, such as gravel streaks or as an additional constituent.

5.2 Over-pressured Zones

It is stated in literature that several methods exist to predict over-pressured zones. The ideal case would be observing off set wells, to prepare the driller, when the approximate depth is soon to be encountered during drilling. The unintegrated techniques consist of surface parameter changes, such as sudden increase in ROP, which may also just indicate a transition onto a softer rock formation or a false drilling break interpretation of a stuck centraliser that has come free. Such uncertain events where in some cases the sudden increase in ROP is double the amount of the current value, forces the driller virtuously to perform a flow check or close the BOP, however resulting in unnecessary non productive time. Another method, based on real time measurements is the Instantaneous Drilling Evaluation Log (IDEL), which calculates rock strength from surface drilling parameters, accounting empirically for bit wear and

bit type, in order to differentiate shale from other formations for its pore pressure estimations. More advanced is the Pressure Evaluation in Real Time method (PERT), using down hole mechanical data in conjunction with gamma ray, resistivity and neutron-density measurements performed by the Measurement While Drilling (MWD) and Logging While Drilling (LWD) tools, as an integrated technique. Future goals are to predict over pressure ahead or at the bit during drilling [84]. Such environment can be reconstructed within the 9 5/8 in casing. An alternating cement fill from very soft to medium hard formations can be cured. During drilling, the pup joints chamber can be preloaded with pressure. As the formations get drilled off, the drill string prototype had encountered a given amount of formation related drilling breaks. Near bottom, the last sealing increment of the test cement will be pierced, releasing overpressure. This set up is a possible method for the prototype sensors, to distinguish a formation related drilling break from an over-pressure related drilling break.

Chapter 6 Conclusion

Given the starting point of present equipment regarding the former drilling test stand, on which the extensions are built upon, a successful synergy between both testing platforms were achieved to fulfil the assigned objectives and serves as a solid basis within its technical limitations. However several steps yet need to be taken from the conceptual phase to realization.

By investigating the environmental as well as activity related loads from subsurface to surface, the components prone to stress concentrations are highlighted and dimensioned accordingly within the scope of practical disciplinary design methods and appropriate safety. However it is also clear that deeper investigations concerning long life fatigue regarding elements such as the mast or pup joint, need to be examined for low and high frequency loads and may result in a different design entirely after FE analysis.

The current modular system architecture created for the testing facility, makes it manageable to exchange components, should the desire exist to increase or decrease certain operational parameters and reincorporating former sensory equipment as well as reproducing and extending the sensory capability onto the new structure.

One aspect, which can never be left out, is the human factor. This thesis is geared towards overcoming technical design limitations on a broad scale, on the behalf of drilling and mechanical engineering, elicited by the assigned testing capabilities and upholding its integrity. As it is intended to operate the facility between 3 or 4 individuals, the detailed working ergonomics, such as control panels and safety measures, such as protective barriers, need yet to be elaborated.

Building on the findings of this thesis, the presented basis bears the potential of providing a challenging testing environment for the drill string prototype.

Appendix A General Appendices

A.1 Well Components

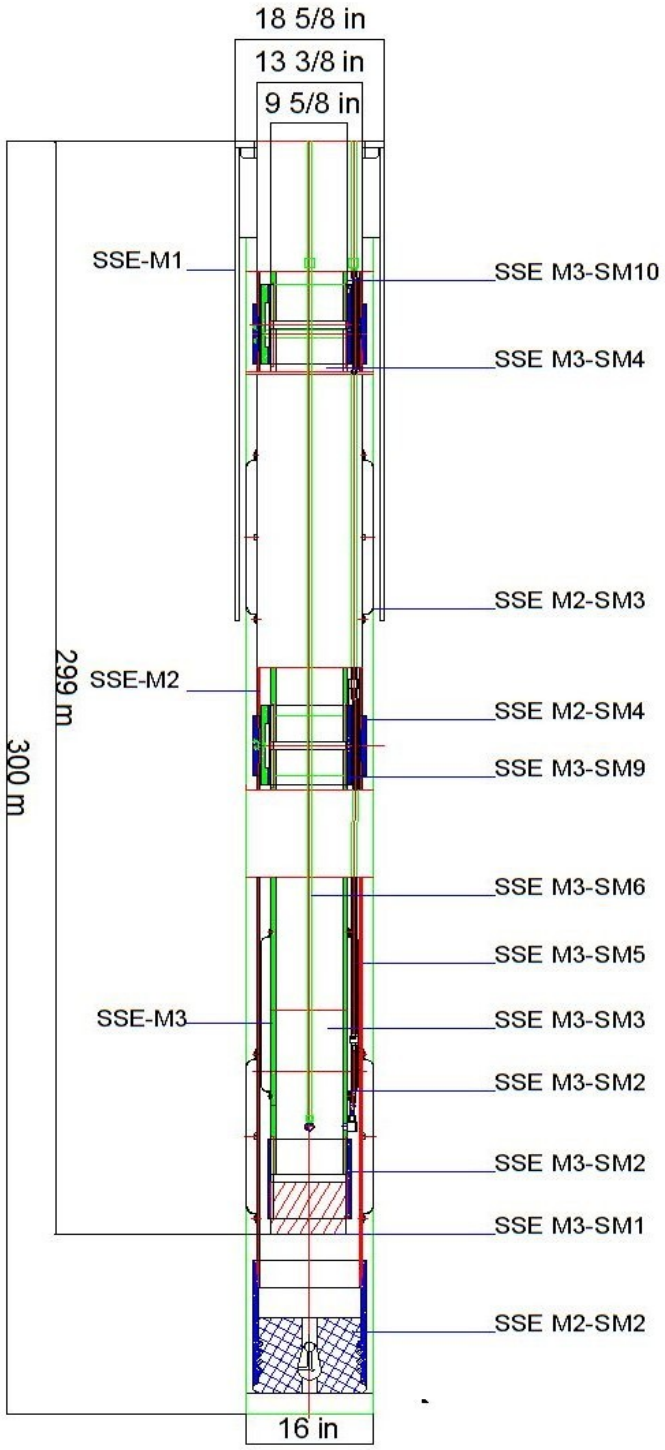

Figure A.1. 1: Well schematic of an assembled unit compiled in AutoCAD. The display shows the bottom most casing coupling with the form lock mechanism.

A.2 Redesign

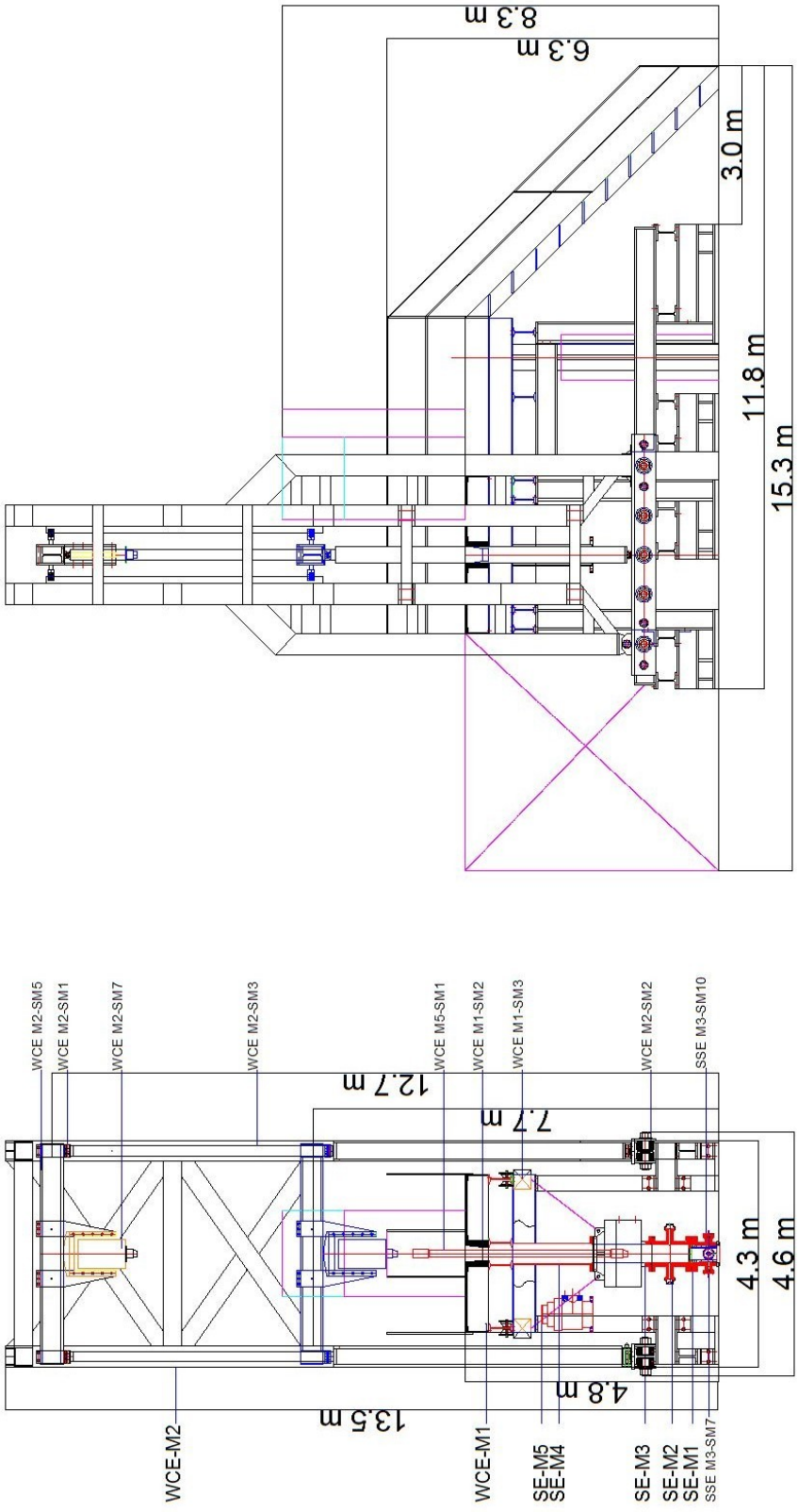

Figure A.2. 1: Front and side view of the substructure and mast in form of a compilation draft in AutoCAD with no cross rods in the side view.

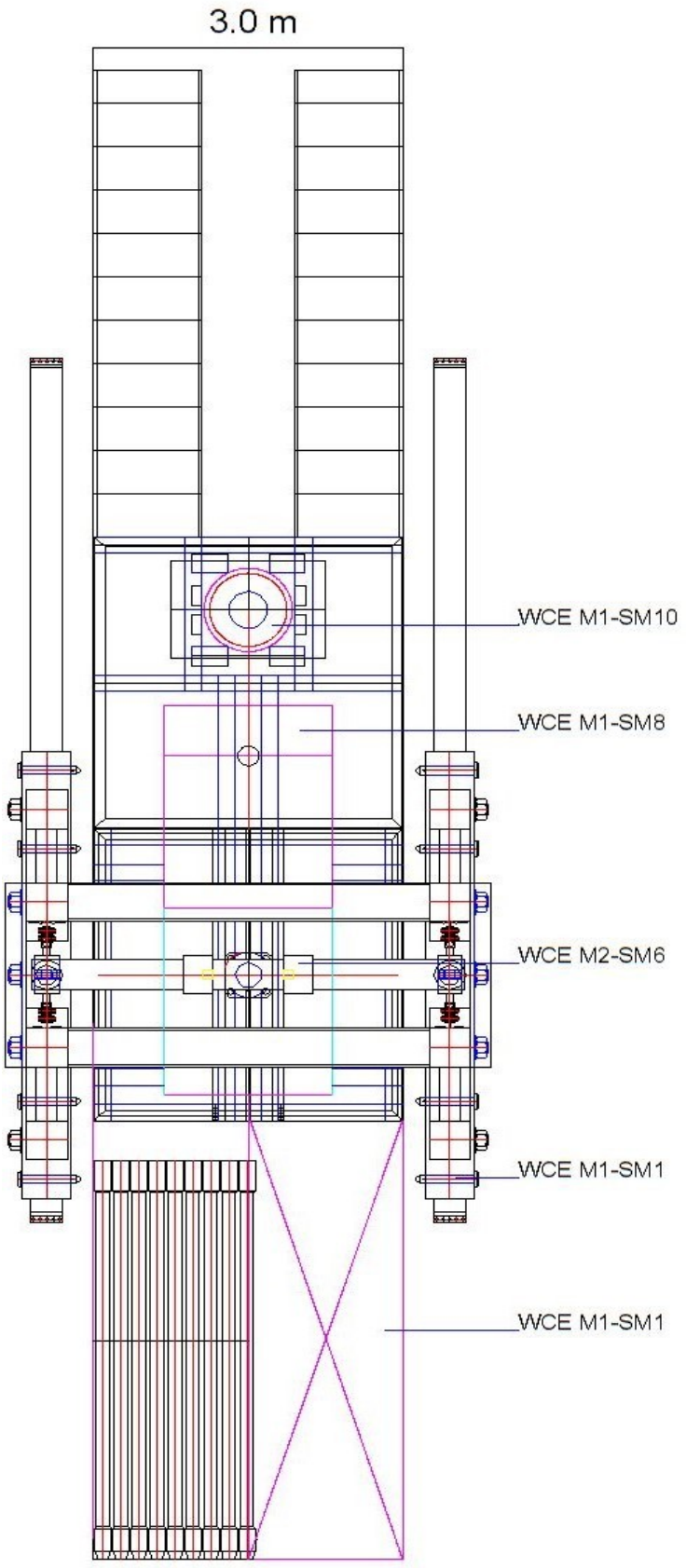

Figure A.2. 2: Plane view of the substructure and mast in form of a compilation draft in AutoCAD.

Table A.2. 1: Design loads of the radial steel plate and the torque bushing.

Component	Load Comparison [N/mm²]	
SSE M2-SM4 (Radial Steel Plate)	$\mathcal{T}_{max} \leq \mathcal{T}_a$	$41.5 \leq 140$
SSE M3-SM9 (Torque Bushing)	$\delta v \leq \delta w$	$84 \leq 407$

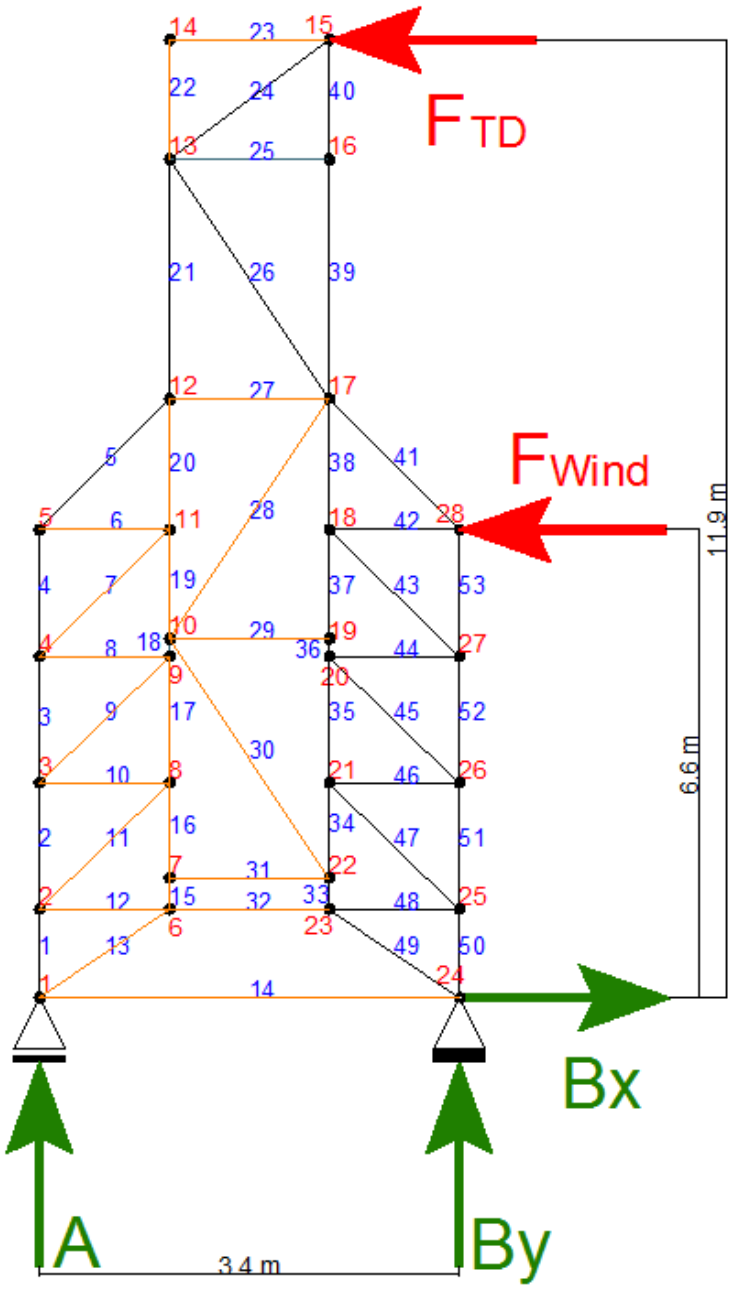

Figure A.2. 3: The truss in side view display for basic static evaluation. The active force for the top drive F_{TD} normally has its working point at the cylinder upper dead point, which is lower than depicted in the figure. The same applies for the maximum wind force F_{Wind}, which has its working point according to the centre of the area projected from the front view. Both forces were lifted slightly, which would increase the reaction forces as a side effect, but in order to vector in the forces into the truss nodes. The force free rods are coloured in orange.

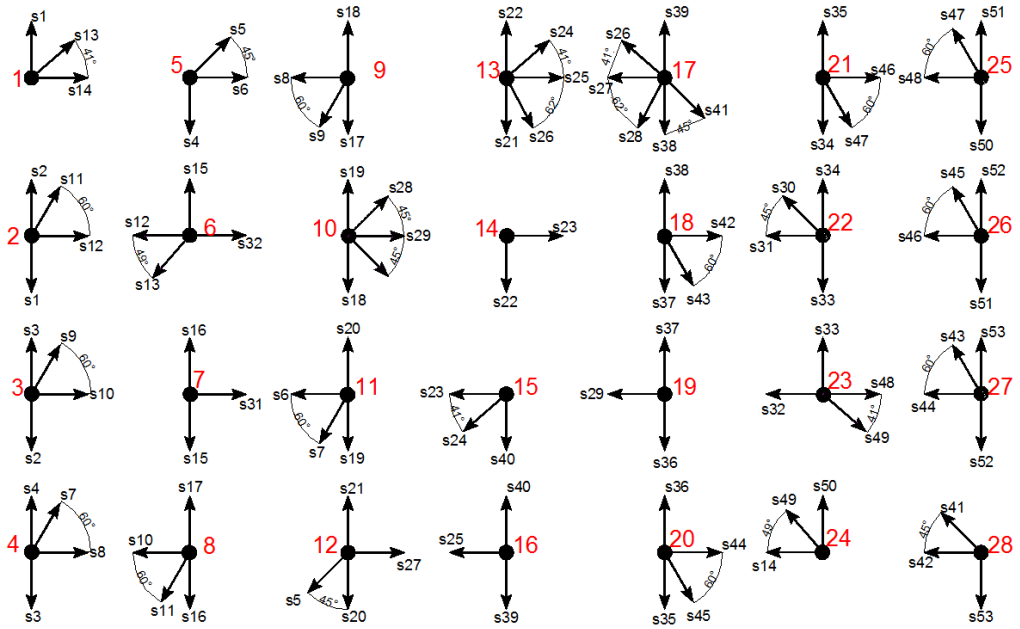

Figure A.2. 4: The truss nodes in order, representing 28 equation systems.

Table A.2. 2: The summarized rod forces of the truss in front view. Negative values indicate rods in compression.

Rod Forces [N]					
S1=	-21,967.10	**S19=**	0	**S37=**	32,413.00
S2=	-21,967.10	**S20=**	0	**S38=**	45,368.40
S3=	-21,967.10	**S21=**	-9,982.5	**S39=**	3,155.50
S4=	-21,967.10	**S22=**	0	**S40=**	3,155.50
S5=	31,066.20	**S23=**	0	**S41=**	5,133.60
S6=	0	**S24=**	-4,809.80	**S42=**	-7,479.80
S7=	0	**S25=**	0	**S43=**	14,959.65
S8=	0	**S26=**	7,732.10	**S44=**	-7,479.80
S9=	0	**S27=**	0	**S45=**	14,959.70
S10=	0	**S28=**	0	**S46=**	-7,479.80
S11=	0	**S29=**	0	**S47=**	14,959.60
S12=	0	**S30=**	0	**S48=**	-7479.80
S13=	0	**S31=**	0	**S49=**	9,910.90
S14=	0	**S32=**	0	**S50=**	15,465.00
S15=	0	**S33=**	6,502.10	**S52=**	-10,445.85
S16=	0	**S34=**	6,502.10	**S53=**	-23,401.30
S17=	0	**S35=**	19,457.50	-	-
S18=	0	**S36=**	32,413.00	-	-

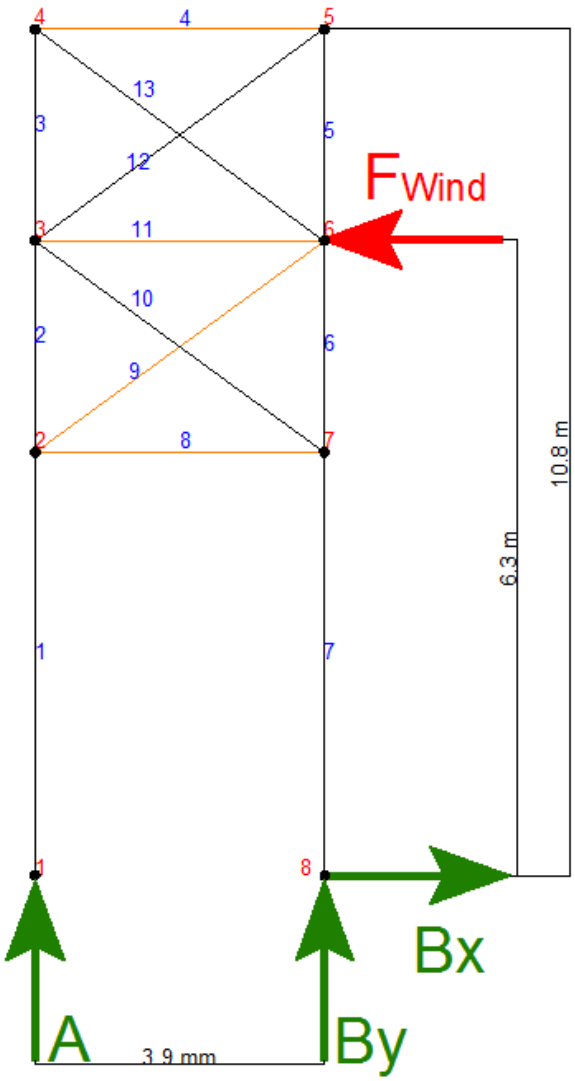

Figure A.2. 5: The truss from the side view, exposed to the wind being the only force, vectored in at the height of the front view centroid of area. Force free rods are highlighted in orange.

Table A.2. 3: The summarized rod forces of the truss in side view. Negative values indicate rods in compression.

Rod Forces [N]					
S1=	-7,239.3	**S7=**	7,239.3	**S12=**	3,161.8
S2=	-7,239.3	**S8=**	0	**S13=**	18,945.0
S3=	-10,866.4	**S9=**	0	-	-
S4=	0	**S10=**	-3,161.8	-	-
S5=	5,425.8	**S11=**	0	-	-

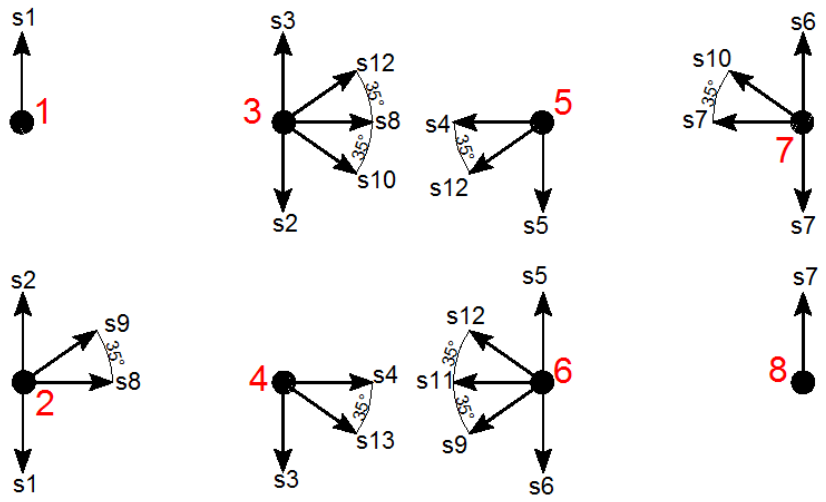

Figure A.2. 6: The truss nodes in order, representing 8 equation systems.

Table A.2. 4: The dimensioning of the critically stressed components designed with triple the drill string load.

Component	Load Comparison [N/mm²]	
WCE-M1 Substructure	$б_b \leq б_a$	$119.4 \leq 180$
WCE M2-SM5 Travelling Beam	$б_b \leq б_a$	$161.7 \leq 180$
WCE-M2 Mast	$б_b \leq б$	$4.4 \leq 205$
WCE M2-SM5 (Lock Pin)	$б_b \leq 0.2 \times R_m$	$157.2 \leq 205$
WCE M2-SM1 Lock Pins	$б_b \leq 0.2 \times R_m$	$186.7 \leq 220$
	$\mathcal{T} \leq 0.15 \times R_m$	$5.1 \leq 220$
	$P \leq 0.15 \times R_m$	$9.7 \leq 205$

Appendix B Drilling Programme

B.1 Well Control

Figure B.1. 1: The mud properties utilized for OBD.

Mud Properties			
Viscosity [cp]	10		
Yield Point [lbf/100 sqft]	10		
Density [ppg]	10		
Constituents	Density [ppg]	Volume [gal]	Weight [lb]
Drill Water	8.34	9,139.13	76,220.31
Bentonite	20.02	355.24	7,110.58
Polymer	20.02	5.92	118.51
Caustic Soda	-	neglected	118.51
Soda Ash	-	neglected	59.25
Barite (@ kick)	35.03	454.52	15,920.96
Barite (@ kill)	35.03	1,498.94	52,504.89

Figure B.1. 2: Data sheet for completing the kill sheet for kick intervention in a vertical well.

Well Control Data		
Hole Size		7,875 in
Hole Depth		295 m
DP	Length	160 m
	Displacement	13,14 l/m
	Capacity	9,26 l/m
	OH-Capacity	24,67 l/m
HWDP	Length	18,9 m
	Capacity	4,59 l/min
	OH-Capacity	24,67 l/m
DC	Length	113 m
	Capacity	3,13 l/min
	OH-Capacity	16,85 l/m
Mud Weight		1,198 kg/l
Leak Off Pressure		55 bar
Leak Off Mud Weight		1,8 kg/l

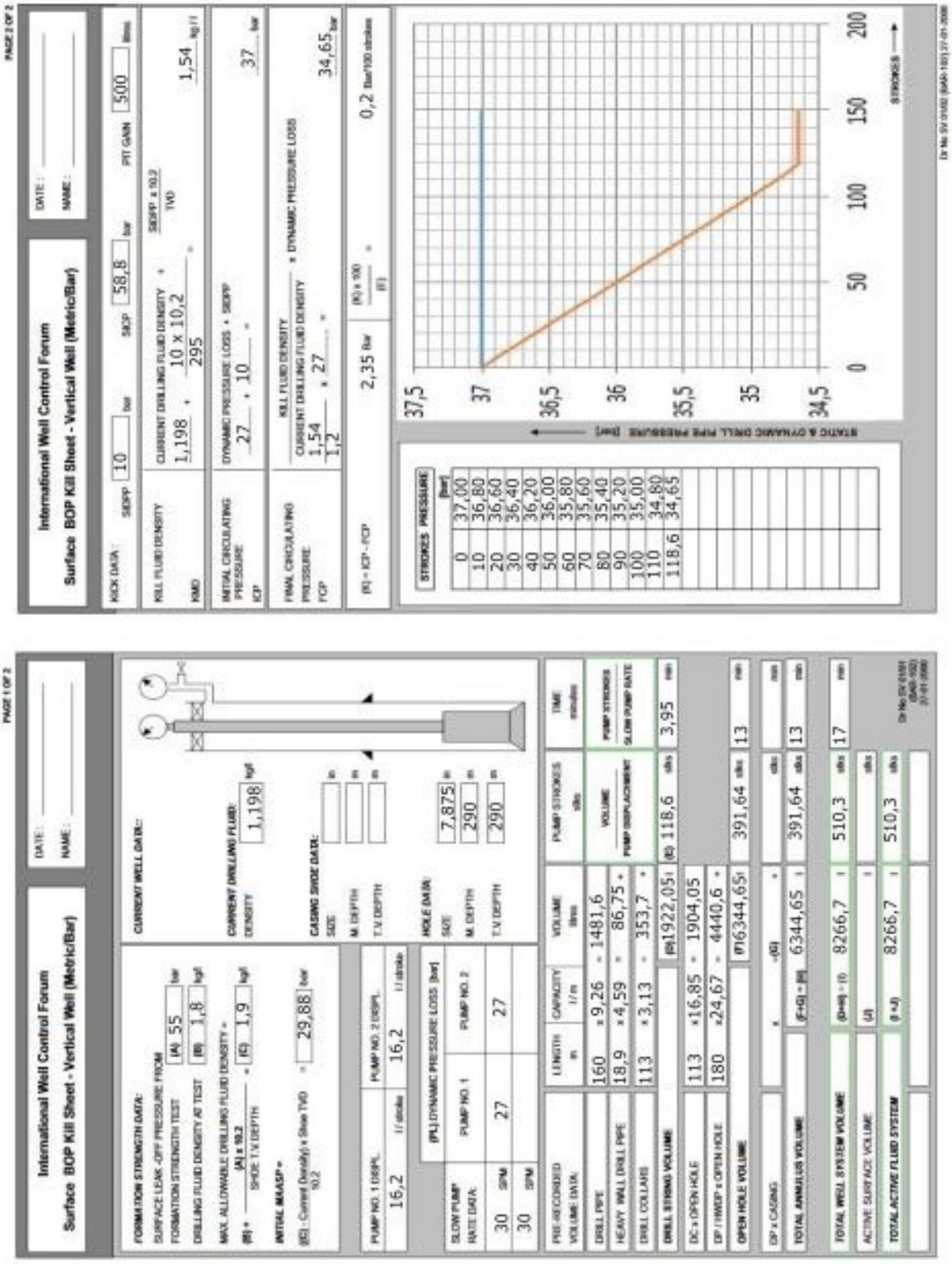

Figure B.1. 3: Utilized kill sheet for vertical wells.

Appendix C Cost Estimation

C.1 Acquisition Cost

Figure C.1. 1: Acquisition cost breakdown of the entire facility redesign with 5% Contingency to the grand total.

Acquisition Cost Breakdown						
Cost	**Cost Group**	**Unit**	**Quant.**	**Unit cost**	**Total Cost**	**Currency**
Bore Hole	16″ OH	[job]	1.00	32,600.00	32,600.00	[EUR]
Conductor	18 5/8″, 87.5 ppf, H40	[job]	1.00	3,040	3,040.00	[EUR]
Casing	13 3/8″, 54.5 ppf, J55	[ton]	24.40	565.5	13,7410.00	[EUR]
Cementing	13 5/8″, 3,000 psi	[job]	1.00	9,000.00	9,000.00	[EUR]
Drilling Mud	13 5/8″, 3,000 psi	[job]	1.00	3,800.00	3,800.00	[EUR]
Float Shoe	13 5/8″, 3,000 psi	[pcs]	1.00	175.00	175.00	[EUR]
Centraliser	13 5/8″, 3,000 psi	[pcs]	60.00	23	1,380.00	[EUR]
Casing	9 5/8″, 58.4 ppf, P110	[ton]	26.10	685	17,878.50	[EUR]
Seal Shoe	9 5/8″, 58.4 ppf, P110	[pcs]	1.00	175.00	175.00	[EUR]
Pup Joint	9 5/8″, 58.4 ppf, P110	[pcs]	1.00	1,200.00	1,200.00	[EUR]
Permeable Med.	9 5/8″, 58.4 ppf, P110	[m^3]	2.00	300.00	660.00	[EUR]
Gas Conduit	9 5/8″, 58.4 ppf, P110	[m]	300.00	4.00	1,200.00	[EUR]
Liquid Conduit	9 5/8″, 58.4 ppf, P110	[m]	300.00	4.00	1,200.00	[EUR]
Heating Conduit	9 5/8″, 58.4 ppf, P110	[m]	1,800.00	4.00	7,200.00	[EUR]
Centralizers	9 5/8″, 58.4 ppf, P110	[pcs]	60.00	19.00	1,140.00	[EUR]
Comp. Fluid	9 5/8″, 58.4 ppf, P110	[kg]	370.00	0.70	259.00	[EUR]
Strain Gauge	Well Surf. El.	[pcs]	2.00	30.00	60.00	[EUR]
Wellhead Hous.	13 5/8″, 3,000 psi	[pcs]	1.00	5,670.00	5,670.00	[EUR]
Drilling Spool	13 5/8″, 3,000 psi	[pcs]	1.00	2,230.00	2,230.00	[EUR]
Annular BOP	13 5/8″, 3,000 psi	[pcs]	1.00	11,400.00	11,400.00	[EUR]
Control BOP	Well Surf. El.	[pcs]	1.00	28,000.00	28,000.00	[EUR]
Bell Nipple	13 5/8″	[pcs]	1.00	200.00	200.00	[EUR]
Substructure	Substructure	[job]	1.00	12,385.00	12,385.00	[EUR]
Pipe Handler	Substructure	[pcs]	1.00	68,300.00	68,300.00	[EUR]
Master Bushing	Substructure	[pcs]	1.00	1,170.00	1,170.00	[EUR]
Lift Trolley	Substructure	[pcs]	2.00	1,000.00	1,000.00	[EUR]
Pneumatic Slips	Substructure	[pcs]	1.00	3,400.00	3,400.00	[EUR]
Safety Collar	Substructure	[pcs]	1.00	200.00	200.00	[EUR]
IBOP	Substructure	[pcs]	1.00	3,000.00	3,000.00	[EUR]

Iron Roughneck	Substructure	[pcs]	1	90,000.00	90,000.00	[EUR]
Cell Socket	Substructure	[pcs]	1	0.00	0.00	[EUR]
Pressure Cell	Substructure	[pcs]	1	0.00	0.00	[EUR]
Cell Hoist	Substructure	[pcs]	1	0.00	0.00	[EUR]
Mast	Mast	[job]	1	30,960.00	30,960.00	[EUR]
Lock Pins	Mast	[pcs]	12	27,5	330.00	[EUR]
Roller Bearings	Mast	[pcs]		10	67.00	[EUR]
Hydraulic Hoist	Mast	[pcs]	2	12,710.00	12,710.00	[EUR]
WOB Bias	Mast	[pcs]	1	92,350.00	92,350.00	[EUR]
Travelling Beam	Mast	[pcs]	1	1,800.00	1,800.00	[EUR]
TD Mount	Mast	[pcs]	1	1,000.00	1,000.00	[EUR]
Drive Pin	Mast	[pcs]	1	0.00	0.00	[EUR]
Return Line	Mud Circ. Sys.	[pcs]	1	30.00	30.00	[EUR]
Flow Paddle	Mud Circ. Sys.	[pcs]	1	80.00	80.00	[EUR]
Mud Gas Sep.	Mud Circ. Sys.	[pcs]	1	14,500.00	14,00.00	[EUR]
Choke-Kill Man.	Mud Circ. Sys.	[pcs]	1	10,000.00	10,000.00	[EUR]
Cell Separator	Mud Circ. Sys.	[pcs]	1	0.00	0.00	[EUR]
Mixing-Recyc.	Mud Circ. Sys.	[pcs]	1	30,000.00	30,000.00	[EUR]
Cuttings Deposit	Mud Circ. Sys.	[pcs]	1	320.00	320.00	[EUR]
Mud Pump	Mud Circ. Sys.	[pcs]	1	0.00	0.00	[EUR]
DP NC50	5", 4 9/32", 19,5 ppf	[ton]	4.66	4,500.00	20,970.00	[EUR]
HWDP NC50	5", 3", 50 ppf	[ton]	1.4	5,200.00	7,280.00	[EUR]
DC NC50	6 ¾", 2 13/16", 100,7 ppf	[pcs]	10	2,550.00	25,,500.00	[EUR]
X-Over	Drill String	[pcs]	1	500.00	500.00	[EUR]
Stabilizer	Drill String	[pcs]	1	1,500.00	1,500.00	[EUR]
Bit Sub	Drill String	[pcs]	1	790.00	790.00	[EUR]
Tri-cone Bit	Drill String	[pcs]	1	850.00	850.00	[EUR]
PDC Bit	Drill String	[pcs]	1	1,170.00	1,170.00	[EUR]
Fishing Tools	Drill String	[pcs]	2	2,500.00	5,000.00	[EUR]
Industrial Heater	Wellhead Inj.	[pcs]	1	145,710.00	145,710.00	[EUR]
Gas Compressor	Wellhead Inj.	[pcs]	1	7,060.00	7,060.00	[EUR]
Liq. Pump	Wellhead Inj.	[pcs]	1	590.00	590.00	[EUR]
Work Shop	Infrastructure	[job]	1	110,340.00	110,340.00	[EUR]
Fork Lift	Infrastructure	[pcs]	1	15,200.00	15,200.00	[EUR]
Concrete Press	Infrastructure	[pcs]	1	3,010.00	3,010.00	[EUR]
TOTALS					812,800.00	[EUR]

C.2 Test Cost Estimation

Figure C.1. 2: Cost breakdown of the overbalanced drilling test with 5% contingency to the grand total.

OBD Test Cost Breakdown					
Cost	**Unit**	**Quantity**	**Unit Cost**	**Total Cost**	**Currency**
Cement Fill A	[m³]	3.30	221.00	729.00	[EUR]
Cement Fill B	[m³]	3.30	232.00	766.00	[EUR]
Cement Fill C	[m³]	3.30	301.00	993.00	[EUR]
Truck Standby	[h]	7.00	100.00	700.00	[EUR]
Pumping	[m³]	10.00	25.00	250.00	[EUR]
Staff	[job]	2.00	500.00	1,000.00	[EUR]
Transport	[m³]	1.00	2,000.00	2,000.00	[EUR]
BOP Rig Up	[h]	1.50	70.00	105.00	[EUR]
BOP Test	[h]	3.50	70.00	245.00	[EUR]
BHA Make Up	[h]	2.00	70.00	140.00	[EUR]
Mud Preparation	[h]	2.00	70.00	140.00	[EUR]
Mud Chemicals	[job]	1.00	3,100.00	3,100.00	[EUR]
Lab. Test	[h]	32.00	70.00	2,240.00	[EUR]
Rig Auxiliary	[kW]	7,900.00	0.32	2,550.00	[EUR]
Mud Pump	[kW]	14,544.00	0.32	4,650.00	[EUR]
Industrial Heater	[kW]	48,000.00	0.32	15,360.00	[EUR]
Fuel Consumption	[l]	120.00	1.00	120.00	[EUR]
Water	[m³]	142.00	2.00	284.00	[EUR]
Cuttings Disposal	[job]	1.00	220.00	220.00	[EUR]
Maintenance	[job]	3.00	70.00	210.00	[EUR]
TOTALS				**39,840.00**	**[EUR]**

Table C.2. 1: Cost breakdown of the MPD test with 5% contingency to the grand total.

MPD Test Cost Breakdown					
Cost	**Unit**	**Quantity**	**Unit Cost**	**Total Cost**	**Currency**
Cement Fill A	[m³]	3.20	221.00	707.00	[EUR]
Cement Fill B	[m³]	3.20	232.00	742.00	[EUR]
Cement Fill C	[m³]	3.20	301.00	963.00	[EUR]
Foaming Agent	[m³]	0.07	1,585.00	111.0	[EUR]
Truck Standby	[h]	10.00	100.00	1000.00	[EUR]
Pumping	[m³]	10.00	25.00	250.00	[EUR]
Staff	[job]	2.00	500.00	1,000.00	[EUR]
Transport	[m³]	1.00	2,000.00	2,000.00	[EUR]
BOP Rig Up	[h]	1.50	70.00	105.00	[EUR]
BOP Test	[h]	3.50	70.00	245.00	[EUR]
BHA Make Up	[h]	2.00	70.00	140.00	[EUR]
Mud Preparation	[h]	2.00	70.00	140.00	[EUR]
Mud Chemicals	[job]	1.00	3,100.00	3,100.00	[EUR]
Lab. Test	[h]	32.00	70.00	2,240.00	[EUR]
RCD Rig Up	[h]	2.00	70.00	140.00	[EUR]
MPD Rental	[day]	3.00	9,000.00	27,000.00	[EUR]
MPD Staff	[day]	3.00	2,000.00	6,000.00	[EUR]
Rig Auxiliary	[kW]	7,900.00	0.32	2,550.00	[EUR]
Mud Pump	[kW]	14,544.00	0.32	4,650.00	[EUR]
Industrial Heater	[kW]	48,000.00	0.32	15,360.00	[EUR]
Fuel Consumption	[l]	120.00	1.00	120.00	[EUR]
Water	[m³]	142.00	2.00	284.00	[EUR]
Cuttings Disposal	[job]	1.00	220.00	220.00	[EUR]
Mud Disposal	[job]	1.00	750.00	750.00	[EUR]
Maintenance	[job]	3.00	70.00	210.00	[EUR]
TOTALS				**51,377.00**	**[EUR]**

Bibliography

[1] A. Bencic, M. Prohaska, J.T.V. de Sousa, K.K. Millheim: Slimhole Drilling and Coring-A New Approach, SPE 49261, 1999.

[2] J.T.V. de Sousa, M.Prohaska, A. Bencic: Optimization of Slimhole Dual-Body Bits by Experiments and Computational Fluid Dynamics, SPE 54595, 1999.

[3] T. Byrom: Casing and Liners for Drilling and Completion, Gulf Drilling Guides 2nd Edition, Elsevier Books, 2017.

[4] S. Devereux: Practical Well Planning and Drilling Manual, Pennwell Books, 1998.

[5] W. Gruber, R. Sachsenhofer, N. Koflar: The architecture of the Trofaiach pull apart Basin (Eastern Alps): An integrated geophysical and structural study; 2004.

[6] G. Bada, F. Horvath, P. Dövenyi, P. Szafian, G. Windhoffer, S. Cloetingh: Present-day stress field and tectonic inversion in the Pannonian basin; 2007.

[7] Carmichael, R.S. ed. 1982. Handbook of Physical Properties of Rocks, Vol. 2, 1-228. Boca Raton, Florida: CRC Press Inc.

[8] X.Luo, P. Wee, J. Liu: Estimation of Biot's effective stress coefficient from well logs, 2015.

[9] O. Vincke, P. Longuemare, M. Bouteca and J.P. Deflandre: Investigation of the poromechanical behavior of shales in the elastic domain, SPE/ISRM 47589, 1998.

[10] T. Finkbeiner : Borehole and Reservoir Geomechanics, Institute of Reservoir Engineering, Montanuniversity Leoben; 2016.

[11] M. Zoback, C. Barton, M. Brudy, D. Castillo, T. Finkbeiner, B. Grollimund, D. Moss, P. Peska, C. Ward, D. Wiprut: Determination of stress orientation and magnitude in deep wells, International Journal of Rock Mechanics and Mining Sciences, 2003.

[12] T. Engelder, M. Fischer: Influence of poroelastic behavior on the magnitude of minimum horizontal stress, Sh, in overpressured parts of sedimentary basins, Department of geosciences, Pensilvania State University, 1994.

[13] G. Coates, S. Denoo: Mechanical properties program using borehole analysis and Mohr's circle, SPWLA 22nd Annual Logging Symposium, 1981.

[14] A. Moumin: Geothermal Well Design, Minestry of Energy and Natural Resources, United Nations University, 2013.

[15] T. Byrom: Casing and Liners for Drilling and Completion, Gulf Drilling Guides 2nd Edition, Elsevier Books, 2017.

[16] Climate-Data, “Klima und Wetter in Trofaiach“, 2016. [Online]. Available: https://de.climate-data.org/location/22498/. [Accessed 01 06 2017].

[17] R. Olzem, “Grundlagen und Nutzung der Erdwärme“, 2016. [Online]. Available: http://www.rainer-olzem.de/232.html. [Accessed 06 02 2017].

[18] W. Fleckenstein, A Eustes, W. Rodrigez, A. Berger, F. Sanchez: Cemented Casing: The True Stress Picture, AADE-05-NTCE-14, 2005.

[19] G. Kaldal, M. Jonsson, H. Palson, S. Karlsdottir: Structural Analysis of Casing in High Temperature Geothermal Wells in Iceland, Faculty of Industrial Engineering, University of Iceland, 2015.

[20] Z. Shen: Intermediate Casing Collapse Induced by Casing Wear in High-Temperature and High-Pressure Wells, SPE 155973, 2012.

[21] J. Wu, M. Gonzalez, N Hosn: Steam Injection Casing Design, SPE 93833, 2005

[22] D. Stiles, Schlumberger, D. Hollies, EnCana Corp.: Implementation of Advanced Cementing Techniques to Improve Long Term Zonal Isolation in Steam Assisted Gravity Drainage Wells, SPE 78950, 2002.

[23] A. Albawi: Influence of Thermal Cycling on Cement Sheath Integrity, Petroleum Geoscience and Engineering, Norwegian Univerity of Science and Technology, 2013.

[24] N. Gaurina-Medimurec, D. Matanovic, G. Krklec: Cement Slurries for Geothermal Wells Cementing, Faculty of Mining, Geology and Petroleum Engineering Zagreb, 1994.

[25] E. Nelson, L. Eilers, L. Spangle: Evaluation and Development of Cement Systems for Geothermal Wells, SPE 10217, 1981.

[26] C. Kosinowski, C. Teodoriu: Study of Class G Fatigue using Experimental Inestigations, SPE 153008, 2012.

[27] C. Thonhofer: Evaluation of wellbore cement integrity for groundwater protection, Chair of Drilling and Completion Engineering, University of Leoben, 2015.

[28] I. Godor, J. Schiffer: Vertiefung zu Maschinenelemente, Chair of Mechanical Engineering, University of Leoben, 2010.

[29] N. Morita, S. Shiozawa: Stability Analysis of Casings During Plastic Deformation, SPE 170303, 2014.

[30] Pirtek, “Service & Produkte”, 2017. [Online]. Available: http://www.pirtek.at/products-services. [Accessed 20 07 2017].

[31] WEH, “Rückschlagventil TVR2 Edelstahl-Produktfamilie“, 2017. [Online]. Avaliable: http://www.wehaustria.at/media/itoris/attachments/t/v/tvr2-datenblatt-d.pdf. [Accessed 20 07 2017].

[32] M+E Tebbe-Neuenhaus, "Quarzsand und Quarzkies-Trocken", 2017. [Online]. Available: https://www.tebbe-neuenhaus.de/fileadmin/pdf/quarz/datenblatt/3_15_-_5_6_mm.pdf. [Accessed 20 07 2017].

[33] Halliburton, "Heavyweight Cement", 2017. [Online]. Available: http://www.halliburton.com/en-US/ps/cementing/cementing-solutions/heavyweight-cement/default.page?node-id=hd0dy5a2. [Accessed 20 07 2017].

[34] Halliburton, "Casing Equipment", 2017. [Online]. Available: http://www.halliburton.com/public/cem/contents/Books_and_Catalogs/web/Casing-Equipment.pdf. [Accessed 20 07 2017].

[35] Slide Share :"Drilling Engineering-Primary Cementing", [Online]. Available: https://de.slideshare.net/akincraig/petroleum-engineering-drilling-engineering-primary-cementing. [Accessed 20 07 2017].

[36] Forum, "Production & Completion Products", 2017, [online]. Available: http://www.f-e-t.com/images/uploads/data-sheets/Thermoplastic_Centralizer.pdf. [Accessed 20 07 2017].

[37] Dril-Quip, "SC-90 Conventional Surface Wellhead System", 2017. [Online]. Available: http://www.dril-quip.com/resources/catalogs/16.%20SC-90%20Conventional%20Surface%20Wellhead%20System.pdf. [Accessed 20 07 2017].

[38] Cameron, "Cameron Conventional Wellhead Systems", 2017. [Online]. Available: http://www.cedip.edu.mx/graficacion/petroleros/Administraci%C3%83%C2%B3n%20de%20Pemex%20Exploracion/Aguas%20profundas/Herramientas%20de%20exploracion%20y%20explotacion%20en%20aguas%20profundas/HTML_for_CD/PDFs/tc1261.pdf. [Accessed 25 07 2017].

[39] WKO: "WKO Firmen A-Z, Kontakt, Oswin Mayer", 29 07 2017. [Online]. Available: https://firmen.wko.at/Web/DetailsKontakt.aspx?FirmaID=c1ba5a23-f29d-433b-9680-e373fc5f125f. [Accessed 29 07 2017].

[40] Ferroflex: "Services, Lieferprogramm Stahl und Metall" 2017. [Online]. Available: http://www.ferroflex.ch/tl_files/content/Stierlin/PDF%20Allgemein/Tabellenbuch%20Lieferprogramm%20Stahl.pdf. [Accessed 29 07 2017].

[41] Cam-Tech Products, Inc.: "Master Bushing" 2017. [Online]. Available: http://www.cam-tech.com/mstr_bush.htm. [Accessed 29 07 2017].

[42] Keystone Energy Tools: "Slip Lifiting Deice" 2017. [Online]. Available: http://keystoneenergytools.com/products/Safety-Products/Slip-Lifting-Device. [Accessed 29 07 2017].

[43] SlideShare: "MUD LOGGING course" 2017. [Online]. Available: https://www.slideshare.net/MohamedHamdy101/mud-logging-course. [Accessed 29 07 2017].

[44] Tricon Drilling Solutions: "Roller Cone Rock Bits, Bearing Types, Product Specification Sheets" 2017. [Online]. Available: http://www.triconds.com.au/wp-content/uploads/2017/02/229mm-WLS40.pdf. [Accessed 29 07 2017].

[45] Roloff/Matec: Maschinenelemente, 15th Edition, Viehwegs Fachbücher der Technik, 2017.

[46] NOV: "Iron Roughnecks, Iron roughnecks Catalog" 2017. [Online]. Available: https://www.nov.com/Segments/Rig_Systems/Land/Iron_Roughnecks/ST-80C2_Iron_Roughneck.aspx. [Accessed 29 07 2017].

[47] Scribd: " Iron Roughneck ST-80" 2017. [Online]. Available: https://de.scribd.com/document/263150962/Iron-Roughneck-ST-80C. [Accessed 29 07 2017].

[48] Xinxiang Kehao Machinery Equipment: „Product Categories, Sourcing, PDG-5" 2017. [Online]. Available: http://www.kcrane.cn/product/60640013777-803226036/Factory_outlet_high_performance_electric_chain_hoist_6t_with_competitive_price.html?spm=a2700.8304367.prewdfa4cf.58.464772a65ThMHh. . [Accessed 04 08 2017].

[49] H. Pilger: „Klimaatlas Steiermark" 2017. [Online]. Available: http://www.umwelt.steiermark.at/cms/dokumente/10728281_16178332/f2121802/7_WINDVERH%C3%84LTNISSE%20-%20Vers_2.0.pdf. [Accessed 04 08 2017].

[50] Renewable Energy Concepts: "Basiswissen Solarenergie, Windlastrechner" 2017. [Online]. Available: http://www.renewable-energy-concepts.com/german/sonnenenergie/basiswissen-solarenergie/windlasten-rechner.html. [Accessed 04 08 2017].

[51] C. Spura: Technische Mechanik 1, Stereostatik: Ein etwas anderes Lehrbuch, Springer Viehweg, 2016.

[52] Ina-Laufrollen: „Stützrollen". 2017. [Online]. Available: http://www.fag-ina.at/explorer/download/waelzlager/25-Lauf-Stuetz-Kurvenrollen.pdf. [Accessed 04 08 2017].

[53] Techniker-Forum: „Formel für die Vorschubkraft beim Bohren". 2017. [Online]. Available: https://www.techniker-forum.de/thema/formel-fuer-die-vorschubkraft-beim-bohren.5826/. [Accessed 04 08 2017].

[54] M. Ramsauer: Feasibility Study of a Well Scale Laboratory at Erzberg, Austria, Chair of Drilling and Completion Engineering, University of Leoben, 2016.

[55] Wolfgang Frank: „Hydraulikzylinder Berechnung". [Online]. Available: http://www.wolfgang-frank.eu/hydraulik.php. [Accessed 04 08 2017].

[56] Geoengineer: "Cement Additives for Permation Grouting", 2017. [Online]. Available: http://www.geoengineer.org/education/web-based-class-projects/select-topics-in-ground-improvement/permeation-grouting-additives?showall=1&limitstart=. [Accessed 05 08 2017].

[57] Water Supply Wells: "6. Annular Space & Sealing". 2017. [Online]. Available: https://dr6j45jk9xcmk.cloudfront.net/documents/946/f-chapter-6-annular-space.pdf. [Accessed 05 08 2017].

[58] W. McCall: Accelerated concrete curing: The basics, The Aberdeen group, J960680, 1996.

[59] StonCor: "Underwater High-Strength Grout". 2017. [Online]. Available: http://cms.stoncor.ca/media/169882/3907_fivestar_underwater_high_strength_grout_productdatalr.pdf. [Accessed 05 08 2017].

[60] EpiMax: "High Performance Underwater Grout". 2017. [Online]. Available: http://www.epimax.com.au/files/EM/TDS/EpiMax_480_UW.pdf. [Accessed 05 08 2017].

[61] PAREX: "Technical Mortars". 2017. [Online]. Available: http://www.parex.co.uk/GetFile.ashx?file_id=1068. [Accessed 05 08 2017].

[62] T. Waltham: Foundations of Engineering Geology, 3rd Edition, Spon Press, 1994.

[63] Test International. 2017. [Online]. Available: http://www.testinternational.ru/CBR-Test-Machine-Transducer.php. [Accessed 05 08 2017].

[64] Modo: "Water Pump, Horizontal Boiler Water Multistage, Centrifugal Pump, Pump, D6-50x2". 2017. [Online]. Available: http://www.modopump.net/water-pump/multistage-pump/horizontal-boiler-water-multistage-centrifugal.html. [Accessed 05 08 2017].

[65] Magma: "Our Products, Circulation Heater" 2017. [Online]. Available: http://www.magmaheaters.com/industrial-heaters.html. [Accessed 05 08 2017].

[66] DENAIR: "Products, Air Compressor, Oil-free Air Compressor, DG1/40". 2017. [Online]. Available: http://www.denair.net/oil-free_air_compressor/. [Accessed 05 08 2017].

[67] DrillingFormulas.Com: "Estimate gas migration rate in a shut in well".2017. [Online]. Available: http://www.drillingformulas.com/estimate-gas-migration-rate-in-a-shut-in-well/. [Accessed 05 08 2017].

[68] SiteTec: "Systems, Recycling- & Mix Systems, RM1000E". 2017. [Online]. Available: http://www.sitetec.nl/hdd-equipment-archive/mud-equipment-en/recycling-mix-systems/?lang=en. [Accessed 05 08 2017].

[69] HANSA-FLEX: "Produkte, Schlauchtechnik, Katalog in PDF Format". 2017. [Online]. Available: https://at.hansa-flex.com/produkte.html. [Accessed 05 08 2017].

[70] Speck Pumpen, “Baureihe A”. 2017. [Online]. Available: https://www.speck-pumps.com/de/speck/industrietechnik/hochdruckpumpen/baureihe-a/.[Accessed 05 08 2017].

[71] DeepRock Manufacturing, “ OTTO Rod Handler “. 2017. [Online]. Available: http://www.deeprock.com/index_OTTO.html. [Accessed 14 08 2017].

[72] SiteTec, “ HDD Equipment, Recycling-& Mix Unit, RM 1000E”. 2017. [Online]. Available: http://www.sitetec.nl/wp-content/uploads/2015/05/RM1000E.pdf. [Accessed 05 08 2017].

[73] K. Andersen, P. A. Sjowall, E. Maidla, B. King, G. Thonhauser, P. Zöllner: Case History: Automated Drilling Performance Measurement of Crews and Drilling Equipment, SPE/IADC 119746, 2009.

[74] Drillquest, “HT-400 Pump”. 2017. [Online]. Available: http://drillquest.net/pdf/items/datasheet-2402.pdf. [Accessed 14 08 2017].

[75] M. Bataee, M. Kamyab, R. Ashena: Investigation of Various ROP and Optimization of Drilling Parameters for PDC and Roller-cone Bits in Shadegan Oil Field, SPE 130932, 2010.

[76] DrillingFormulas, “Inside BOP valve (Gray Valve)”. 2017. [Online]. Available: http://www.drillingformulas.com/what-are-differences-between-full-opening-safety-valve-tiw-valve-and-inside-bop-valve-gray-valve/. [Accessed 20 08 2017].

[77] IFWC, “Home, Training & Qualifications, Useful Downloads, Surface BOP Stack Operations BL 10.2-Vertical Well Kill Sheet”. 2017 . [Online]. Available: http://www.iwcf.org/images/pdfs/kill_sheets/surface/Surface_BOP_Stack_Operations_BL_10.2-_Vertical_Well_Kill_Sheet.pdf. [Accessed 20 08 2017].

[78] P. Fredericks, L. Smith, K. Moreau: ECD Managmenent and Pore Pressure Determination with MPD Improves Efficiency in GOM Well, SPE/IADC 140289, 2011.

[79] Weatherford, “Products & Services, Rotating Control Devices, SafeShield Model 1000 RCD”. 2017. [Online]. Available: http://www.weatherford.com/doc/wft126027. [Accessed 20 08 2017].

[80] Chem-Eng-Musings: “A New Equation for the Vapor Pressure of Condensate (saturated liquid Water) a Full Range, Accurate Formula”. 2017. [Online]. Available: https://mychemengmusings.wordpress.com/2016/06/26/a-new-equation-for-the-vapor-pressure-of-condensate-saturated-liquid-water-a-full-range-accurate-formula/. [Accessed 20 08 2017].

[81] Sandvic: “Product & Services, Boiler Tubes”. 2017. [Online]. Available: http://smt.sandvik.com/en/products/tube-pipe-fittings-and-flanges/tubular-products/boiler-tubes/. [Accessed 27 08 2017].

[82] DEA, “Technology, Drilling, High Pressure and –temperature wells (HPHT wells”. [Online] Available: https://www.dea-group.com/en/technology/drilling/high-pressure-and-temperature-wells. [Accessed 27 08 2017].

[83] J. Brett, T. Warren, S. Behr: Bit Whirl-A New Theory of PDC Bit Failure, SPE 19571, 1990.

[84] Schlumberger: "Real-Time Overpressure Detection". 2017. [Online] Available: http://www.slb.com/~/media/Files/resources/oilfield_review/ors89/oct89/2_overpressure.pdf. [Accessed 27 08 2017].

Acronyms

API	American Petroleum Institute
BHA	Bottom Hole Assembly
BOD	Basis of Design
BOP	Blow Out Preventer
BWOC	By Weight of Cement
CAD	Computer Aided Design
CT	Computer Tomography
DC	Drill Collar
ECD	Equivalent Circulating Density
EMW	Equivalent Mud Weight
FE	Finite Element
HPHT	Heavy Weight Drill Pipe
HSE	Health Safety and Environment
IDEL	Instantaneous Drilling Evaluation Log
LOT	Leak Off Test
LWD	Logging While Drilling
MPD	Managed Pressure Drilling
MWD	Measurement While Drilling
OBD	Over Balanced Drilling
OH	Open Hole
PDC	Polycrystalline Diamond Compact
PERT	Pressure Evaluation in Real Time
PLC	Programmable Logic Controller
POOH	Pull Out Of Hole
PPG	Pounds Per Gallon
RCD	Rotating Control Device
RIH	Run In Hole
ROP	Rate Of Penetration
SBR	Styrene Butadiene Rubber
SICP	Shut In Casing Pressure

SIDPP	Shut In Drill Pipe Pressure
SG	Specific Gravity
TVD	True Vertical Depth
VAE	Vinyl Acetate Ethylene
WOB	Weight On Bit

List of Figures

List of Tables